Deciphering Resonances in ^{12}C - a β-decay study of ^{12}B

Andreas M. G. Gad
201303721
Aarhus University
Department of Physics and Astronomy

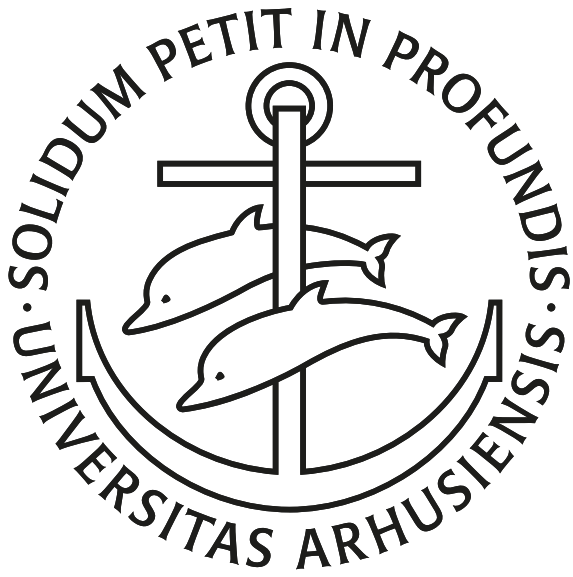

PhD Dissertation

Date: 31$^{\text{st}}$ of Oct, 2021
Supervisor: Hans O. U. Fynbo

This thesis has been submitted to the Faculty of Natural Sciences at Aarhus University in order to fulfill the requirements of obtaining a PhD degree in physics. The work has been carried out under the supervision of Hans O. U. Fynbo at the Department of Physics and Astronomy (IFA).

Department of Physics and Astronomy
Aarhus University
Ny Munkegade 120
DK-8000 Aarhus C
Denmark
Email: ag@phys.au.dk

1st edition, 31st of Oct, 2021

Cover image: Aarhus University's logo.

Resumé

In denne afhandling præsenterer jeg resultaterne fra eksperiment I257, som undersøger henfaldet af den radioaktive ^{12}B kerne. ^{12}B henfalder via β^--henfald til ^{12}C med en halveringstid på 20.2 ms. Mere end 99% af alle henfald populerer enten grundtilstanden eller den bundne første eksiterede tilstand i ^{12}C. De resterende henfald går til højt eksiterede tilstande, der ligger over 3α-tærsklen, og som har en høj sandsynlighed for at bryde op i tre lav energetiske α-partikler. Disse højt eksiterede tilstande består bl.a. af den famøse Hoyle tilstand, samt et bredt område hvor egenskaberne endnu ikke er fuldt forstået. At forstå dette område er det primære mål for dette arbejde.

Eksperimentet I257 blev gennemført i september 2020 ved IGISOL faciliteten i Jyväskylä, ved at implantere radioaktive ^{12}B ioner i et tyndt folie. Energien og impulsen af de udsendte α-partikler blev målt ved hjælp af et specialdesignet detektionskammer bestående af seks dobbeltsidede segmenterede siliciumdetektorer, bakket op af fem enkeltsidede siliciumdetektorer. Den store rumvinkels dækning i denne opsætning resulterer i en høj effektivitet for detektion af koincidenser, hvilket giver os mulighed for at studere opbruddet med fuld kinematisk information.

Et simuleringsværktøj baseret på Geant4 er blevet udviklet for at sammenligne teoretiske modeller med de eksperimentelle data. Dataene er analyseret ved hjælp af en sekventiel henfaldsmodel kombineret med R-matrix teori i to separate grænser. Disse analyser tyder begge på, at størstedelen af den brede peak kan tillægges Hoyle tilstandens *spøgelse* samt en bred 0^+_3 resonans. Beviser for en svagt populeret 2^+_2 resonans i samme område ses også. En sammenligning af faserumfordelingen indikerer, at henfald der fortsætter via ^{8}Be grundtilstanden, dominerer spektret.

Et nyt generaliseret R-matrix udtryk præsenteres og bruges til at lave et kombineret fit til alle dele af dataene. Denne analyse er stadig prematur, men indikerer en tidlig bekræftelse af resultaterne fra de foregående analyser. Derudover viser den at 0_3^+ og 2_2^+ resonanserne henfalder primært gennem ^{8}Be grundtilstanden. Et 0^+ bidrag ved højere energi viser sig at have en signifikant kobling til $^8\mathrm{Be}(2^+)$. Energierne og bredderne af 0_3^+ og 2_2^+ resonanserne fundet i dette studie er fuldt ud i overensstemmelse med resultaterne fra [Hyl+10].

Til sidst er vinkelkorrelationen mellem β- og α-partiklerne analyseret. Denne analyse bekræfter delvist den usædvanligt store anisotropi målt i ^{12}N β henfald i [Gar17].

Abstract

In this thesis, I present the results from experiment I257 investigating the decay of the radioactive ^{12}B nucleus. ^{12}B decays via β^- decay to ^{12}C with a half-life of 20.2 ms. More than 99% of all decays populate the ground state or the bound first excited state in ^{12}C. The remaining decays proceed through excited states, above the 3α-particle threshold, with a large probability of subsequently breaking up into three low energetic α-particles. These highly excited states consist in part of the famous Hoyle state and a broad region of which the properties are still not fully understood. Resolving this region is the primary objective of this work.

The experiment I257 was conducted in September 2020 at the IGISOL facility in Jyväskylä, by implanting radioactive ^{12}B ions in a thin foil. The energies and momenta of the emitted α-particles were measured using a custom-designed detection chamber consisting of six double-sided segmented silicon detectors, backed by five single-sided silicon detectors. The large solid angle coverage in this setup allows for a high coincidence detection efficiency, enabling us to study the breakup with full kinematic information.

A simulation tool based on Geant4 has been developed in order to compare theoretical models to the experimental data. The data is analyzed using a sequential decay model combined with R-matrix theory in two separate limits. These analyses both suggest that the majority of the broad peak can be attributed to the *ghost* of the Hoyle state and a broad 0_3^+ resonance. Evidence for a weakly populated 2_2^+ resonance in the same region is also seen. A comparison of the phase space distribution indicates that decays proceeding via the ^{8}Be ground state dominate the spectrum.

A novel generalized R-matrix expression is presented and used to simultaneously fit all parts of the data. This analysis is still premature but shows early

confirmation of the results from the previous analyses. Additionally, it shows that the 0_3^+ and 2_2^+ resonances decay primarily through the ^{8}Be ground state. A 0^+ contribution at higher energy is shown to have a significant coupling to $^8\mathrm{Be}(2^+)$. The energies and widths of the 0_3^+ and 2_2^+ resonances found in this work are fully consistent with results from [Hyl+10].

Lastly, the angular correlation between the β- and α-particles are analyzed. This analysis partly confirms the unusually large anisotropy measured in ^{12}N β decay in [Gar17].

Acknowledgments

First and foremost, I would like to thank my supervisor Hans O. U. Fynbo and Karsten Riisager, who, for all practical purposes, has also been my supervisor. Their doors have always been open, and I appreciate their help and guidance. I would also like to thank Jonas Refsgaard for his help regarding R-matrix analysis.

Thanks to all the participants and operators at the experiment in Jyväskylä for technical assistance and for welcoming us to Finland. Without their help, there would be no experiment.

Thank you to Michael Munch, Jesper Halkjær, Erik Jensen, and the rest of the subatomic group for a strong collaboration. I have really enjoyed working with you for the past four years.

Lastly, I would like to thank my family for their love and support. In particular, my beloved fiance, Asta, for believing in me and always being supportive.

Andreas Møsvraa Gaarde Gad
Aarhus, October 2021

Contents

CHAPTER 1

Introduction

For the last century, Carbon 12 has been studied extensively by both nuclear- and astrophysicists. The considerable interest in it spans different fields within physics due to its implications in stellar nucleosynthesis as well as fascinating nuclear structure properties. This chapter aims to present a historical overview of some of the essential theories and experimental results related to ^{12}C, as well as a motivation for this study.

1.1 A Brief History of ^{12}C

1.1.1 Stellar Helium Burning

Understanding what we are made of and where we come from has always been a focus of both philosophers and physicists. In 1948, Alpher and Gamow presented one of the first explanations for the origin of matter, the nucleosynthesis model [ABG48], in which all elements were suggested to be created in the Big Bang. According to their model, at the time after the Big Bang, the universe was a dense pool of nucleons and electrons, where elements were created by neutron capture followed by β decay. Due to the short time allowed for this process, they argued that only nuclei just above the upper fringe of the stable elements could be created in this process. Later, it became known that no stable isotopes of mass

number five and eight exists (fig. 1.1), which would prevent any heavier elements from being created, and the nucleosynthesis model, therefore, had to be rejected.

An alternative theory described in [Bur+57] suggested that elements are created in fusion processes during different stages in stellar evolution. Hydrogen burning fuels the main part of a star's life, where hydrogen is converted into Helium. When the core is depleted of Hydrogen, the pressure decreases, and the core collapses under the gravitational pull, while hydrogen burning continues in the outer shell of the star. When the temperature and density increase, it allows for two helium nuclei, or α-particles, to fuse together into ^{8}Be. This nucleus is highly unstable and will decay back into two α-particles with a half-life of around 10^{-17}s. If the star is massive enough, the temperature and density inside the core increase enough such that the α fusion process happens fast enough to produce ^{12}C by fusing with yet another α-particle. However, this is not enough, since the excited ^{12}C nucleus will decay back into three α-particles, unless it lives long enough to de-excite into a bound state in ^{12}C through the triple-α process, $^{8}\mathrm{Be}(\alpha,\gamma)^{12}\mathrm{C}$ suggested by Salpeter and Öpic in [Sal52; Öpi51].

1.1.2 Discovery of the Hoyle state

Carbon 12 is the fourth most abundant isotope in the universe, after just ^{1}H, ^{4}He and ^{16}O [RR88]. In 1953 Fred Hoyle showed that the triple-α process alone could not explain the observed abundance of ^{12}C [HDa53]. He suggested that the triple-α process occurs resonantly through an excited state in ^{12}C. Based on the abundance and expected stellar temperatures, he predicted an unbound resonance just 0.31 MeV above the triple-α threshold with $\Gamma < 25\,\mathrm{keV}$. Later in the same year, the existence of this state, now known as the Hoyle state, was experimentally confirmed by Dunbar in [Dun+53]. A few years later in 1957, the spin and parity of the Hoyle state was determined to be 0^{+} in a β decay experiment by Cook [Coo+57]. This measurement cemented the fact that the Hoyle state plays an important role in the triple-α process. Precision studies has since then determined the excitation energy of the Hoyle state to be at 7.654 MeV, almost exactly where Hoyle predicted. The prediction and discovery of the Hoyle state is an astonishing example of the fruitful collaboration between nuclear- and astrophysics.

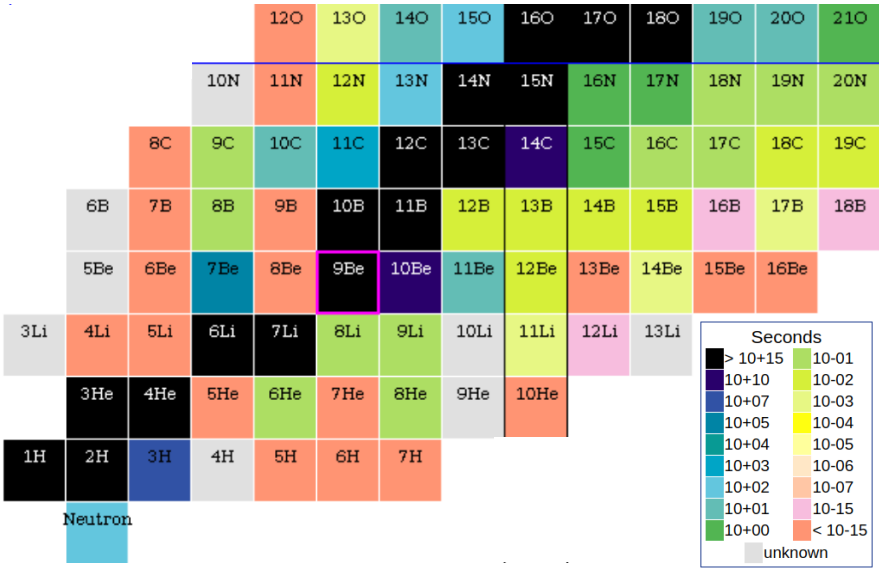

Figure 1.1: *Chart of the lightest nuclides up to Oxygen. The color coding illustrates the half-life. Note that no long-lived isotopes of mass 5 exist [NND].*

1.1.3 Broad resonances

In the years surrounding the discovery of the Hoyle state, other studies found evidence for another structure a few MeV above the Hoyle state [DI53; DJ50]. The first clear evidence was reported by Cook *et al.* in [Coo+58]. They measured the α-particles coming from ^{12}B β decay and saw a broad component with a maximum at 10.1 MeV excitation energy and FWHM = 2.5 MeV. Due to β decay selection rules, they argued that this had to be either a 0^+ or 2^+ resonance, but most likely 0^+ decaying sequentially through the ground state of ^{8}Be with an s-wave α emission.

In 1962 Barker and Treacy [BT62] published an article studying cross sections near particle thresholds, showing that an isolated level near a particle threshold gives rise to an anomalous peak or *ghost* (see section 2.2.3). They found that the observed width of the Hoyle state of $\Gamma = 8$ eV would give rise to a broad peak, roughly in the same region as the previously mentioned 0^+ resonance.

Energy [MeV]	Γ [keV]	J^p	T
g.s.	–	0^+	0
4.43982(21)	$10.8(6) \times 10^{-6}$	2^+	0
7.65407(19)	$9.3(9) \times 10^{-3}$	0^+	0
9.641(5)	46(3)	3^-	0
9.870(60)	850(85)	2^+	0
(9.930(30))	2710(80)	0^+	0
(10.3(3))	3000(700)	(0^+)	0
10.847(4)	273(5)	1^-	0
11.836(4)	230(8)	2^-	–
(12.4)	broad	$(5^+, 4^-, 6^-, 7^+)$	–
12.710(6)	18.1(28)	1^+	0
(13.3(2))	1700(200)	4^+	0
13.316(20)	360(43)	4^-	0
14.079(5)	272(6)	4^+	0
15.110(3)	$45.6(10) \times 10^{-3}$	1^+	1
15.44(40)	1770(200)	(2^+)	0

Table 1.1: *Table of low energy levels in ^{12}C from the most recent evaluation [KPS17]. Energies and spin-parity in parantheses are tentative.*

A combined measurement of the β-delayed α decay of ^{12}N and ^{12}B by Wilkinson *et al.* [Wil+63], increased the accessible energy range in ^{12}C compared to the ^{12}B decay in [Coo+58]. They concluded that the *ghost* contribution from the Hoyle state was unlikely to account for the whole spectra. Instead, they proposed two broad resonances at 10 MeV and 11.8 MeV, respectively. The latter was found to have $\log(ft) \simeq 4.6$, and it was, therefore, concluded it must be populated through allowed decay, fixing the parity as even. For reference, the most recent combined evaluation is [KPS17], and a summary of the lowest energy levels in ^{12}C is shown in table 1.1.

1.1.4 α clusters

Along with the astrophysical implications of the Hoyle state, another motivation for studying ^{12}C was presented in 1956 by Morinaga [Mor56]. In all of the light $4n$-type self-conjugate nuclei, i.e. ^{8}Be, ^{12}C up to ^{24}Mg, there seems to be a

tendency of a 0^+ level not far above the ground state along with a 2_2^+ level not too far above the 0^+ level. In an attempt to give a general explanation for this structure, he suggested that these levels belong to a rotational band. The energy separation of the 0^+ and 2^+ level was used to estimate the deformation of the levels, which he found to be quite high in some cases. For ^{24}Mg, the energy spacing seemed to correspond to a configuration of a linear chain of α-particles. Assuming the same linear chain configuration in ^{12}C, he predicted the existence of a 2_2^+ and a 4^+ level at 9.7 MeV and 14.18 MeV excitation energy, respectively. At the time, the spin and parity of the 9.61 MeV and 14.079 MeV states were not known, and he suggested that it might be the rotational excitation of the Hoyle state. However, he also noted that the narrow width of the 2_2^+ state contradicted the suggested configuration. Later it was found that the spin of the proposed 2_2^+ state was instead 3^-. When the broad resonance at 10 MeV was discovered by Cook and Wilkinson [Coo+58; Wil+63], Morinaga adopted this as the missing 2_2^+ level [Mor66].

In the same period as Morinaga, Ikeda *et al.* proposed the formation of molecule-like configurations of α-clusters near the α-particle threshold in light $4n$ self-conjugate nuclei. This idea is sketched in the Ikeda diagram seen in fig. 1.2. This has since then led to numerous attempts to search for these α cluster states near the particle thresholds.

While the clustered nature of the Hoyle state is well established, the arrangement of the clusters is still unknown. Several structures have been proposed, such as the linear string of three α-particles [Mor66] mentioned previously, Bose-Einstein condensate [Toh+01], and a "bent-arm" configuration [Epe+12]. Determining the energy of the 2_2^+ rotational excitation of the Hoyle state would bring us a lot closer to understanding the structure of the Hoyle state since the energy of such a state is $E = \frac{\hbar^2}{2I} J(J+1)$, where I is the moment of inertia of the state.

1.2 Theoretical Models

Describing the Hoyle state has long been an issue for shell model calculations [CK65; Kar+95; NVB00a; NVB00b], suggesting that it does indeed possess some sort of collective structure. Even more modern *ab initio* calculations such as the no-core shell model have problems [Rot+11] where it appears approximately 5 MeV higher in energy than the experimentally determined value. The failure of

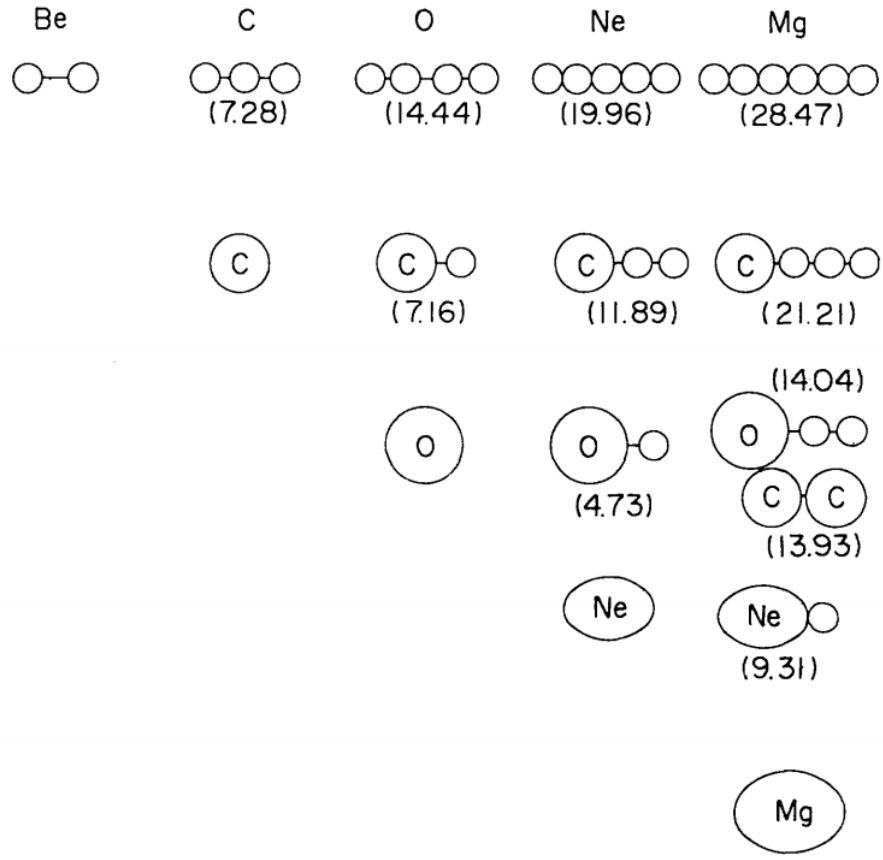

Figure 1.2: *Original Ikeda diagram from [ITH68]. The α threshold energy for $4n$ self-conjugate nuclei up to ^{24}Mg are shown in MeV.*

these models point to the fact that the Hoyle state can not be described with single-particle excitations.

Other models that explicitly include clusterization, such as the Bose-Einstein condensate model [YS04; Fun+05; YS05] have been able to reproduce the even spin levels below 15 MeV and predict a 2_2^+ state at 9.7 MeV. More recently, the Real-time evolution method [ITK19], explicitly assuming α cluster wave functions, has been used to calculate several states in ^{12}C, finding the 2_2^+ state at 9 MeV.

Alternatively, microscopic cluster models such as the Antisymmetrized Molecular Dynamics (AMD) model [Kan07] Fermionic Molecular Dynamics (FMD) model [Rot+04; Che+07] does not explicitly assume clusterization. Instead, it includes nucleon-nucleon interactions, a three-body potential, and in some cases some empirical corrections to reproduce the experimentally observed ground states in different isotopes. The α cluster structure then emerges from these nucleon-nucleon interactions. These models are able to reproduce energies of shell-model states such as the 4.44 MeV level, as well as clustered states such as the Hoyle state. The AMD model also reproduces the electromagnetic and β transition strengths. An analysis of the mass distribution of the Hoyle state found it to be highly clustered, while the 1^+ state at 12.7 MeV showed no cluster structure. The ground state was found to be a mixture of a cluster and a shell-model state. Furthermore, their model gives out a 2_2^+ resonance at 10 MeV with a strong clusterization, which is very similar to the one suggested by Moringa [Mor66]. The study in [Che+07] found similar results as [Kan07], namely that the Hoyle state is a mixture of shell-model and cluster state and the 2_2^+ state shows significant clusterization. However, they find that these two states do not belong to the same rotational band because of different cluster structures.

Lastly, modern *ab initio* models such as Chiral Effective Field Theory (ChEFT) by [Epe+12] have also reproduced both the ^{12}C ground state and Hoyle state. The ground state appeared as a triangular α structure, while the Hoyle state showed a "bent-arm" structure. In their work, the 2_1^+ state and a 2_2^+ state at 10 MeV also came out. These were interpreted as the rotational excitations of the two 0^+ states.

It seems evident that a combined description of ^{12}C must include both clusterization as well as shell-model contributions. Many theoretical models predict the 2_2^+ state to be located around 9.5 MeV to 10 MeV. However, the

interpretation of this state is still very much up for debate. For a thorough review of theoretical descriptions of microscopic clustering in light nuclei, see [Fre+18].

1.3 Recent Studies of Resonances in ^{12}C

One of the main difficulties when searching for the a second 2^+ resonance in ^{12}C, is to get a clear signal without background from neighboring levels. Looking at table 1.1, we see that at least four levels lie close to the region of interest 9.64 MeV (3^-), 10.3 MeV (0^+), 10.84 MeV (1^-), and 11.83 MeV (2^-).

In this section I will review a selection of recent experimental studies specifically developed to find the 2_2^+state and compare their findings.

1.3.1 Scattering experiments

Inelastic scattering is an often-used method of identifying resonance states. In this method a ^{12}C target is bombarded by a beam of some projectile with known energy, and the scattered projectiles are then measured at varying angles. Both p, p' and α, α' scattering experiments have been used to study ^{12}C.

One of such experiments was performed by Freer *et al.* [Fre+09] at iThemba LABS using a 66 MeV proton beam. Another experiment by Itoh *et al.* [Ito+11] used a 386 MeV α-particle beam. In both experiments, a magnetic spectrometer was used to gate on specific scattering angles corresponding to minima in the dominant background contributions.

In 2012, Freer *et al.* published a combined fit to both of these datasets [Fre+12], demonstrating the existence of the 2_2^+ level located at 9.75(15) MeV with $\Gamma = 750(150)$ keV.

A combined R-matrix fit to many different scattering and reactions experiments performed at iThemba LABS was published in [Li+20]. They found that the total fit was significantly improved if the model included not only the 2_2^+ state found by Freer *et al.* and a 0_2^+ level at roughly 11 MeV, but also an additional 0^+ level at roughly 9 MeV.

1.3.2 β decay experiments

One of the more selective experimental probes is β decay. Due to the β decay selection rules, only a handful of states within the β-decay window are populated. The allowed spin and parities of these are 0^+, 1^+, and 2^+. In other experiments, the 3^- state at 9.64 MeV and 1^- state at 10.8 MeV has proved problematic when trying to resolve the even-spin resonance in the region. The exclusion of these is a major advantage of β decay studies.

In the period from 2001 to 2007, a series of experiments measuring the ^{12}N and ^{12}B β-decay was performed at ISOLDE, JYFL [Fyn+03; Fyn+05; Dig+09; Ref16; Gar17] and KVI [Hyl+09; Hyl+10].

In [Fyn+05] ^{12}C was populated through β decay of ^{12}B, and ^{12}N and the total energy spectrum was measured by detecting the energy and position of all three emitted α-particles in the β-delayed triple-α decay (see chapter 3 for more details). The total energy spectrum was then analyzed using R-matrix theory (see section 2.2), and they found that most of the structure at 10 MeV was dominated by 0^+ strength, and the asymmetry of the peak could be explained with strong interference with the Hoyle state. Such a distortion due to interference would not be present if the spectrum was dominated by 2^+ strength. A study of the data from another complete kinematics experiment was presented in [Dig+09], and found that the region around 10 MeV was consistent with a 0^+ resonance sequentially decaying through the ^{8}Be ground state. The energy range from 10.5-11.1 MeV was found to be consistent with a 2^+ contribution, placing the 2^+_2 resonance higher than what was found in scattering experiments.

Later, the β decay was measured by implanting the radioactive isotopes into a silicon detector. This greatly simplified the otherwise complicated acceptance, but with no information about the kinematics of the decay. A combined R-matrix fit to both KVI and JYFL data showed evidence for a 0^+_2 level at 11.2(3) MeV with $\Gamma = 1.5(6)$ MeV and a 2^+ state at 11.1(3) MeV with $\Gamma = 1.4(4)$ MeV.

In 2014 another experiment measuring ^{12}N β decay with full kinematic information and much-improved statistics was performed again at JYFL [Ref16; Gar17]. They were supposed to measure ^{12}B as well, but due to accelerator problems, that part of the experiment was canceled. The experiment presented in this thesis is the missing part. An analysis of the phase space distribution in [Ref16] found similar conclusions as [Dig+09]. In [Gar17], the $\beta - \alpha$ angular

correlation was analyzed and found evidence for the 2_2^+ level at 10.53(17) MeV with $\Gamma = 1.35$ MeV.

1.3.3 Photodisintegration

A study by Zimmerman *et al.* [Zim+13] claimed to have unambiguously identified the 2_2^+ state. They used intense nearly monoenergetic gamma-rays from the HIγS facility to produce α-particles through photodisintegration of ^{12}C. The triple-α breakup was then measured in an optical time projection chamber. The gamma-ray transition cannot populate 0^+ states and only populates the 3^- state weakly, making it an excellent probe to search for the 2_2^+ state. The 2_2^+ state found in this study is located at 10.03(11) MeV with a width of $\Gamma = 800(130)$ keV, which is in quite good agreement with the 2_2^+ level found by Freer *et al.* [Fre+12].

One thing to note, however, is the narrow 3^- level which is located at an energy very close to the 2_2^+ resonance proposed in [Zim+13; Fre+12]. With the lack of natural selectivity compared to β decay studies, one has to be very confident in the handling of this resonance.

1.4 Outline

It should be clear by now that we still to this day do not have a clear understanding of the region around 9 MeV to 13 MeV in ^{12}C. Two camps are starting to emerge, with the reaction experiments finding evidence for a relatively narrow (800 keV) 2_2^+ state just below 10 MeV. On the other hand, the β decay experiments show evidence for a broader (1.5 MeV) 2^+ contribution at around 11 MeV.

In this thesis, I will present the analysis and findings from the experiment I257 performed at IGISOL measuring the β-delayed triple-α decay of ^{12}B. Chapter 2 and chapter 4 consists of a short general overview of the theory and software used in the work. In chapter 3 I present the methods used to probe and analyze ^{12}C. Chapter 5, chapter 6 and chapter 7 presents the experimental apparatus as well as the initial steps of the analysis, such as calibrations and event reconstruction. Simulations are a large part of understanding the data and these are treated in chapter 8. Lastly, the different results are presented in chapter 9.

This chapter consists of a general look at the data, three different R-matrix analysis as well as an analysis of the β-α angular correlation. The findings are then summarized in chapter 10.

CHAPTER 2

Theory

2.1 β Decay

The β-decay process is a weak interaction process in which a proton is converted into a neutron or vice versa. There are three types of processes that fall under the name of β-decay, β^+, β^- and electron capture (EC):

$$\beta^- : \qquad X_Z^A \xrightarrow{\beta^-} Y_{Z+1}^A + e^- + \bar{\mu_e}, \tag{2.1}$$

$$\beta^+ : \qquad X_Z^A \xrightarrow{\beta^+} Y_{Z-1}^A + e^+ + \mu_e, \tag{2.2}$$

$$\text{EC} : \qquad e^- + X_Z^A \xrightarrow{\beta^-} Y_{Z-1}^A + \mu_e. \tag{2.3}$$

The energy available in these decays, the Q-value, is given by:

$$Q_{\beta^-} = M(A,Z)c^2 - M(A,Z+1)c^2, \tag{2.4}$$

$$Q_{\beta^+} = M(A,Z)c^2 - M(A,Z-1)c^2 - 2m_e c^2 \tag{2.5}$$

$$Q_{EC} = M(A,Z)c^2 - M(A,Z-1)c^2, \tag{2.6}$$

where $M(A,Z)$ is the atomic mass of an atom with Z protons and A nucleons. The Q-value is distributed between the final products as either excitation energy or kinetic energy.

2.1.1 *ft*-values and strength functions

The spectral shape of the β-particle energy in allowed β-decays can be described by the Fermi theory of β-decay. The transition probability of the β-decay is given by Fermi's golden rule as:

$$\lambda = \frac{2\pi}{\hbar}|V_{fi}|^2\rho(E_f), \tag{2.7}$$

where $V_{fi} = g\int \psi_f^* \mathcal{O}_x \psi_i d\tau$, and $\rho(E_f)$ is the density of states at the final energy E_f. The density of states can be calculated using statistical mechanics to evaluate the number of ways the available energy can be divided between the β and the neutrino. Assuming the β and neutrino to be free particles, the matrix element can be written in terms of a nuclear matrix element M_{fi} which is the overlap between the initial and final nucleus state wave functions. Combining this, the decay rate for a given β momentum, p_e, can be written as:

$$\lambda(p_e) = \frac{g^2|M_{fi}|^2}{2\pi^3\hbar^7c^3}p^2(Q-T_e)^2, \tag{2.8}$$

where T_e is the kinetic energy of the β particle.

The assumption of the β being a free particle is obviously not true due to its interaction with the Coulomb field from the nucleus. This effect may be corrected by a factor $F(Z_D, p_e)$ called the Fermi function. The total decay rate then becomes

$$\lambda = \frac{g^2|M_{fi}|^2 m_e^5 c^4}{2\pi^3\hbar^7c^3} f(Z_D, Q), \tag{2.9}$$

where

$$f(Z_D, Q) = \frac{1}{m_e^5c^7}\int_0^{p_{max}} p_e^2 F(Z_D, p_e)(Q-T_e)^2 dp_e \tag{2.10}$$

is the Fermi integral, which will also be mentioned as the β-decay phase space. Finally, by rearranging eq. (2.9) the *comparative half-life*, also called *ft-value*, can be obtained

$$ft_{1/2} = \ln(2)\frac{2\pi^3\hbar^7}{g^2m_e^5c^4|M_{fi}|^2}. \tag{2.11}$$

The ft-value ranges from 10^3 to around 10^{20}, with the lower values corresponding to allowed decays.

2.1.2 Selection Rules

The β-decay selection rules impose some narrow constraints on the spin and parity of the daughter nucleus final state. If the lepton pair carry no orbital angular momentum the β decay is classified as *allowed*. The selection rules for *allowed* decays are

$$\Delta J = |J_f - J_i| = 0 \text{ or } 1, \tag{2.12}$$

$$\pi_f \pi_i = +1, \tag{2.13}$$

where J_x is the total spin of the nucleus, π_x is the parity and i and f are the parent and daughter nucleus, respectively. *Allowed* β-decays can be further divided into two categories depending on the total spin of the leptop pair, which can be either 0 or 1. If the lepton spin is 0 it is called a *Fermi decay* and if the spin is 1 it is called *Gamow-Teller decay*.

2.1.3 $\beta - \alpha$ angular correlations

The $\beta - \alpha$ angular correlation function for a 0^+ state should always be isotropic, unlike non-zero spin states which are in general anisotropic. A general expression for directional correlations in β-decays was derived by Morita M. in [MM66]. Assuming the decay scheme

$$J \xrightarrow{\beta,L} J_1 \xrightarrow{\alpha,L'} J_2, \tag{2.14}$$

the $\beta - \alpha$ correlation function, $W(\theta)$, is given in [MM66] as

$$\begin{aligned} W(\theta_{\beta\alpha}) = \sum_{n=0}^{2J_1,even} & \left[\sum_{L \le L'} (-1)^{J_1 - J + n} b_{LL'}^{(n)} W(J_1 J_1 L L'; nJ)(2J_1+1)^{\frac{1}{2}} \right] \\ & \times \left[\sum_{L_1, L_1'} \tau_1^n (J_2|L_1|J_1)(J_2|L_1'|J_1) F_n(L_1 L_1' J_2 J_1) \right] P_n(\cos\theta_{\beta\alpha}), \end{aligned} \tag{2.15}$$

where $\theta_{\beta\alpha}$ is the angle between the two particles, P_n is the n'th order Legendre polynomial, F_n is given as

$$\begin{aligned} F_n(LL'J_1J_2) = & (-1)^{J_2 - J_1 - 1} \\ & \times [(2J_2+1)(2L+1)(2L'+1)]^{\frac{1}{2}} (LL'1-1|n0) W(J_2 J_1 L L'; n J_1). \end{aligned} \tag{2.16}$$

Finally, $b^{(n)}_{LL'}$ is the β parameter found in [MM66] as:

$$b^{(n)}_{LL'} = (J|L|J_1)(j|L'|J_1)^* \times [(2L+1)(2L'+1)]^{\frac{1}{2}} (LL'00|n0). \tag{2.17}$$

In the β-decay, L is the rank of the β matrix element and for the α-decay L' is the total orbital angular momentum of the α particle. $(J_1 J_2 m_1 m_2|Jm)$ and $W(abcd;ef)$ are the Wigner $3j$ and $6j$ symbols, respectively. According to [Mor59] and [RGS65], eq. (2.15) can be rewritten as

$$W(\theta) = 1 + A_2 \cdot P_2(\cos(\theta), \tag{2.18}$$

where A_2 can be separated into a β factor $A_{2\beta}$ and an α factor, $A_2 = A_{2\alpha} \times A_{2\beta}$. $A_{2\alpha}$ can be calculated using eq. (2.16) as described in Sec. 4 of [MM66]. If only allowed matrix elements, M_F and M_{GT}, play a role in the β-decay, then the β factor, $A_{2\beta}$, should be zero. The β factor depends on the relative contributions from higher order forbidden matrix elements, and therefore any anisotropy in the angular correlation at a given excitation energy is proportional to the relative strength of non-zero spin states at that energy. For a more detailed discussion of this, see [Gar17].

2.1.4 ^{8}Li $\beta - \alpha$ angular correlation

A special case that will be used in chapter 9, is the $\beta - \alpha$ angular correlation in ^{8}Li β-decay. ^{8}Li predominantly decays through the first excited 2^+ state in ^{8}Be. Due to the large Q-value and low mass, recoil effects are known to be significant in this decay. The angular correlation is given in [Hol74; TG75; MGG80] as,

$$W(\theta_{\beta\alpha}) = 1 + B\cos(\theta_{\beta\alpha}) + A_2\cos^2(\theta_{\beta\alpha}), \tag{2.19}$$

where the parameter B is related to the β-decay recoil and is approximately given as $B \simeq -\frac{2E}{Mv^*}$, with E being the electron (positron) energy, M is the nuclear mass and v^* is the α-particle velocity in the center of mass. The parameter A_2 is the anisotropy parameter from eq. (2.18).

2.2 R-Matrix Theory

The R-matrix formalism has been used for several decades to interpret experimental data from nuclear reactions and decays in terms of nuclear

resonances. A thorough review of R-matrix formalism is found in the paper by Lane and Thomas [LT58] as well as [Vog62; Vog04]. A detailed derivation of the application to β-decay can be found in [BW88; Hyl10].

The essence of R-matrix theory is the separation of configuration space into an internal part and an external part. The assumption is that all nuclear interactions take place inside the internal region, while the external region is dominated by long-range interactions such as Coulomb interactions and angular momentum barriers. The boundary between the two regions is at the channel radius a_c and can vary from channel to channel. The channel radius is often chosen roughly the same size as the nucleus $a_c = r_0(A_1^{1/3} + A_2^{1/3})$, where $r_0 \simeq 1.4\,\mathrm{nm}$.

The wavefunction in the internal region is expanded in terms of square-integrable eigenstates called levels or resonances. The levels are labeled by λ and the eigenenergy is E_λ, such that $HX_\lambda = E_\lambda X_\lambda$. The total inner wavefunction can be expressed as

$$\Psi = \sum_\lambda C_\lambda X_\lambda. \tag{2.20}$$

The wavefunction is constrained by boundary conditions on their logarithmic derivative, which must match the external wavefunction at the boundary. The coupling strength of a level, λ, to a channel, c, is called the *reduced width amplitude* and is determined by the overlap between X_λ and the pure channel function, ψ_c:

$$\gamma_{\lambda c} = \left(\frac{\hbar^2}{2\mu a_c}\right) \int_S X_\lambda^* \psi_c dS, \tag{2.21}$$

where μ is the reduced mass of the channel and S is the spherical surface at the channel radius.

The square of the reduced width amplitude is proportional to the probability of forming the channel nuclei, separated by the channel radius. However, unlike what one could expect, the probability of observing that channel is not only determined by the reduced width amplitude. In order to be observed, the projectile must tunnel through the Coulomb and angular momentum barrier, which leads to the definition of the *partial width*

$$\Gamma_{\lambda c} = 2P_c(E_\lambda)\gamma_{\lambda c}^2, \tag{2.22}$$

where P_c is called the penetrability and is proportional to the probability of transmission through the barriers. From here, it is possible to calculate reaction cross sections or decay rates.

2.2.1 R-matrix parameters

The R-matrix parameters for each level in the cross-section are the level energy E_λ, and reduced widths, $\gamma_{\lambda c}$. These parameters are related to, but not equal ot the observed parameters from experimental measurements.

To illustrate this in a simple case, we will now take a look at the simplest case with only a single level. Here, the cross-section reduces to the *Breit-Wigner* cross-section

$$\sigma_{cc'} \propto \frac{\Gamma_{\lambda c}\Gamma_{\lambda c'}}{(E - E_\lambda + \Delta_\lambda)^2 + \frac{1}{4}\Gamma_\lambda}. \tag{2.23}$$

In the case of a narrow level, where the energy dependence of the penetrability can be ignored, the observed resonance energy, E_r can be written as

$$E_r = E_\lambda + \Delta_\lambda \simeq E_\lambda - \frac{\sum_c \gamma_{\lambda c}^2 (S_c(E_\lambda) - B_c)}{1 + \sum_c \gamma_{\lambda c}^2 \frac{\delta S}{\delta E}|_{E=E_\lambda}}, \tag{2.24}$$

where S_c is the *shift function* and B_c is the boundary condition imposed on the internal wavefunction. Note, that the shift function and penetrability depend only on the conditions in the external region, and can therefore be calculated analytically. A short description of the functions can be found in Appendix A of [Hyl10], and details of the numerical implementation is found in [Mic07].

The difference between R-matrix and observed parameters also applies to the level widths as

$$(\gamma_{\lambda c}^{obs})^2 = \frac{\gamma_{\lambda c}^2}{1 + \sum_c \gamma_{\lambda c}^2 \frac{\delta S}{\delta E}|_{E=E_\lambda}}, \tag{2.25}$$

$$\Gamma_{\lambda c}^{obs} = 2P_c(E_\lambda)(\gamma_{\lambda c}^{obs})^2. \tag{2.26}$$

Note that the difference between the two is only substantial when considering broad levels where the reduced width is large.

2.2.2 R-matrix formalism applied to β decay

The R-matrix formalism was originally developed to treat particle scattering and reactions. It was then extended to also incorporate β-delayed particle emission in

[Bar68; Bar69] and later in [Hyl10]. This was done in a way analogous to photon channels in [LT58], where the photon phase space factor and width amplitude were substituted by the β decay phase space and beta strength parameters, thereby replacing the cross-section by a decay probability

$$w_c(E) = C^2 f_\beta \sum_c P_c \sum_{x=F,GT} \left| \sum_{\lambda\mu} g_{\lambda\mu} \gamma_{\mu c} A_{\lambda\mu} \right|^2 , \tag{2.27}$$

where f_β is the β decay phase space, $g_{\lambda\mu}$ is the beta strength of λ (analogous to the reduced width amplitude), and C is chosen such that

$$\int w(E) dE = \frac{\ln 2}{t_{1/2}}. \tag{2.28}$$

$A_{\lambda\mu}$ is the *level matrix* defined as

$$(A^{-1})_{\lambda\mu} = (E_\lambda - E)\delta_{\lambda\mu} - \sum_c \left(S_c(E) - B_c + iP_c(E)\right) \gamma_{\lambda c} \gamma_{\mu c}, \tag{2.29}$$

where B_c is the boundary condition imposed on the internal wavefunction.

An interesting feature of eq. (2.27), which will be shown to have a significant impact in the later analysis, is that levels with the same spin and parity can interfere constructively or destructively. Due to interference, it is a bad approximation to describe the full spectrum using a sum of single-level approximations. However, as long as its limitations are kept in mind, the single-level approximation can still be a nice visual guide when interpreting an R-matrix fit.

2.2.3 Ghosts and other threshold effects

The observed shape of a level close to a threshold differs significantly from the usual *Breit-Wigner* shape. At low energy, the penetrability increases faster than the high energy tail of the level decreases and gives rise to a secondary peak at higher energy. These anomalous peaks are often referred to as *ghosts* but are a well-understood consequence of threshold effects.

A similar effect can be seen at high energies in β decays. If a level is located below but close to the Q-value endpoint, the high energy side of the peak is suppressed by both the Breit-Wigner shape as well as the available phase space.

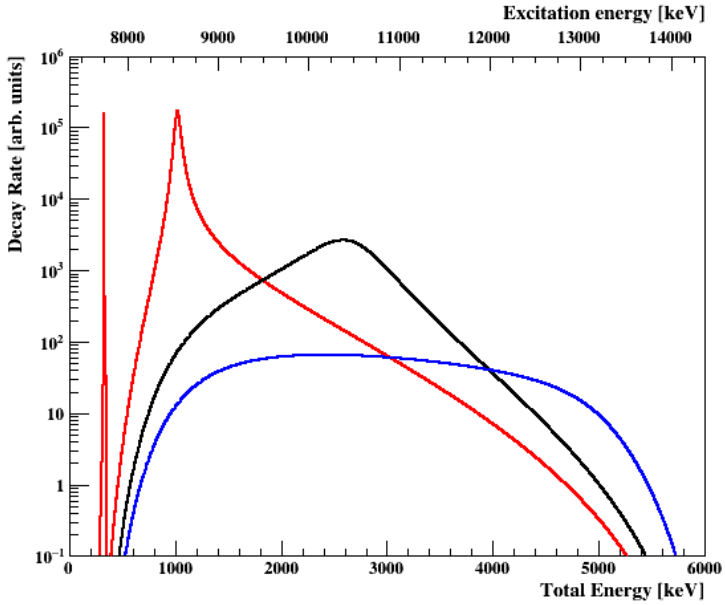

Figure 2.1: *Example of three identical R-matrix levels in* ^{12}B β *decay, differing only by the resonance energy. The red, black and blue lines correspond to* $E_\lambda =$ 7.6 MeV, 10 MeV *and* 12.5 MeV, *respectively.*

The low energy side, however, is extremely enhanced by the increasing phase space, and the Breit-Wigner peak is therefore hidden in a broad shape that does not necessarily resemble a peak. Figure 2.1 show an example of three R-matrix levels in ^{12}C fed by ^{12}B β decay, with identical parameters except for the resonance energy. The level at low energy clearly shows a narrow main peak and a broad ghost contribution at higher energy. The middle level somewhat resembles a regular peak structure, while the high energy level is extremely distorted by changes in phase space, resulting in a broad continuum.

As will be seen later, *ghosts* play a very important role when trying to understand the α decay of ^{12}C. Both the Hoyle state in ^{12}C as well as the ground state in ^{8}Be lie close to the α-particle threshold. In ^{12}C, even though the Hoyle state is only a few eV broad and is located a few MeV below, it is well known that the Hoyle state ghost is responsible for a significant contribution in the broad continuum around 10 MeV excitation energy.

CHAPTER 3

Experimental Probe

This chapter introduces the methods used to study the ^{12}C nucleus, namely through a kinematic study of β-delayed α decay of ^{12}B. In section 3.1 some general properties of the ^{12}B β decay is presented. The concept of Dalitz plots, which will be used extensively throughout the thesis, is introduced in section 3.2. The sequential decay model is introduced in section 3.3, along with two ways of describing the decay using R-matrix formalism. The differences between the two methods are then discussed in section 3.3.3.

3.1 β Decay of ^{12}B

^{12}B is a short-lived radioactive isotope with a half-life of just 20.2 ms [KPS17]. It decays to ^{12}C via β^- decay, producing an electron and anti-electron neutrino. The total available energy in the β decay is

$$Q_{\beta^-} = M(^{12}\mathrm{B}) - M(^{12}\mathrm{C}) = 13.367\,\mathrm{MeV}. \tag{3.1}$$

Due to the β decay phase space, decays to the low energy levels in ^{12}C are heavily favored. Roughly 98% of all decays go directly to the ^{12}C ground state, while 1.28% decays to the bound first excited 2^+ state at 4.44 MeV excitation energy and then subsequently γ decays to the ground state. These decays all

result in a stable ^{12}C nucleus. The remaining 0.69(2)% ([Hyl+09]) decays to highly excited states in ^{12}C above the 3α-particle threshold. The triple-α threshold corresponds to an excitation energy in ^{12}C of

$$E_{3\alpha} = 3M_\alpha - M(^{12}\mathrm{C}) = 7.274\,\mathrm{MeV}. \tag{3.2}$$

When the ^{12}C daughter nucleus ends up in an excited state above $E_{3\alpha}$, it can either decay via γ emission or α emission. The Hoyle state and higher lying states within the β decay window all have a very large probability of decaying by emission of an α-particle.

Due to the β decay selection rules, not all states in ^{12}C are populated through this decay, effectively removing unwanted background from high spin and odd parity states. The relevant levels in ^{12}C are illustrated in fig. 3.1, together with the energetically available states in ^{8}Be.

Only two narrow states populated in allowed β decay and above the triple-α threshold lie within the ^{12}B β-decay window in ^{12}C. The Hoyle state is a 0^+ level at 7.65 MeV, only 380 keV above the triple-α threshold, and the 1^+ level located at 12.7 MeV, just 657 keV below the end-point of the β decay window. In between those two narrow levels is a broad continuum region marked by the grey area in fig. 3.1. Resolving this region is the main interest of this study.

3.2 Dalitz Coordinates

The Dalitz plot is a visual representation of the phase space of a three-body decay involving spin 0 particles. It is named after Richard Dalitz who first applied this representation in 1953 [Dal53]. For a three-body decay, there are 12 degrees of freedom coming from the three Lorentz vectors. There are four constraints from 4-momentum conservation, three masses, and three Euler angles which reduces the total degrees of freedom to two. The original Dalitz plot used the x and y coordinates

$$x = \frac{\sqrt{3}(E_1 - E_2)}{E_{tot}}, \tag{3.3}$$

$$y = \frac{2E_3 - E_1 - E_2}{E_{tot}}, \tag{3.4}$$

where E_i is the kinetic energy of particle i and $E_{tot} = E_1 + E_2 + E_3$.

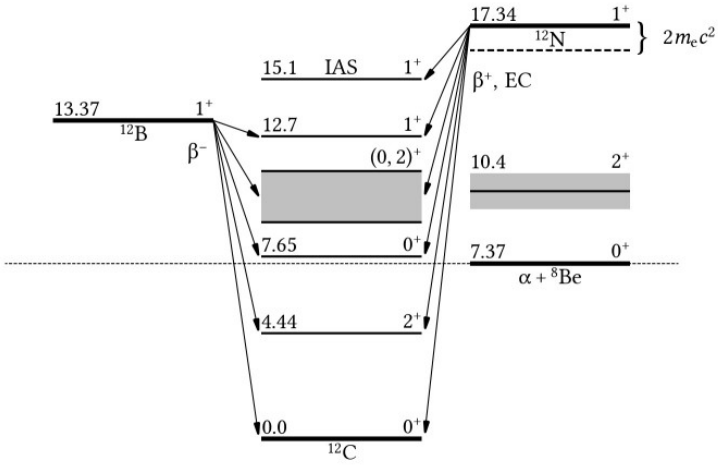

Figure 3.1: *Overview of levels in ^{12}C relevant for the β-delayed triple-α decay of ^{12}B and ^{12}N. All energies are given in MeV above the ^{12}C ground state. Numbers on the right side of levels are spin and parity, J^p. Figure generated from [Jen21].*

The equilateral triangle in fig. 3.2 indicates the area of the Dalitz plot, which is allowed by energy conservation. Furthermore, due to having three identical particles and momentum conservation, the decays are confined to the circle of unit radius shown in the same figure. Having three identical particles creates six possible naming configurations, which introduces a six-fold symmetry. This symmetry is shown by the six *slices* in the plot. If we adopt the convention that $E_1 > E_2 > E_3$, the possible decays all lie within a single slice marked by the green area in fig. 3.2. If the amplitude is constant, then the Dalitz plot will be uniformly populated. In later chapters, this will be referred to as *uniform phase space decay.*

3.3 Sequential Decays

The β-delayed triple-α process can be viewed in a sequential picture with two separate α emissions in succession. The first process breaks ^{12}C up into ^{8}Be and an α, leaving the ^{8}Be fragment in an unbound state, which then immediately decays into two α-particles. The β-delayed triple-α process can therefore be

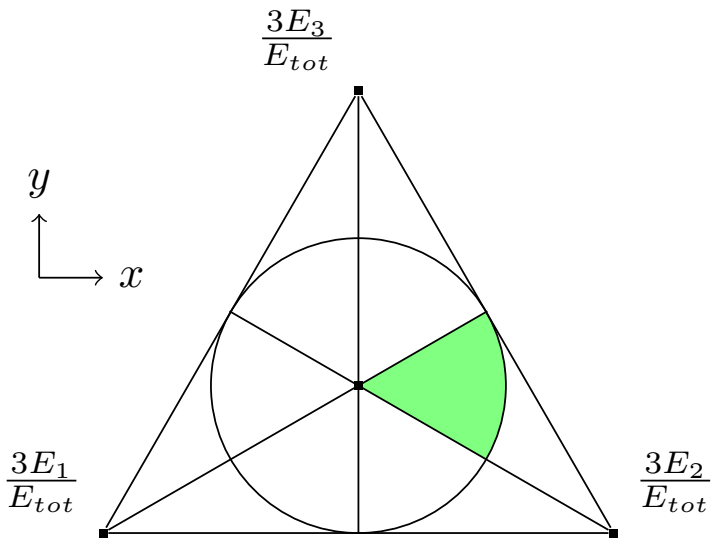

Figure 3.2: *Example of Dalitz plot. The x and y coordinates are defined in eqs.* (3.3) *and* (3.4) *and the kinematics of a three-body decay is completely described by these.*

written as:

$$^{12}\mathrm{B} \xrightarrow{\beta^-} {}^{12}\mathrm{C}^*(j_a) \xrightarrow{l} {}^{8}\mathrm{Be}^*(j_b) + \alpha \longrightarrow \alpha + \alpha + \alpha. \tag{3.5}$$

Due to momentum conservation, the energy of the first emitted α-particle can be expressed in terms of the energy released in the first α emission, Q_1 as

$$E_1 = \frac{2}{3}Q_1. \tag{3.6}$$

The secondary α-particles then share the remaining energy depending on the angle of emission with respect to the first decay as:

$$E_2 = \frac{Q_2}{2} + \frac{Q_1}{6} + \sqrt{\frac{Q_1 Q_2}{3}}\cos\theta_2, \tag{3.7}$$

$$E_3 = \frac{Q_2}{2} + \frac{Q_1}{6} - \sqrt{\frac{Q_1 Q_2}{3}}\cos\theta_2, \tag{3.8}$$

where Q_2 is the energy released in the second step and θ_2 is the angle of emission of α_2 in the ^{8}Be rest frame.

j_a	l	j_b
0	0	0
0	2	2
1	2	2
2	0	2
2	2	0
2	2	2
2	4	2

Table 3.1: *Combinations of spin and orbital angular momentum that conserve spin and parity in ^{12}B β decay.*

In fig. 3.1 we see that only two levels in ^{8}Be is energetically allowed to contribute to the decay. The ground state is a narrow 0^+ level at only 91.8 keV above the double-α threshold. The first excited state is a broad 2^+ resonance roughly 3 MeV above the ground state. Due to the β decay selection rules, only 0^+, 1^+ and 2^+ states are populated in ^{12}C. Conservation of spin and parity narrows down the possible decay channels to the ones listed in table 3.1.

For decays going through the ^{8}Be ground state peak, the energy of the first α-particle is uniquely determined (ignoring β recoil and the small width of the ground state) by the excitation energy in ^{12}C, effectively removing one degree of freedom in the decay. If the energy and momentum of all three α-particles is measured, it is easy to identify these events, which we will label ^{8}Be(peak). In the remainder of this thesis, a distinction will be made between ^{8}Be(peak) and ^{8}Be(ex.), where the latter corresponds to all events not belonging to ^{8}Be(peak). The naming of ^{8}Be(ex.) might suggest that it consists purely of decays going through the ^{8}Be(2^+) excited state, however it is actually a sum of a few components. The ^{8}Be ground state ghost is known to be significantly populated, and it is not possible to distinguish between those two decays on an event-by-event basis. Similarly, a possible direct decay branch would also be indistinguishable from ^{8}Be(2^+) decays.

One of the methods used in this thesis to analyze the experimental spectra is by fitting the spectra to R-matrix models. In the next sections, I will present two R-matrix expressions that can be used to fit different parts of the ^{12}B decay and

discuss the differences between the two models in section 3.3.3.

3.3.1 Three-body R-matrix: I

The R-matrix expression in eq. (2.27) is only strictly valid for two-body reactions. However, it can be modified to include three-body break-ups when approximating this as two sequential two-body reactions. The following explanation is based on [LT58] and [Hyl+10] where the modified R-matrix expression was used to analyze ^{12}B and ^{12}N β decay.

In sec. XIII.2 of [LT58], a sequential three-body reaction is treated by making the reduced widths in the first process, dependent on the energy of the unbound fragment

$$\gamma_{\lambda c}^2 \to \gamma_{\lambda c}^2(E_{23})dE_{23}, \tag{3.9}$$

where E_{23} is the energy above the 2α threshold in ^{8}Be. Whenever the contribution from a channel is included, we must now also integrate over E_{23}

$$\sum_c \to \sum_c \int dE_{23}. \tag{3.10}$$

It is assumed that the energy dependent reduced width, $\gamma_{\lambda c}(E_{23})$ can be factorized as

$$\gamma_{\lambda c}(E_{23}) = \gamma_{\lambda c}\rho_c(E_{23}), \tag{3.11}$$

where $\rho_c(E_{23})$ is the density of states in ^{8}Be.

Due to the different spins of the two states in ^{8}Be, we can use the single-level, single-channel approximation for the $\rho_c(E_{23})$:

$$\rho_{j_b}(E_{23}) = \frac{(2\pi)^{-1}\Gamma_{j_b}(E_{23})}{\left|(E'_{j_b} - \Delta_{j_b} - E_{23})\right|^2 + \left|\frac{\Gamma_{j_b}}{2}\right|^2}, \tag{3.12}$$

where E'_{j_b}, j_b and γ_{j_b} is the energy, spin and reduced width of the state in ^{8}Be.

The normalization is chosen such that the original reduced width is regained when integrating over E_{23}:

$$\int \gamma_{\lambda c}^2(E_{23})dE_{23} = \gamma_{\lambda c}^2. \tag{3.13}$$

This modification to the original R-matrix expression for β decay, can be achieved by introducing the modified penetrability and shift functions

$$\mathcal{P}_c(E) = \int_0^\infty P_c(E - E_{23})\rho(E_{23})dE_{23}, \tag{3.14}$$

$$\mathcal{S}_c(E) = \int_0^\infty S_c(E - E_{23})\rho(E_{23})dE_{23}. \tag{3.15}$$

Now we simply replace P_c and S_c by $\mathcal{P}_c$ and $\mathcal{S}_c$ in eq. (2.27) and in the level matrix in eq. (2.29).

In practice, calculating $\mathcal{P}_c$ and $\mathcal{S}_c$ involves integrating to infinity, however we notice that they do not depend on the level parameters of ^{12}C, which is the fit parameters. We can, therefore, just calculate it once before fitting, making the fit much less computationally demanding.

3.3.2 Three-body R-matrix: II

Another way to describe the sequential picture has been presented in [BZT74], [Fyn+03] and [Dig+09]. The expression for the breakup amplitude is

$$\begin{aligned} f_{1-23} = \sum_{m_b} &\langle l m_a - m_b j_b m_b | j_a m_a \rangle Y_l^{m_a - m_b}(\Theta_1, \Phi_1) Y_{l'}^{m_b}(\Theta_2, \Phi_2) \\ &\times \frac{\sqrt{\Gamma_1 \Gamma_2 / \sqrt{E_1 E_{23}}} e^{i(\omega_l - \phi_l)} e^{i(\omega_{l'} - \phi_{l'})}}{E_0 - \gamma_2^2 \left[S_{l'}(E_{23}) - S_{l'}(E_0) \right] - E_{23} - \frac{i}{2}\Gamma_2}. \end{aligned} \tag{3.16}$$

The notation follows that of [Fyn+03], where (Θ_1, Φ_1) is the direction of emission of the first α-particle in the center of mass, (Θ_2, Φ_2) is the direction of the secondary emissions in the recoil center of mass, j_a and j_b are the spins of the states in ^{12}C and ^{8}Be, l and l' is the orbital angular momentum in the first and second breakup, respectively. E_1 is the kinetic energy of α_1 in ^{12}C restframe, E_{23} is the relative energy of α_2 and α_3 and E_0 is the energy of the intermediate state in ^{8}Be. $\omega_l - \phi_l$ is the Coulomb minus hard sphere phase shift, Γ_1 and Γ_2 are the partial widths of the first and second decay channel and are calculated using eq. (2.22). Note that the three-body correction to the shift function and penetrability from the previous section is also applied in this formula.

The three α-particles are identical bosons, and the final amplitude must therefore be symmetrized in the coordinates of the three particles and averaged over the

initial spin projection m_a, such that the final amplitude is

$$|f|^2 = \sum_{m_a} |f_{1-23} + f_{2-31} + f_{3-12}|^2 . \tag{3.17}$$

Equation (3.17) rests on the assumption that the two α emissions happen completely independently. A detailed study of the triple-α breakup of the 12.7 MeV level in ^{12}C in [Fyn+03] showed that this is in fact not the case. The distance traveled by the first emitted α-particle, α_1, before the breakup of the unbound ^{8}Be fragment can be estimated as $v_{\alpha_1}\tau_{^8\mathrm{Be}} = \sqrt{2\epsilon_1/\mu}$. Assuming a kinetic energy of α_1 to be 1 MeV and using observed partials widths from [Til+04], results in 1.3 nm for ^{8}Be(0^+) and 4.3 fm for ^{8}Be(2^+). In the case of ^{8}Be(2^+), the electrostatic energy of the $^8\mathrm{Be} + \alpha$ system at that distance is on the order of 1 MeV and is therefore clearly not negligible. For decays through the ground state the effect is negligible.

One way of including this correction is presented in [Fyn+03] and eq. 3.10 of [Ref16]. If we imagine that α_1 is formed on the nuclear surface at radius R and then tunnels out to radius R', where the ^{8}Be fragment then breaks up into α_2 and α_3. From here, the penetrability must be replaced with the penetrability for two $\alpha + \alpha$ pairs. This modification can be included my modifying the penetrability as follows:

$$\frac{P_l(\epsilon_1)}{\sqrt{\epsilon_1}} \rightarrow \frac{P_l(\epsilon_1)}{\sqrt{\epsilon_1}} \frac{\tilde{P}_{12,\tilde{l}}(E_{12})}{\sqrt{E_{12}}} \frac{\tilde{P}_{13,\tilde{l}}(E_{13})}{\sqrt{E_{13}}} \tag{3.18}$$

where $\tilde{P}$ is the $^8\mathrm{Be} + \alpha$ penetrability evalutated using a channel radius $\tilde{R}$. In [Fyn+03] a *Coulomb radius* of $\tilde{R} = 10$ fm was found to be appropriate.

Dalitz distributions generated with eq. (3.17) for all allowed decay channels are shown in fig. 3.3. The resonance energy and level width for the ^{8}Be ground state are taken from [Til+04], where $E_{0^+} = 0$ keV and $\Gamma_{0^+} = 5.57$ eV. Parameters for the first excited state are found in [BAS06], $E_{2^+} = 3037$ keV and $\Gamma_{2^+} = 1477$ keV.

In channels going through the ^{8}Be ground state, most of the strength is located in the diagonal component. In fig. 3.3 this component goes beyond the z-range of the plot by several orders of magnitude. The amplitude outside of the diagonal corresponds to decays to the ^{8}Be ghost.

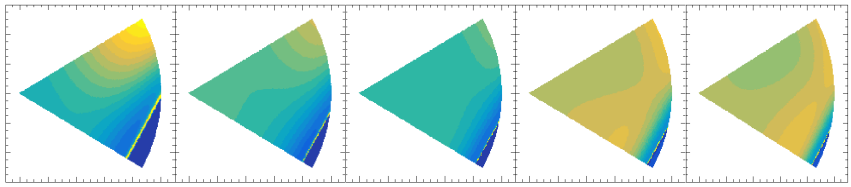

(a) *(0,0,0)*

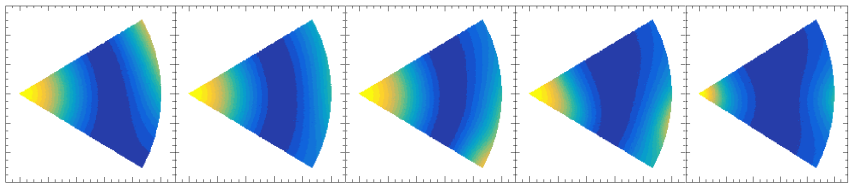

(b) *(0,2,2)*

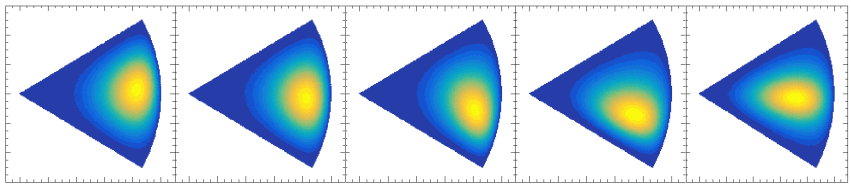

(c) *(1,2,2)*

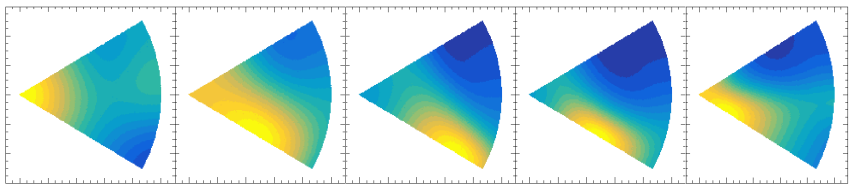

(d) *(2,0,2)*

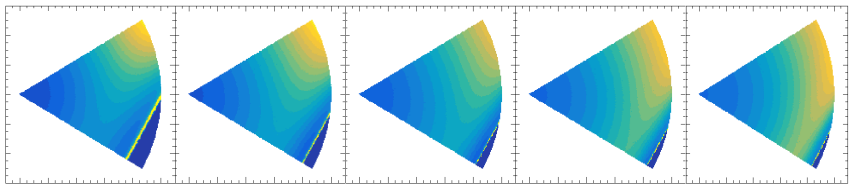

(e) *(2,2,0)*

Figure 3.3

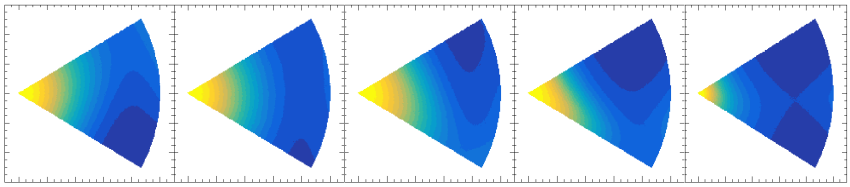

(f) *(2,2,2)*

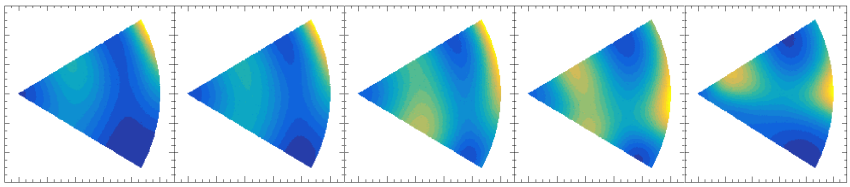

(g) *(2,4,2)*

Figure 3.3: *Dalitz plots calculated with eq.* (3.17) *for all allowed decay channels. Each figure is labeled by* (j_a, l, j_b)*. For each channel, the figures from left to right correspond to* E_{tot} *=1.5 MeV, 2.5 MeV, 3.5 MeV, 4.5 MeV and 5.5 MeV. Note that the diagonal line in all* $j_b = 0$ *channels go beyond the range of the plot.*

3.3.3 Summary

The two R-matrix expressions just presented, have both been used in previous studies to analyze the ^{12}N and ^{12}B β decays using different observables.

The first model predicts the distribution of excitation energy in ^{12}C and correctly includes interference between same-spin levels. However, it does not contain any information about the kinematics of the decay or includes Bose symmetrization. This method was used in [Hyl+10] to fit the shape of the ^{12}C excitation energy spectrum. This effectively corresponds to integrating over the Dalitz plot. If the detection coverage is 4π, which was the case in [Hyl+10], the interference due to the Bose symmetrization is integrated out. The effect of Bose symmetrization on ^{8}Be(peak) decays is negligible, and it is therefore okay to use the model on the ^{8}Be(peak) spectrum. Also, the Coulomb correction from section 3.3.2 only affects the energy distribution of the three particles, but not the excitation energy spectrum and is therefore not needed in this model.

Conversely, the second model does include Bose symmetrization and predicts the Dalitz distribution of a decay channel. However, it does not include interference between states or predicts the distribution of excitation energy in ^{12}C. The Dalitz distributions of ^{12}N β decays were fitted using the expression in eq. (3.17) in both [Fyn+03] and [Ref16]. However, this was done separately in bins of E_{tot} with no absolute normalization, since eq. (3.17) does not contain any information about the total normalization.

Three R-matrix analyses are presented in chapter 9. In section 9.4 the ^{8}Be(peak) are fitted to the model from section 3.3.1, and the phase space distribution is fitted to eq. (3.17) in section 9.3. In section 9.5, a novel combined theoretical R-matrix description will be introduced, and used to make a combined fit to both ^{8}Be(peak) and ^{8}Be(ex.) spectra.

CHAPTER 4

Software

An integral part of most modern experimental efforts is the software we use to analyze the data. This allows us to use a common analysis framework for all of our experiments. This framework is called AUSAlib, and is described in section 4.1. Analysing data from a complicated experimental setup with many detectors detecting several particles in coincidence is not a trivial task. Some of the issues can be to estimate detection efficiencies and cross-check results. One of the solutions can be to simulate the experiment using Monte Carlo techniques. In section 4.2 I will present a simulation tool I have developed to be used together with AUSAlib.

4.1 AUSAlib

AUSAlib is a data analysis framework created in our group primarily by M. Munch, O.S. Kirsebom, and J.H. Jensen [MHK17]. It is written in the C++ programming language and is based on ROOT [CER21].

Many of the experiments we do in our group share a similar structure. The core of the setup usually includes a number of Double-sided Silicon Strip Detectors (DSSD's) and Single-sided Silicon Detectors (SSD's). This means that some of the initial steps in the analysis, such as energy calibration and front/back-side matching, are mostly the same in all experiments.

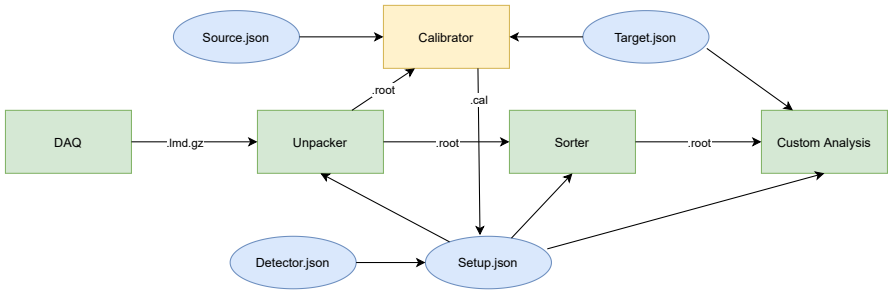

Figure 4.1: *Flowchart showing the AUSAlib analysis pipeline.*

Previously each member of our group had to, more or less, build their own analysis from scratch. However, there are a two primary downsides to this procedure. The first is that most people in areas such as nuclear and particle physics, where the data analysis is very time consuming, only do a few experiments during their academic career. This means that it is very inefficient for each person to start from scratch. The second is that by having each person make their own analysis, you increase the risk of including bugs and errors in an analysis.

The main idea behind AUSAlib is to streamline the parts of an analysis that can be re-used. Some of the main ingredients in AUSAlib is:

- Detectors - AUSAlib has build-in classes for each type of DSSD's and SSD's we use. This class includes the layout, size, thickness, deadlayers, number of segments and whether it is double-sided or not.
- Setup - The backbone of an AUSAlib analysis is the setup-file. This is a *.json*-file which contains a number of detector-entries. Each entry specifies the name, type of detector, position, orientation, calibration file as well as the data mapping from unpacked-files. An example is shown in fig. 4.2.
- Geometry - AUSAlib allows the user to get pixel- and target positions with a single function call. It also includes methods to calculate transversed distance in target layers.
- Calibration - AUSAlib provides a tool for quick energy calibration, where the user specifies the type of calibration source, setup-file and calibration data.

- Energy loss - AUSAlib also includes tools for calculating energy losses based on tabulated stopping powers from either SRIM [ZZB10] or ICRU [05; Ber+16]

A typical analysis pipeline is shown in fig. 4.1. At first the raw data is stored in list-mode-data format. In the unpacking step, this data is transformed into a more usable *.root* format where TDC and ADC signals for both sides of each detector, as well as any other scalers, are saved in *TBranches*.

The next part of the analysis pipeline is done by the *Sorter*. This program has three primary jobs. First is to apply the linear energy calibration specified in the setup-file. Secondly, to make a front- and back matching based on the smallest possible energy difference between the two sides. Finally, the Sorter also applies a TDC calibration provided by the user. Because AUSAlib keeps track of the position of each detector, these hits correspond to *physical* hits, with well-defined time and energy information as well as the position of the hit in a global coordinate system.

The next step in the analysis depends on the specifics of the experiment. This often involves identifying the type of particle and/or finding coincidences. For this job, we have a custom analysis skeleton where loading data, and handling geometry is already done. What is left for the user is to define selection criteria and the type of output e.g *TTree's*, histograms or figures.

4.2 G4Sim

Monte Carlo simulations play a huge part in many nuclear and particle physics experiments. Up until now our group has used a simulation tool called SimX. This program allows the user to specify a reaction or decay in a reaction-file using json format. The program was build in-house, and it is only used by our group. The tool is very useful both as a part of the analysis, but also as a preparation for experiments to optimize detector geometry for high efficiency. However, one disadvantage by using our own software, is that it is not standardized or easy to compare with widely used frameworks such as Geant4. Also, SimX does not include the handling of leptons which can be problematic in β-decay studies. Due to these reasons, I have chosen to develop a new Monte Carlo simulation tool called G4Sim [Gad21], based on Geant4 [Ago+03]. The

```
{
  "name": "i257",
  "detectors": [
    {
      "name": "Det1",
      "file": "Detectors/AUW1_60_2881-1.json",
      "calibration": "ADC_feb/Det1.cal",
      "position": {"x": "50mm", "y": "0mm", "z": "0mm"},
      "normal": {"x": "-1mm", "y": "0mm", "z": "0mm"},
      "orientation": {"x": "0mm", "y": "1mm", "z": "0mm"},
      "frontMapping": {
        "multiplicity": "",
        "prefix": "DET1F",
        "segment": "I",
        "adc": "_E",
        "tdc": "_T"
      },
      "backMapping": {
        "multiplicity": "",
        "prefix": "DET1B",
        "segment": "I",
        "adc": "_E",
        "tdc": "_T"
      }
    },
    {
      "name": "P1",
      "file": "Detectors/AUPAD_1000_3112-16.json",
      "calibration": "PDummy.cal",
      "position": {"x": "55mm","y": "0mm","z": "0mm"},
      "normal": {"x": "-1mm","y": "0mm","z": "0mm"},
      "orientation": {"x": "0mm","y": "1mm","z": "0mm"},
      "mapping": {
        "adc": "P1_E",
        "tdc": "P1_T"
      }
    }
  ],
  "signals": [
      "CLOCK"
  ]
}
```

Figure 4.2: *Example of an AUSAlib setup file.*

primary reasons for choosing Geant4 as the framework, is that is it widely used and accepted within the nuclear and particle physics community, as well as being continuously updated and maintained.

One of the main criteria for G4Sim, is that it should be easy to incorporate into an existing AUSAlib analysis. Fortunately, Geant4 and AUSAlib shares a lot of the same abstractions.
A Geant4 simulation is controlled by the class *G4RunManager*, which keeps control of what to run and when. There are 8 abstract interfaces for user input. Three of these are mandatory, while the remaining five are optional. The mandatory inputs are:

- *G4UserDetectorConstruction* - defines the material and geometric setup.
- *G4UserPhysicsList* - defines the physics processes that are included in the simulation.
- *G4UserPrimaryGeneratorAction* - defines the initial conditions of the primary particles.

The five optional base classes represent a step in the simulation. From large to small, these are:

- *G4UserRunAction* - a run contains a number of events.
- *G4UserEventAction* - an event is defined in G4UserPrimaryGeneratorAction.
- *G4UserStackingAction* - a stack contains a number of tracks.
- *G4UserTrackingAction* - a track defines a particle propagation.
- *G4UserSteppingAction* - a step is one simulated step in a particle propagation.

The five optional base classes are all based on a similar structure and have one method called before and after the event that it represents.

4.2.1 Physics

The physics in Geant4 is loaded through a *G4PhysicsList*, which is a list of reaction packages. The only responsibility of the physics lists in G4Sim, is to

handle energy loss when propagating charged particles through matter. The relevant energy scale is from a few keV to several MeV. There are several prebuilt physics packages in Geant4 which handle this domain, and for G4Sim I have chosen to use *G4EmLivermorePhysics*, which includes tabulated stopping powers from [Ber+16] for many charged particles and nuclei.

4.2.2 Geometry

As we already have a setup-file which keeps tab on the geometric setup in AUSAlib it is natural to re-use this. This file is therefore fed to the implementation of G4UserDetectorConstruction, and this class then loops over a list of DSSD's and SSD's and determines the type and shape of the detector. Each type is implemented by a corresponding class with some abstractions such as size, thickness and number of strips.

4.2.3 Sensitive Detectors

In Geant4 a particle can be measured in a *G4VSensitiveDetector*. In G4Sim the detectors are build by a number of sensitive volumes, one for each pixel in the detector. A sensitive volume has a method that is called everytime a particle takes a step inside the volume. For every event, each sensitive volume creates a *pixel hit*, which saves the volume id and adds up all energy deposited during the event. The list of pixel hits is then passed onto the analyzer responsible for formatting the output.

4.2.4 Output

The output from G4Sim must be compatible with the AUSAlib analysis pipeline. Since the simulation does not include any form of analysis or matching criteria, I have chosen the output to mimic *unpacked* files. First, the list of pixel hits is divided into a list of *strip hits*, where all pixels within a single strip are added together. This would correspond to complete *pile-up* in a detector - something we know is not true. In principle one should determine a time-dependent pile-up, but since these types of event does not survive the matching criteria in the Sorter, it does not matter. To include electronic noise the strip signal is then folded with a gaussian signal with σ_{elec} taken from the AUSAlib detector-file.

Lastly, the calibration-file is used to make an inverse energy-calibration to express the energy in ADC-channels.

4.2.5 Primary Generators

The previous sections described general features that are the same for each experiment. However, we will need to include the actual physics that we want to simulate. This is done by the *G4UserPrimaryGeneratorAction* class, that has a single method called *GeneratePrimaries*. This is where the primary particles are defined, in terms of particle-type, kinetic energy and momentum direction.

G4Sim includes several different types of generators already which can be selected in the macro. These are:

- AlphaSource - Takes a path to the AUSAlib-type alpha source, and generates α particles based on the energies in the source-file.
- GPS - Geant4 included a *GeneralParticleSource* (GPS), which can be controlled via macros [21a]. This option simply generates particles based on this source.
- sim3a - This class generates three α-particles with initial momenta loaded from an externally generated root-file.
- betaDecay - This is a class made solely for the β-delayed triple α-decay of ^{12}B and ^{12}N. It loads an excitation spectrum for ^{12}C, and then sequentially decays three α-particles through either the ^{8}Be ground state or first excited state.

The structure of G4Sim, allows the user to easily create their own primary-generator class, and the program is built with modification-by-addition in mind.

4.2.6 Macros - an example

Lastly, we want to put it all together. G4Sim is controlled through macros, which are simple text-files containing a number of commands. An example of such a macro is shown in fig. 4.3.

```
########   GEOMETRY   #############
# Points to AUSAlib setup-, and target-files.
/G4Sim/setupFile    setup.json
/G4Sim/targetFile   target.json

# Choose name for output file.
/G4Sim/outputFile   outputFile.root

# Determines the AUSAlib alpha-source file
/G4Sim/sourceFile   AUSAlib_source.json

# Chooses which kind of primary generator to use.
/G4Sim/simType alphaSource

# Sets the random engine seed.
/random/setSeeds 1 1000

# Determines the number of events to be simulated
/run/beamOn 500000
```

Figure 4.3: *Example of an G4Sim macro file.*

CHAPTER 5

Experiment I257

The lifetime of ^{12}B being only 20 ms, presents a clear issue when wanting to study its decay, namely that the production of the radioactive nuclei has to be in close physical proximity of the detection system. A technique used to study these types of short-lived isotopes is the *ISOL* method, which was invented over 70 years ago in Copenhagen. Today, several *ISOL* facilities exists around the world. One of those being the *IGISOL* facility for radioactive beam production located at the Accelerator Laboratory of University of Jyväskylä in Finland, which is where we decided to carry out the experiment.

There were several reasons for choosing IGISOL as the location for this experiment, apart from the beautiful location as shown in fig. 5.2. Firstly, we have previously had a good collaboration with the local group, which has led to several articles [Dig+09; Kir+19; Kir+11; Lau+13] and PhD thesis' [Dig06; Ref16; Kir10; Hyl10; Lau14]. Second, we want to make a high statistics experiment to be able to resolve the suppressed region just below the 1^+ state at 12.7 MeV. To do this, we can either have a large yield or long beamtime. In this aspect, IGISOL is ideal since it has historically shown to be a very stable accelerator facility and can produce a high ^{12}B yield of approximately 18×10^3 ions/s. On top of this, we were able to get a long beamtime of 14 days.

The experiment was divided into three parts. The first part was measuring the decay of ^{20}Na, which was used as a calibration source. Secondly, the primary

Figure 5.1: *Timeline of experiment I257.*

objective of the experiment was to measure the β-decay of ^{12}B. Lastly, we measured the β-decay of ^{8}Li. This reason for measuring ^{8}Li is two-fold. For one, we can compare this with a previous measurement of ^{8}B from ISOLDE in 2017 to analyse the mirror asymmetry as a function of excitation energy. This can be used to improve limits on exotic currents. Another reason for this measurement is to act as a validation for the ^{12}B β-α angular correlation measurement since the β-α angular correlation of ^{8}Li β-decay is known to be nearly isotropic. An approximate timeline of the experiment is shown in fig. 5.1.

5.1 IGISOL

The *Ion-Guide Isotope On-Line* (IGISOL) facility first began running in 1993 and has since then been upgraded several times. It is now on its fourth installment and has been running this since 2013 [Den97; Äys+14; Moo+13]. A primary high energy beam of 30 MeV protons is produced by the cyclotron, and is then bombarded onto the production target. When the primary beam hits the production target, many different reactions happen and we are left with a cocktail of different isotopes. Some of these recoil out of the target and are then swept into the ion-guide by a stream of helium buffer gas. The RF sextupole ion-guide is tuned to only allow certain mass ions to pass through the extraction electrode. The ions are then electrostatically accelerated and led through a dipole magnet and finally to the experimental setup. In this experiment we attached the detector chamber to the spectroscopy line shown in fig. 5.3. IGISOL has two primary accelerators. The K-130 cyclotron is the original accelerator and can provide both light and heavy beams. The MCC-30/15 cyclotron is a newer addition installed in 2010. This accelerator can accelerate proton and deuterium beams.

In this experiment, three different production targets were used in combination with both a proton and deuterium beam from the MCC-30/15 cyclotron. For the calibration run, a target of natural Mg was used with a proton beam to produce

Figure 5.2: *Picture of the bridge from Jyväskylä to the Accelerator Laboratory. The picture was taken in August 2020, a few weeks before the beamtime started.*

^{20}Na through a $(p, n\alpha)$ reaction. ^{8}Li was created by a (d, p) reaction on an isotope enriched ^{7}Li target. Lastly, ^{12}B was produced similarly via (d, p) reaction using an isotope enriched ^{11}B target.

5.2 Detectors

In this experiment, we want to measure α- and β-particles. Two types of detectors are included in the setup, W1 Double-sided Silicon Strip Detectors (DSSD's) and Single-sided Silicon Detectors (SSD's) from Micron Technology. The DSSD's are the bread and butter of this experiment, and it is therefore advantageous to into detail on the structure of these. The DSSD's have an active area of 50×50 mm, with 16 contacts on the frontside and 16 perpendicular strips on the backside. This results in 256 pixels, each being 3×3 mm with a 0.1 mm inter-strip separation. This type of contact grid, replaced the older models with a

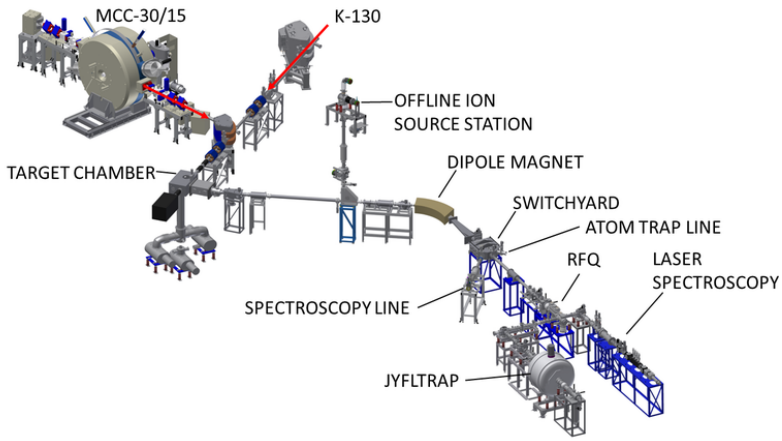

Figure 5.3: *Layout of the IGISOL facility. Picture taken from [IGI].*

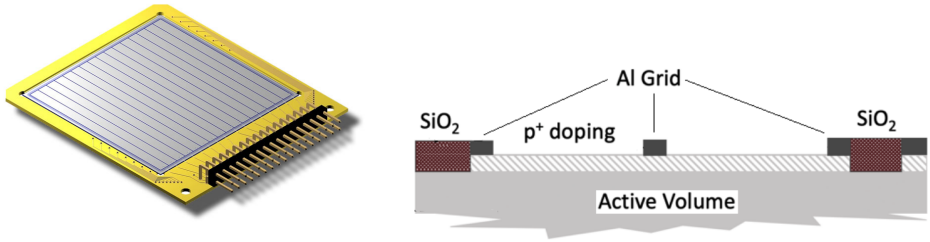

(a) **(b)**

Figure 5.4: *(**a**) Drawing of a W1 type DSSD from Micron Semiconductor Ltd. (**b**) Schematic view of the microscopic structure of a W1 DSSD. Figure is taken from [Viñ+21] and is not for scale.*

continuous Al-grid, and effectively reduces the deadlayer to being only 100 nm on 98% of the surface [Ten+04]. On the remaining 2% we have the aluminum contacts with a thickness of roughly 200 nm. This structure is shown in fig. 5.4b.

5.3 Detection Setup

Most of the experiments done by our group focus on measuring charged particles using silicon semiconductor detectors. Often we want to measure particles in coincidence and therefore want to have a large solid angle coverage. We generally use two types, Double-sided Silicon Strip Detectors (DSSD's) and Single-sided Silicon Detectors (SSD's). Before this experiment, we decided to design a new, easily transportable, detection system to be reused in several experiments at different ISOL facilities. Designing and overseeing the production of this setup has been a part of my work during the first part of this PhD. The result is the setup shown in fig. 5.5a. The outer cylinder is made from aluminum and made to fit inside the *Segmented Germanium Array* (SeGA) from the *National Superconducting Cyclotron Laboratory* (NSCL) at Michigan State University, where the setup is planned to be used for another experiment. Inside, the detectors are placed in a 3D-printed cube shown in fig. 5.5b. It has space for six ΔE-E telescope configurations with a DSSD in the front and SSD in the back. In the middle of the cube, we have a cutout to place a thin collection foil, with custom-designed thin aluminum frames to reduce shadows. One of the advantages of the detector cube and the setup, is that the detector geometry is guaranteed to be the same every time. However, we are still able to change the thickness of each detector depending on the type of decays and particles we want to measure. The solid angle coverage is the six pairs is 54%

In this experiment, we used six DSSD's and 5 pads, since one of them was not working when we came to Finland. The placement and thickness of all detectors are shown in table 5.1 and fig. 5.6.

The punch-through energy of an α-particle on a 60 µm Silicon detector is roughly 9 MeV. In this experiment, the alpha particles are all below 4 MeV, so all alphas will be stopped in the DSSD's. Only a few percent of the β-decays will subsequently α-decay, and we therefore have quite a large β background. A 1 MeV β-particle will deposit on the order of 20 keV in a 60 µm Silicon detector, and on the order of 0.5-1.5 MeV in a 1000 µm detector.

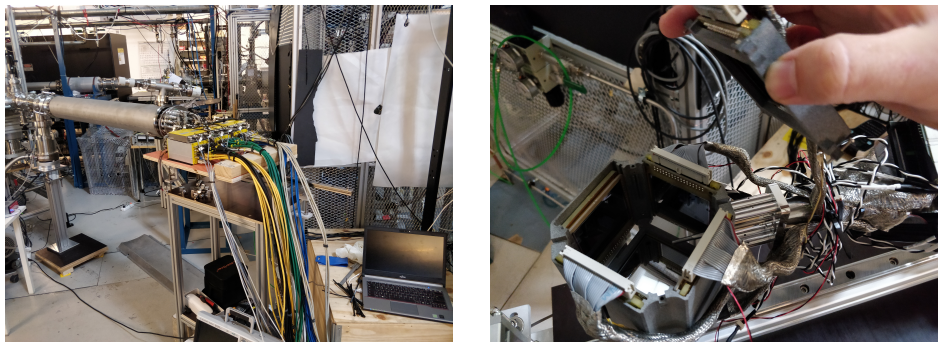

(a) **(b)**

Figure 5.5: *(**a**) Picture of the aluminum chamber and pre-amplifiers. (**b**) Picture of the 3D-printed detector-cube with detectors inserted.*

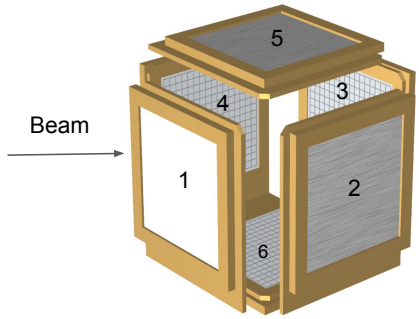

Figure 5.6: *Figure showing the placement of detectors. For each number there is a DSSD (U) and pad (P), except for number 1 which only has a DSSD.*

On the one hand, we would like to be able to measure the position of the β-particles while still being able to measure the position and precise energy of the α-particles. So, four of the DSSD's are thin to minimize the response from β-particle energy deposition and allow precise determination of the α-particle energy. The remaining two DSSD's in pair 2 and 6 were chosen to be thick to be able to measure the β-particle positions.

Pair	DSSD thickness	DSSD deadlayer	Pad thickness	Pad deadlayer
1	67 µm	100 nm	-	-
2	1002 µm	100 nm	1036 µm	500 nm
3	65 µm	100 nm	1497 µm	500 nm
4	60 µm	100 nm	1490 µm	500 nm
5	60 µm	100 nm	1498 µm	500 nm
6	1043 µm	100 nm	1038 µm	500 nm

Table 5.1: *Thickness and deadlayer thickness for all detectors as provided by the manufacturer. However, the precision of this is not stated. Previous experiments has shown that the deadlayer thickness varies within 10-20% of the factory specification [Ref16; Kir10].*

Nuclei	Beam Energy [keV]	Mean Range [nm]	Straggling [nm]
^{8}Li	30	165	40
^{12}B	30	87	21
^{20}Na	30	49	13

Table 5.2: *Ranges and straggling simulated in TRIM for different radioactive nuclei.*

5.4 Implantation Foil

To stop the radioactive nuclei, a thin foil of amorphous carbon was placed inside the detector cube. The foil must be thick enough to stop the radiactive beam, but otherwise as thin as possible to minimize energy loss inside the target. To determine the range of the different beams, simulations were done in TRIM [ZZB10]. The ranges and straggling is shown for the different radioactive beams in table 5.2.

Before the beamtime, we had prepared several foils of three different thickness', ranging from 155 nm to 253 nm. We ended up using a 253 nm catcher foil during the ^{8}Li and ^{12}B runs, due to a couple of reasons. First, we wanted to avoid having to break the vacuum when switching from ^{12}B to ^{8}Li beam, and this was the only foil thick enough to stop ^{8}Li. Secondly, we had problems with the thinner foils blowing out during the beamtime, and this even happened two times

with the thick foil as well. Ventilating and pumping down the chamber was a +5 h process, so it was a priority to avoid having to do this too many times. During the ^{20}Na run, we were using a 155 nm catcher foil.

5.5 Data Aquisition

The data acquisition system is of course, an integral part of any modern nuclear physics experiment. Leading up to the beamtime, I was responsible for setting up the data acquisition system, with the help of M. Munch and E.A.M. Jensen.

A particle passing through a Silicon detector creates a small charge through ionization. For reference, the charge created by a 3 MeV particle in a DSSD is approximately 40 fC. This charge is then amplified and converted into a voltage signal in the pre-amplifier. To reduce noise on the small signal coming into the pre-amplifier, it is positioned as close to the detectors as possible - which in this case was 10 cm outside the vacuum chamber. From here, the signal is fed into a combined amplifier and shaper where the signal, as the name suggests, is further amplified and then shaped into a gaussian signal with FWHM $\sim 2\,\mu$s. From here, the signal is split into three parts. First, the shaped signal is sent to the ADC. Secondly, the amplifier also discriminates the signal using *constant fraction*-discrimination, producing a logic signal which is sent to the TDC with a small delay. Lastly, a logic *OR* from all TDC channels is produced and can be used by the trigger logic.

The trigger signal is fed to the acquisition control system, where the triggers from all amplifiers are compared with 8 pre-defined patterns to determine if a *master-trigger* signal should be produced. If a master-trigger is produced, it is sent to all ADC's and TDC's. While the ADC modules digitize the signal, a *Busy* is sent back to the acquisition control. No master-triggers can be produced while in a busy state, resulting in what is known as *deadtime*. The system was run in *shadow readout mode* [Mun+19] to minimize this deadtime.

5.6 Achievement

Planning and carrying out the experiment I257 was a tumoultuous experience for several reasons. The experiment was first pushed back due to problems with construction of the chamber. After that, it got postponed again due to the

COVID-19 pandemic. Finally, in August 2020, one other PhD student and I were allowed to travel to Jyväskylä to prepare the experiment. One day after arriving back in Århus after setup, lockdowns started being introduced again, and we had to travel back to Finland on short notice. Due to this, most of our collaboration was only able to join us via online meetings. The local group at IGISOL was therefore vital in providing technical assistance as well as being able to help cover shifts for the 14 days of beamtime. Without that help, it is safe to say that the experiment would not have been a success.

The experiment started by measuring the decay of ^{20}Na, to be used as a calibration point. The ^{20}Na included a significant current of stable ^{20}Ne from a buffer gas in an ion trap. This stable beam contaminant charged up the detector cube, which is not electrically conductive, and led to some of the detectors becomming extremely noisy. Due to this issue, the ^{20}Na could not be used in the energy calibration. These issues persisted even after switching to a ^{12}B beam, and as a consequence, the data from the first two days of beamtime had to be excluded from the analysis. The primary beam current was increased significantly during the last part of the experiment, so the two days correspond to only 10% of the total data.

CHAPTER 6

Calibration

This chapter is concerned with "getting to know" our experiment. To extract reliable information from our experiment, we must fully understand the response and effects in the setup. This is also an important step when making accurate simulations, which will be needed in later stages of the analysis.

6.1 Energy

The most important calibration we must do, it to convert the ADC signals into energy. A source containing three α-emitting isotopes was placed inside the detector cube, and rotated such that all detectors were illuminated by the source. This was done three times throughout the experiment. The first calibration was done before getting the first beam, then one while the primary target was changed from Mg to ^{11}B, and lastly, right after the experiment ended. The isotopes in the calibration source is shown in table 6.1, along with the most prominent lines from each isotope.

A linear calibration is done strip-by-strip, and an example of a spectrum from a single strip is shown in fig. 6.1a. When calibrating a single strip, an approximate peak is first found without correcting for energy loss in the source itself or the detector deadlayer. Next, the resulting spectrum is analyzed to find the energy loss in the source. Lastly, a precise calibration is done that accounts for all effects.

Isotope	E_α (KeV)	I_α
^{239}Pu	5156.6	0.709
	5144.3	0.171
	5105.5	0.120
^{241}Am	5485.6	0.866
	5442.8	0.134
^{244}Cm	5804.8	0.769
	5762.6	0.231

Table 6.1: *Most intense lines from the isotopes in the triple-α calibration source. Values are those listed in [ENS].*

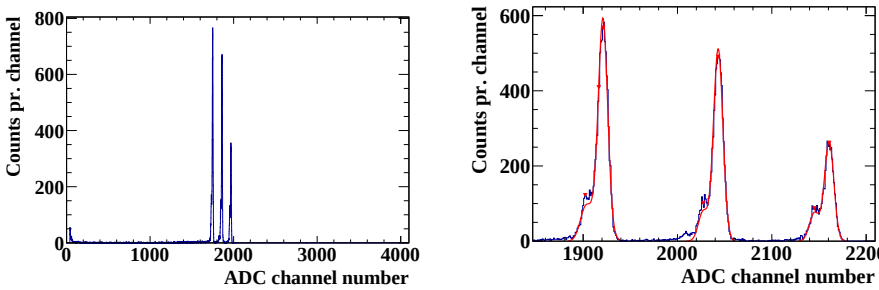

Figure 6.1: *(**a**) Typical 3α spectrum from a single strip. Here it is shown for backstrip 8 in detector U1. (**b**) The blue line is data, and the red line shows gaussians fitted to the ADC spectrum. Peak positions are marked by the small red arrows.*

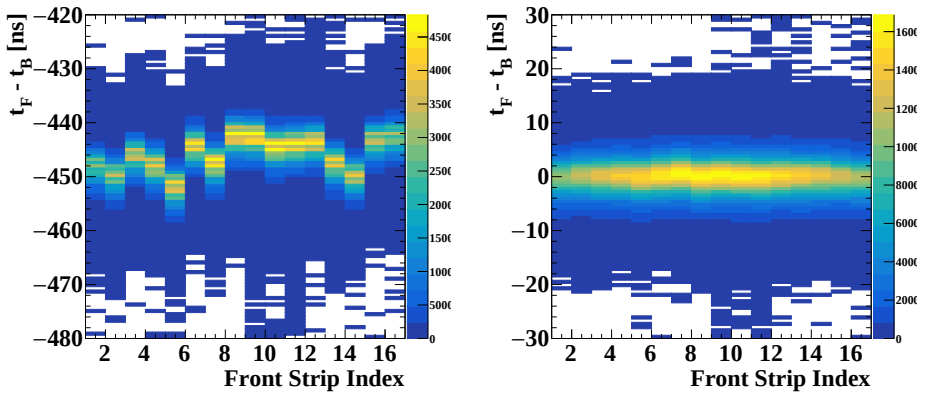

(a) **(b)**

Figure 6.2: *$t_F - t_B$ is the time difference between front- and back-side hits. (**a**) Typical spectrum before TDC calibration. (**b**) Same spectrum after alignment.*

6.2 TDC Calibration

Since we want to measure three alpha particles in coincidence, we also want to make sure that they originate from the same decay, i.e. avoid random coincidences. One way of eliminating random coincidences is to make a gate on the time difference between the hits. However, while all TDC channels have the same time division they are offset by a varying amount, depending on factors such as the lenght of cables in the DAQ. The solution is, therefore, to do an alignment of the TDC channels.

The alignment happens in two steps. First each strip in a single detector is aligned such that the front- and back strip time difference is zero. To do this alignment, real particles hits are used. In this case, alpha particles from ^{12}B are used with an energy above 400 keV. A reference strip is chosen on the front side, and all back side strips are aligned to this. Then a reference strip in the back side is chosen and the remaining front-side strips are aligned to this. The result of the alignment is shown in fig. 6.2.

The second part of the TDC alignment, is to find the offset between different detectors. To do this, we need real coincidence events. The coincidence events

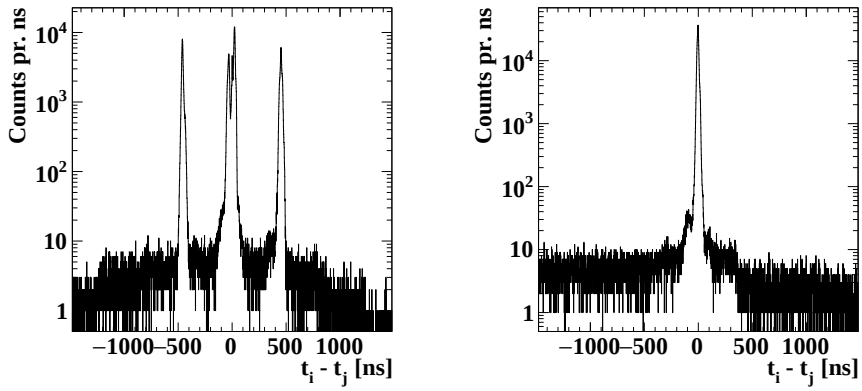

Figure 6.3: *$t_i - t_j$ is the time difference between two hits in multiplicity 3 events. (**a**) Typical spectrum before TDC calibration. (**b**) Same spectrum after alignment.*

were found by first running the coincidence analysis explained chapter 7 without the TDC gate. A reference detector is chosen, and the offset for all other detectors is then found. The result of this alignment is shown in fig. 7.1.

6.3 Implantation Foil Thickness

The same carbon foil was used for ^{12}B and ^{8}Li to avoid having to break the vacuum between runs. This foil was specified by the manufacturer to be $50\,\mu g/cm^3$ which corresponds to 253 nm. However, experience from previous experiments has shown that the thickness can easily vary by up to 30% and even change during the experiment. It is, therefore, necessary to determine the thickness using data.

The lack of narrow peaks in the spectrum from both ^{12}B and ^{8}Li makes determining the thickness difficult, but it is possible to estimate based on the ^{8}Li β-decay. Since the two α-particles are emitted back-to-back with equal energy in the restframe of ^{8}Be, we should measure two α-particles with equal energy except the recoil created by the β-decay. Assuming the decay happens at rest inside the foil at the implantation depth simulated in TRIM, the α-particle detected in one

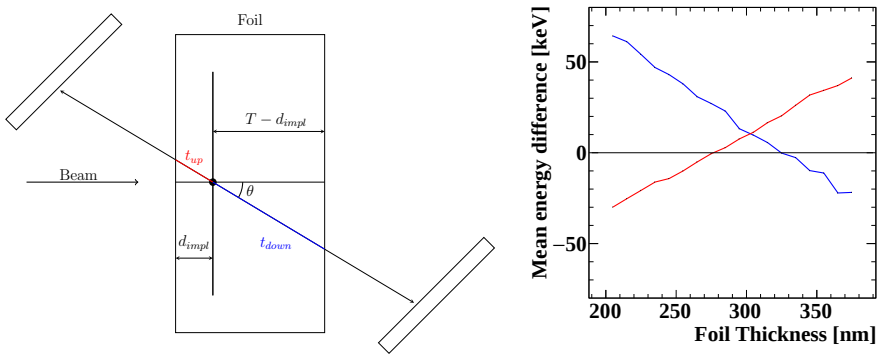

(a) **(b)**

Figure 6.4: ***(a)*** *Illustration of effective foil thickness.* ***(b)*** *Plot of the mean energy difference between two 2α-coincidences from* ^{8}*Li β-decay as a function of foil thickness. The blue line is detectors U1 and U3 and red line is detectors U2 and U4.*

of the upstream detectors will transverse a thickness of

$$t_{up} = \frac{d_{impl}}{\cos\theta}, \tag{6.1}$$

while the downstream α will transverse

$$t_{down} = \frac{T - d_{impl}}{\cos\theta}, \tag{6.2}$$

where T is the foil thickness, d_{impl} is the implantation depth and θ is the angle between the foil normal-vector and the particle direction.

As the two α-particles are emitted back-to-back, we will either detect them in detectors U1 and U3, or U2 and U4. Figure 6.4b shows a plot of the mean energy difference between the upstream- and downstream α-particles from ^{8}Li decay, as a function of the foil thickness for the two detector pairs. It shows that there is an asymmetry in the estimation which is not understood. However, we can estimate the foil thickness as a mean of these two values which is 290 nm and accept uncertainty on the order of 25 nm.

CHAPTER 7

Event Reconstruction

This chapter is concerned with identifying triple-α coincidence events by applying various energy corrections and cuts. This part of the analysis is divided into two parts. The first part is to identify particle hits and determine their initial energy. The second is to match hits in coincidence to form events.

7.1 Particle Hits

7.1.1 Matching

In most circumstances, when a particle hits and deposits energy in a DSSD, the DAQ will read out two signals, one on each side, as shown in fig. 7.1a. In these cases, the matching procedure is trivial. However, in this experiment, we often expect to see one alpha particle in one detector and two in the opposite detector. The two α-particles in the second detector will most times have similar energy. Such an example is shown in fig. 7.1b. A non-*greedy* algorithm is used to minimize the total energy difference of both hits:

$$\min\left(\sum_i |E_{f,i} - E_{b,i}|^2\right), \tag{7.1}$$

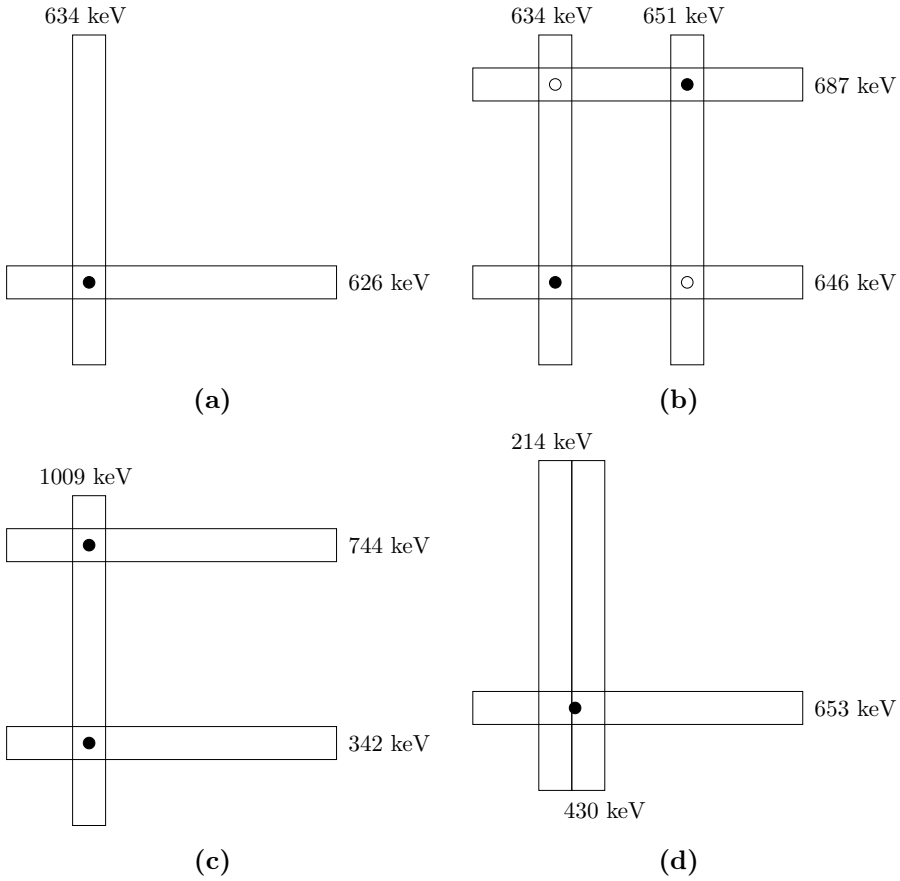

Figure 7.1: *Solid circles indicate the positions of the hits. (**a**) Simple event with one hit in each side. (**b**) Multi-hit event. Solid dots are the result of a non-greedy minimizer, while a greedy minimizer would result in the hollow circles. (**c**) Example of a summing event. (**c**) Example of a sharing event.*

where no pair can have an energy difference larger than a user-specified tolerance. If a regular *greedy* algorithm was used in fig. 7.1b, the matched hits would correspond to the two hollow circles.

A more complex case is where the multiplicity in the front-side is not equal to the back-side. This can happen due to a number of reasons. First, the extra signal in one side can be due to noise. Unless the noise is very close to the particle energy,

it should still be possible to determine the real hit based on the energy difference. This effect is mostly a concern at low energies.

Another example is shown in fig. 7.1c, where the single signal is larger than the two others. This is due to *summing*, where two particles hit the same strip, and their energy is partially summed. If summing happens in the front-strip, the energy is determined as:

$$E_{f,i} = E_f \cdot \frac{E_{b,i}}{\sum_j E_{b,j}}. \tag{7.2}$$

Lastly, we have the example shown in fig. 7.1d, where a particle hits the interstrip region, and the measured charge is divided between two neighboring strips. This phenomenon is called *sharing*, and here the energy of the shared signal is just determined as $E = E_i + E_j$. Based solely on the ADC-signals it is not possible to distinguish between a *sharing* event and a *summing* event where two neighboring strips are hit. Some TDC's are able to record multiple triggers per event in a single channel, but this is assosiated with some uncertainty as there is a minimum recovery time between such to signals. Instead, we simply treat all events with neighboring strips as *shared* and all others as *summed*.

7.1.2 Energy reconstruction

At this point, we know the position of the hit and the energy it deposited in the detector. The job is then to estimate the initial kinetic energy of the particle. This is done by propagating the particle backward from the detector to the decay-point and adding the estimated energy loss along the way. The decay point is not well defined as the implantation distribution is quite broad, but we assume it to be at

$$\vec{x}_0 = \vec{p}_{tar} + T \cdot \hat{z} - d_{impl} \cdot \hat{z}, \tag{7.3}$$

where the z-axis is defined as the beam direction, $\vec{p}_{tar}$ is the target center position, T is the target thickness found in section 6.3 and d_{impl} is the implantation depth from table 5.2.

In this setup, there are two places the particles will lose energy before being detected. One is in the detector deadlayer and the other is inside the implantation foil, as shown in fig. 6.4a.

SRIM [ZZB10] provides tabulated ranges for many ion and material combinations, and by interpolating these tables we have the range as a continous function of kinetic energy. The energy loss can then be calculated by the method of range-inversion. If E_i is the initial energy before entering the deadlayer, E_f is the energy after exiting and Δx is the traversed distance in the deadlayer, then

$$E_i = R^{-1}\left(R(E_f) + \Delta x_d\right), \tag{7.4}$$

where $R(E)$ is the range-function.

The energy lost inside the target is calculated similarly, where E_f is replaced by E_i.

7.2 Triple-α coincidences

The last step in this part of the analysis is to reconstruct triple-α breakups based on events where all three α-particles are detected. This step involves a number of cuts and assumptions.

7.2.1 List of hits

For each matched hit in a DSSD, the energy in the pad behind is saved as well as the position, direction-vector, time and DSSD energy.

7.2.2 Particle ID

Next, a simple algorithm is used to determine whether the hit is from an α- or a β-particle. All hits in the thin DSSD's are assumed to be α-particles. For the two thick DSSD's, the type is determined as follows:

1. If the SSD behind the DSSD does not have an energy signal, the hit is assumed to be an α-particle.
2. If the SSD does have an energy signal and there is only one hit in that DSSD, it is assumed to be a β-particle.
3. If there are more than one hit in the DSSD and an energy signal in the pad, then the hit is labeled as both a β- and α-particle.

All hits with an α-particle label is then corrected for energy-loss in the detector deadlayer and implantation foil.

7.2.3 Triple-α events

If an event contains at least three possible α-particle hits, the total momentum is calculated for all combinations of α-hits. The combination with the lowest momentum is then selected. If any of the three α-hits is a possible β candidate, this label is removed and the remaining β candidates are saved.

At this point events that include α-particle hits in detectors U5 and U6 are removed. For α-particles that hit these detectors, the effective target thickness is very large due to the large outgoing angle. The exact energy-loss correction is therefore extremely sensitive to errors in the geometry. During the analysis it became clear that it was simply not feasible to include these events.

7.2.4 Multiplicity cut

During the experiment, we saw noise spikes in all detectors coming in a regular interval. A similar effect had been observed in the experiment preceding I257 by one of the people from the IGISOL group. It was thought to be electronic noise coming from the electrical grid. In such an event, many hits will be identified in the matching procedure. The number of matched hits with at least three possible α-hits for a single run is shown in fig. 7.2a. The multiplicity of these noisy events is more or less evenly distributed from 5 up to 50 hits per event. Based on fig. 7.2a, a background of approximately 1% of the events with multiplicity ≤ 5. However, these events are mostly low energy and are quite easily separated from the real 3α-events by placing a cut on the total energy in section 7.2.6.

7.2.5 TDC cut

The TDC's provide useful timing information that can be used to remove random coincidences that are not correlated in time. The ADC gate is 2 µs while the main peak shown in fig. 6.3b is well within ± 100 ns. However, not all low-energy hits will generate a TDC signal, so the best we can do is to place a cut on the time difference on hits that have produced a trigger. The cut is chosen to be $\Delta T \leq 100$ ns.

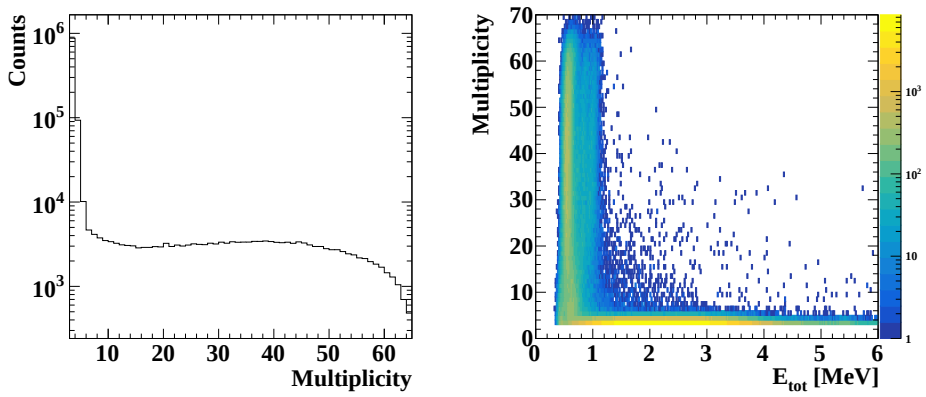

(a) (b)

Figure 7.2: ***(a)*** *Histogram of the matched multiplicity of a single run.* ***(b)*** *Plot of total energy against matched multiplicity.*

7.2.6 Momentum cut

The events surviving so far are shown in fig. 7.3. The real triple-α coincidences lie in the intense elliptical structure at low momentum. The bunch around E_{tot} =5.4 MeV corresponds to decays through the 1^+ resonance at 12.7 MeV excitation energy in ^{12}C. The other structures in this plot are either coincidences with the β-particle or random coincidences and will be investigated in chapter 8.

A two-dimensional energy-momentum cut is made based on the similar analysis in [Ref16], defined by

$$|\sum_i \vec{p_i}| \leq \frac{1}{2}\sqrt{\sum_i E_i + 800 \text{ keV}}, \tag{7.5}$$

and

$$\sum_i E_i \geq 800 \text{ keV}. \tag{7.6}$$

The exact shape of this cut does not have any deeper meaning other than it seems to be a good compromise between including most simulated triple-α decays while excluding most other structures. The effectiveness of the cut is investigated in section 8.5

7.2.7 ^{8}Be decay channel

The relative energy, E_{23}, of α_2 and α_3 provides a way to categorize the triple-α decays. Due to full kinematic information, E_{23} can be calculated using the momentum vectors of the two hits as

$$E_{23} = 2\frac{\vec{p}_{23}^{\,2}}{2m\alpha}, \tag{7.7}$$

where $\vec{p}_{23} = \frac{1}{2}(\vec{p}_2 - \vec{p}_1)$ is the momentum of the center of mass system of the two α-particles. The spectrum of E_{23} is shown in fig. 7.4, and immediately two prominent features are visible. Most events lie in the narrow peak at low energy. This peak has centroid at 95.8 keV with FWHM=41 keV. It then reaches a minimum at approximately 250 keV and then starts rising again, forming a broad continuum up to approximately 2.5 MeV.

Remembering the discussion of ^{8}Be(peak) and ^{8}Be(ex.) decays in chapter 3, all events are now separated into two categories. Events with $E_{23} < 250$ keV are labeled ^{8}Be(peak) and events with $E_{23} \geq 250$ keV are labeled ^{8}Be(ex.).

7.2.8 Summary

The previous sections describe the data reduction procedure in the order of application. To get an idea of the severity of each cut, table 7.1 shows the number of events left after each step.

7.3 Spectra

Figure 7.5 shows the measured energy spectrum in ^{12}C, as well as the energy-dependent distribution between ^{8}Be(peak) and ^{8}Be(ex.). From this, we can make a few interesting observations. The spectrum is consists of a very broad featureless region as well as a narrow peak at 5.4 MeV which is the 1^+ resonance at 12.7 MeV excitation energy in ^{12}C. The 1^+ resonance is known to be only 18.1(28) eV broad [KPS17], while the FWHM of the observed peak is 130 keV with a pronounced asymmetry. This gives us an indication of the resolution and response of the experimental setup and analysis. Furthermore, it is interesting to see that the 1^+ peak decays purely through ^{8}Be(ex.), which is expected because spin and parity conservation forces the decay to go through the first excited 2^+ state in ^{8}Be. A several MeV broad p̈eakät approximately 2.5-3 MeV is visible in

Cut	Remaining events
Initial	25 888 140
Matching	22 997 429
Three α's	1 150 403
Multiplicity	979 083
No U5 and U6	710 123
TDC cut	638 572
Energy-momentum cut	420 959
$E_{23} < 250$ keV	404 785
$E_{23} \geq 250$ keV	16 174

Table 7.1: *Remaining number of events after each cut in the data reduction procedure described in the previous sections.*

both ^{8}Be(peak) and ^{8}Be(ex.) spectra. The maximum The ^{8}Be(peak) contribution dominates in this region. However, the ^{8}Be(peak) spectrum falls off faster than ^{8}Be(ex.) toward higher energy, and at 5 MeV both spectra contribute roughly equally.

Figure 7.5 only includes information about the total energy of the event. A way to visualize correlations in the events is by plotting it in a so-called *Fynbo*-plot, where the energy of each α is plotted against the total energy of the event, as shown in fig. 7.6. Here we clearly see signs of very different decay mechanisms in the two spectra. For ^{8}Be(peak) decays, $E_{23} \approxeq 91.84$ keV and therefore the energy of the first emitted α is determined solely by the total available energy as

$$E_1 = \frac{2}{3}(E_{tot} - E_{23}). \tag{7.8}$$

The strong diagonal component in fig. 7.6 (Left) shows exactly that. The two secondary α-particles share the remaining energy, depending on the angle between the first and second α decay. This gives a broader energy distribution which corresponds to the broad component at lower single-particle energies in the same plot.

If we look at the ^{8}Be(ex.) decays in fig. 7.6 (Right), we immediately see two separate features in the spectrum. The 12.7 MeV resonance shows three distinct *blobs*, whereas the continuum below has no obvious structure, except the diagonal

upper line which is a result of the cut on E_{23}. The ^{8}Be(ex.) decays not going through the 1^{+} resonance are of particular interest. In the sequential picture, the understanding is that these events are a mixture of decays going through the ^{8}Be ground state *ghost* as well as decays going through the first excited 2^{+} state in ^{8}Be. Assuming one knows the level structure of ^{12}C, we can calculate the relative strength of the two contributions, but there is, unfortunately, no way to distinguish on an event-by-event basis with the information available in this experiment.

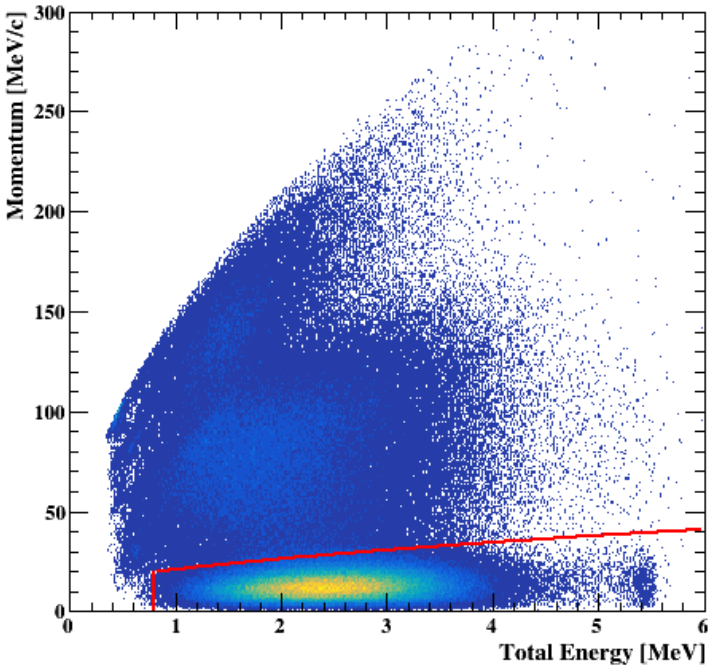

Figure 7.3: *Total momentum and energy for all possible triple-α-events. The red line corresponds to the cut in eqs.* (7.5) *and* (7.6).

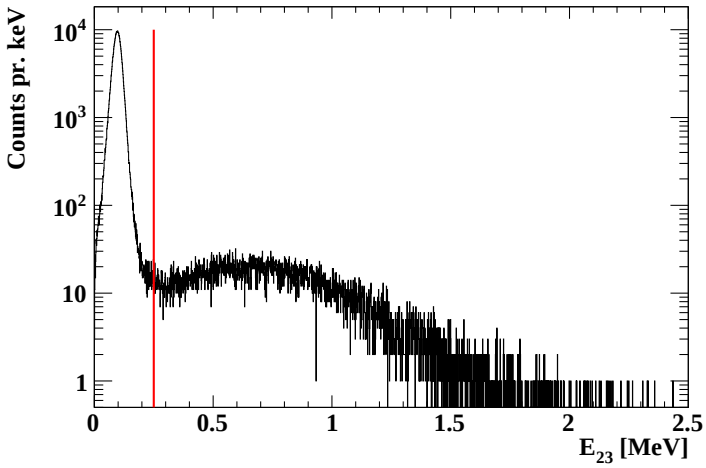

Figure 7.4: *Relative energy of two α-particles with least kinetic energy. The red line corresponds to E_{23} =250 keV.*

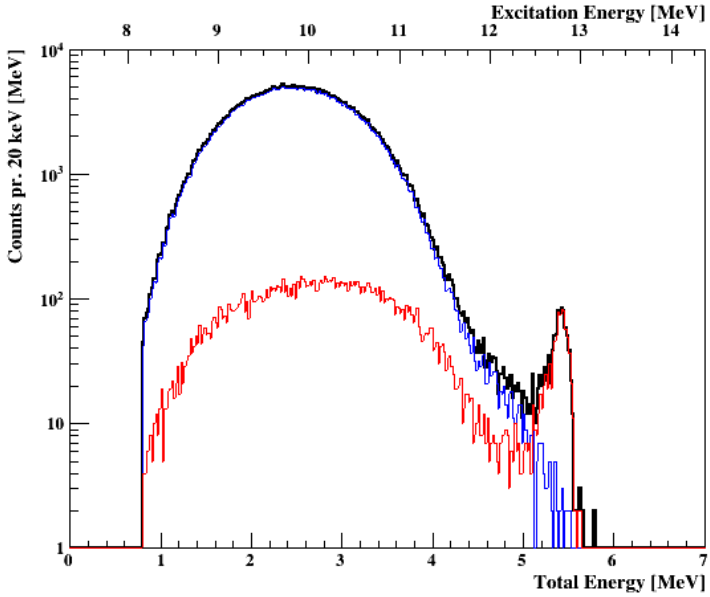

Figure 7.5: *Plot of the measured energy spectrum. The blue line is* ^{8}*Be(peak), the red line is* ^{8}*Be(ex.) and the black line is the sum of the two.*

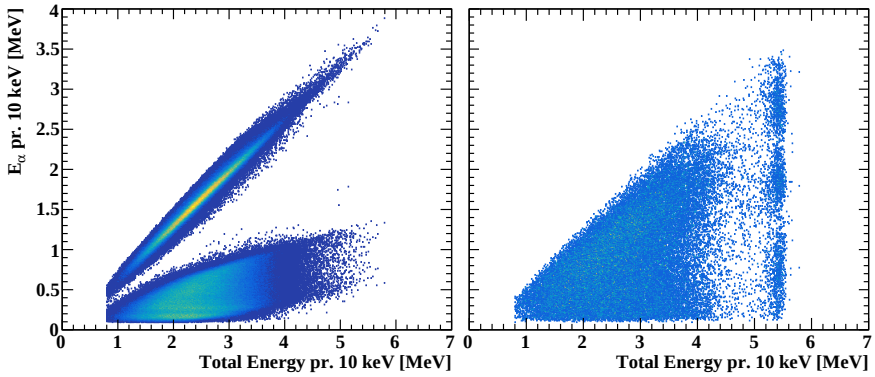

Figure 7.6: *Single* α *energy versus the total energy in the event. Note that each event contributes with three points in this plot.* ***(Left)*** ^{8}*Be(peak) decays.* ***(Right)*** ^{8}*Be(ex.) decays.*

CHAPTER 8

Simulation

As seen in the previous chapters, the response from the experimental setup and analysis of the events is far from trivial. The detection efficiency of a triple-α event is not just determined by the solid angle coverage of the detectors and the total energy, but also on the relative angles of emission, how the total energy is shared between the particles as well as the complex cuts placed in the analysis. Due to this, it is simply not practical, or even possible, to determine the detection efficiency analytically, and instead, we turn to Monte Carlo simulations.

This chapter is concerned with first making a realistic simulation and validating it on known examples, after which we can extract information such as background estimation and detection efficiencies.

8.1 Detector Response

A realistic simulation should be able to reproduce characteristics of the experiment such as resolution and the detector response line-shape, so the first step in the simulation is to include this. The final line-shape is a product of several physical and electronic effects, some of which are discussed in [Ten+04; Viñ+21]. When an α-particle hits the detector, it experiences some energy loss through the deadlayer depending on the incident angle and which part of the detector's microstructure it hits. The structure of a W1 DSSD is shown in

fig. 5.4b. Even if we know the exact place the particle hits and the amount of material is goes through before reaching the active region, the energy lost cannot be determined exactly due to *straggling*.

When the α enters the detecting region of the detector, the kinetic energy can be transferred to the detector in two ways. Most of the energy is transferred by electronic excitation, creating *electron-hole pairs* which are then separated by the bias voltage and the resulting current is then measured. This effect is a statistical effect, which on average requires ϵ =3.62 eV per electron-hole pair. Assuming this is a true Poissonian effect, the intrinsic spread is on the order of $\sqrt{(}N) = \sqrt{(}E/\epsilon)$, which for a 1 MeV α-particle is on the order of 2 keV. Secondly, the α can deposit energy in rare events through collisions with the silicon nuclei in the detector. In these cases some of the energy is lost to crystal defects and lattice vibrations.

The charge collected through the electron-hole pairs is then converted to a voltage in the pre-amplifier before being digitized in the ADC, and the detector signal is therefore folded with the resolution of the pre-amplifier/amplifier/ADC chain.

In G4Sim, the energy lost through the deadlayer and other non-active regions of the detector is calculated based on tabulated stopping powers from [Ber+16]. The energy deposited in a step inside the active region is evaluated using *G4Step::GetTotalEnergyDeposit()*, and is a sum of both ionizing- and non-ionizing energy loss. The broadening due to electronic noise is estimated for each detector by fitting a gaussian to pulser measurements. The result of this is σ_{el} ranging from 12 to 15 keV, which is then folded onto the simulated output.

A simulation of the α spectrum from the calibration source described in table 6.1, is shown with the corresponding calibration data in fig. 8.1. Both spectra are corrected for energy losses in the source itself and detector deadlayers, and is run through the same matching analysis.

It is evident from fig. 8.1 that the main features of the spectrum is quite well reproduced, especially the high energy tail and the broadening of the main peaks. However, the low energy tails are much less pronounced in the simulation than what is seen in the data. The third satellite peak at low energies correspond to events where the α-particles hit the aluminum grid on the detector. From the simulation, it seems like we underestimate the number of events where this happens. The broad tail at very low energy is also not reproduced in the

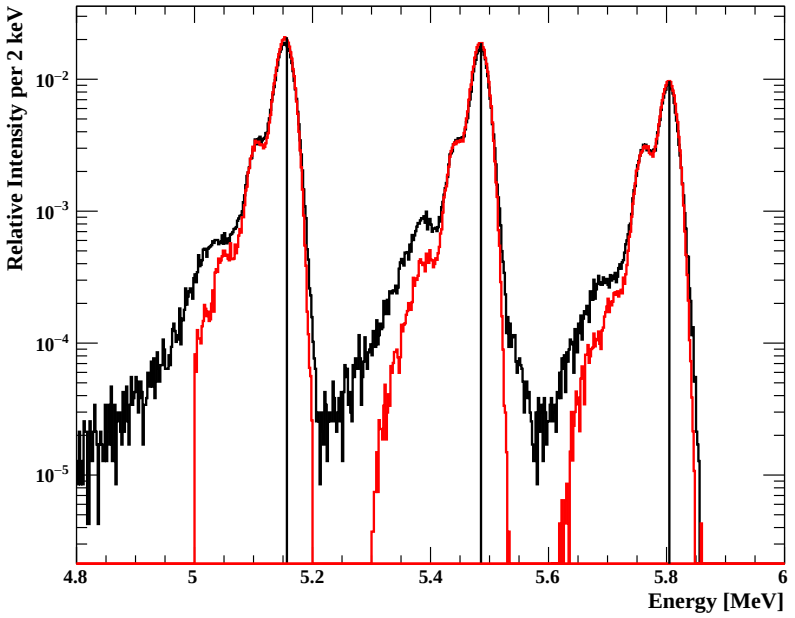

Figure 8.1: *Blue line shows the calibration data for U4 and red line is the simulation. Black vertical line shows the peak values from table 6.1.*

simulation. A similar issue has been reported in a previous experiment [Ref16], where the low-energy tail was significantly stronger than the prediction. It is speculated that an explanation could be that these low energy events are inter strip effects where some of the charge is captured in an anomalous electric field in the region between two strips.

Another, previously used, method to determine the detectors response function is to fit the parametrization in equation 11 of [BC87] to the α calibration peaks. The issue with this method is that the response function can only be determined for a specific energy corresponding to the calibration peak, which in this case is much larger than the typical energies measured in the triple-α decay. However, the stopping power of α-particles increases at lower energies and the energy loss is therefore underestimated. By simulating the response function in G4Sim, the energy dependence of the response is included.

8.2 Simulating triple-α events

In the previous section, we only really tested the detector response to a single α-particle. However, when simulating triple-α events effects such as the target, $\beta\nu$-recoil and decay point must also be included. The process of simulating a single event is the following:

1. Choose $Q_{3\alpha}$.
2. Determine Q_β and $\beta\nu$-recoil.
3. Generate 4-momenta for the three α-particles and the β.
4. Determine decay point.
5. Propagate particles through target and detectors.

Points 2 and 3 is done using a modified version of Sim3a [21b], which is a program written by J. Refsgaard, a former PhD student in the group, for the analysis of β-decay of ^{12}N. First the energy of the β-particle is drawn from the kinetic energy distribution found by Fermi's golden rule. Using available phase space as the density of states, this can be written as in section 7.1.1 in [Ref16] as:

$$W_T dT_\beta \sim \sqrt{T_\beta^2 + 2T_\beta m_\beta c^2}\left(T_\beta + m_\beta c^2\right)\left(Q_\beta - T_\beta\right) dT_\beta. \tag{8.1}$$

The polar and azimuthal angles of the β momentum are calculated as:

$$\theta_\beta = \cos^{-1}(2x - 1), \qquad \phi_\beta = 2\pi y, \tag{8.2}$$

where x and y are uniformly drawn numbers between 0 and 1.

The angular correlation between the anti-neutrino and the electron in a Gamow-Teller β-decay is shown in [Ham47] as:

$$W_\theta = 1 + \frac{1}{3}\frac{p_\beta}{T_\beta + m_\beta c^2}\cos\theta_{\beta\nu}. \tag{8.3}$$

The polar angle of the neutrino is drawn uniformly between 0 and 2π, while the polar angle with respect to the β momentum direction is sampled using ROOT's *TF1::GetRandom()* method on eq. (8.3).

With the momenta of both the neutrino and β known, the resulting recoil is added to ^{12}C, and the next step is to determine a 3α final state allowed by both

energy and momentum conservation. The ROOT library includes a method of generating n-body states in the *TGenPhaseSpace*. This method returns the four-momenta of the particles as well as the weight associated with the event such that, when sampled according to their weight, the generated events are uniformly distributed in phase space. The model-dependent weight is calculated using the Balamuth equation eq. (3.17), and by multiplying the two weights we get the final weight of the event. The event is then accepted or rejected based on von Neumann sampling [Neu51].

The decay point is determined by the beam shape and the implantation depth distribution. The implantation depth was simulated in SRIM and the depth can just be sampled from this. During the experiment we suspect the beam shape changed quite a bit, since the beam steerers and quadrupoles were tuned every hour or so and sometimes quite drastically and we therefore have no way of determining it. As a rough approximation the beam profile is chosen to be a uniform distribution within a circular plane with radius 5 mm which is the same as the collimator just outside the detector cube.

8.3 1^+ Resonance

Most of the triple-α spectrum is dominated by a broad continuum with little obvious structure. However, the 1^+ resonance at 12.71 MeV excitation energy in ^{12}C is narrow and can be used to test the triple-α simulation and analysis as well as the resulting resolution. Decays through the 1^+ resonance decays solely through the first excited state in ^{8}Be due to spin-conservation. Level parameters from [BAS06] are used to describe the first excited state in ^{8}Be with $E_{Be} = 3030\,\text{keV}$ and $\gamma^2 = 1075\,\text{keV}$. The black histogram in fig. 8.2 shows the experimental data with $E_{23} > 250\,\text{keV}$ and the red histogram shows a simulation of the 1^+ resonance, processed using the same analysis and identical cuts as the experimental data. The first thing to notice is that both the peak position and width are quite well reproduced. The FWHM of the simulation is slightly smaller at 124 keV compared to 130 keV for the experimental spectrum. However, the low energy tail of the experimental spectrum is much more pronounced than what is seen in the simulated spectrum. There are a few possible explanations for this. One could be that these events does not originate from the 1^+ resonance but instead from the even-spin continuum that dominates at lower energies. This it quite unlikely, though, since there are no other known states in this region that

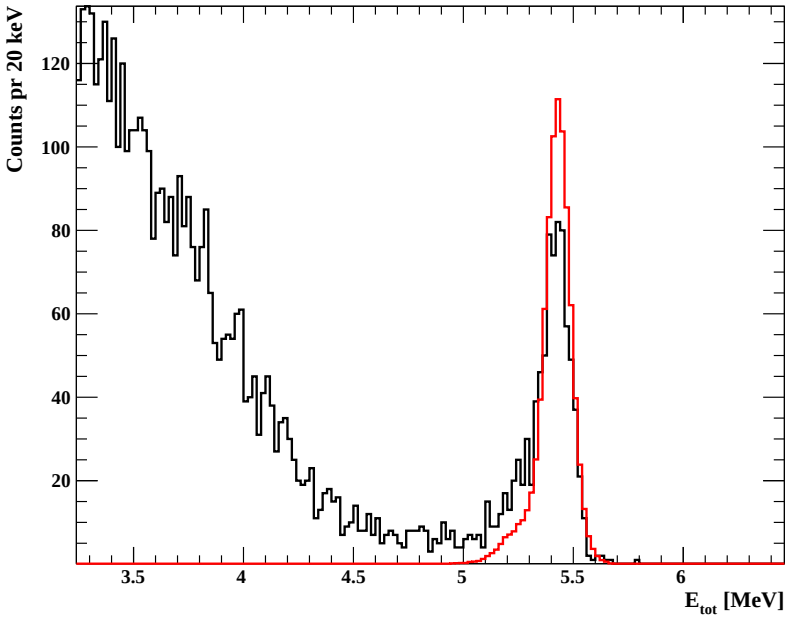

Figure 8.2: *Spectrum of* ^{8}*Be(ex.) in the region around* 12.71 MeV. *The black line is experimental data, and the red line is a simulation of the* 1^+ *resonance. See text for details.*

could contribute. The more likely explanation is that the low energy tail stems from events that experience a greater energy loss due to some experimental feature not fully understood. One reason could be that the catcher foil might be thicker in some areas than others. In that case, the same issue could explain the disagreement between the left and right detectors in fig. 6.4b. As a consequence, we must accept some uncertainty in the low-energy part of the simulated triple-α response.

8.4 Efficiency

After the previous sections it is now time to enjoy the fruits of our labor. The primary reason for the whole effort of simulating the experiment, is to account

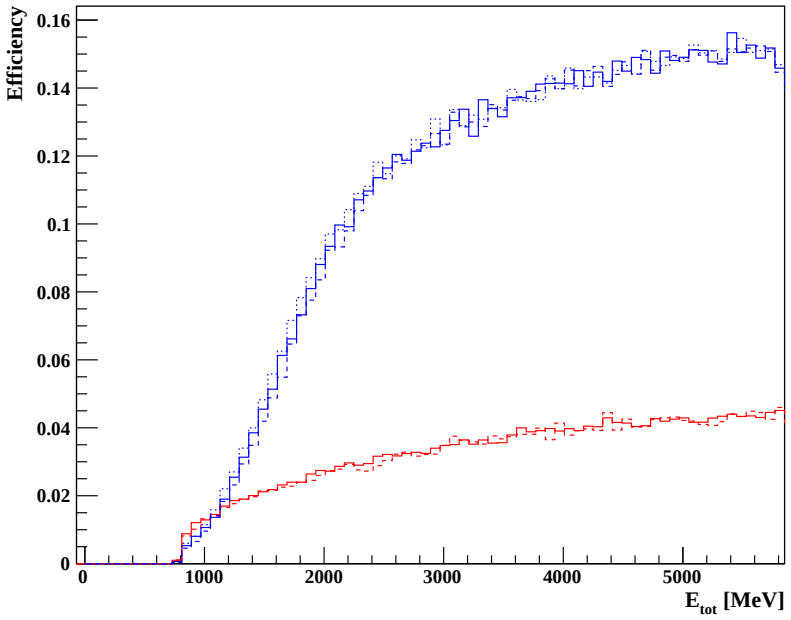

Figure 8.3: *Efficiency as a function of E_{tot}. Blue line is ^{8}Be(peak) decays, and red line is ^{8}Be(ex.) decays. Dashed and dotted lines correspond to simulations with foil thickness* ± 25 nm.

for the experiment-specific effects on the measured data. The most important effect to account for, is the setup-specific detection efficiency. Since the detection efficiency depends on the decay channel, the efficiency will be estimated separately for ^{8}Be(peak) and ^{8}Be(ex.).

8.4.1 Decays through ^{8}Be gs.

Estimating the detection efficiency for ^{8}Be(peak) is relatively simple, due to the extra constraint on the ^{8}Be excitation energy. 20×10^6 decays were simulated with a uniform E_{tot} distribution spanning the entire β window from 200 keV to 6100 keV. The resulting E_{tot} spectrum was then divided by the simulated E_{tot} distribution, and the result is shown in fig. 8.3. The efficiency vanishes quickly toward low values of E_{tot}. At higher energies, it keeps slowly increasing up to

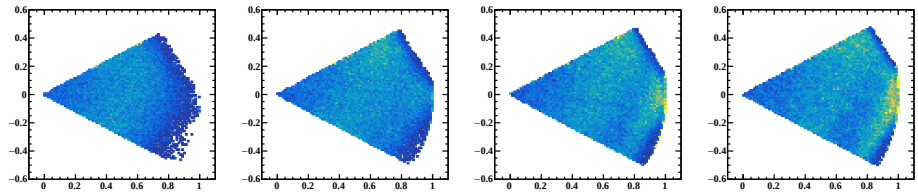

Figure 8.4: *Probability of detecting uniform phase space decays. The four figures are for increasing values of E_{tot}, starting at* 1 MeV *in intervals of* 1250 keV*. All figures share the same linear z-axis.*

approximately 15%. This effect can be explained qualitatively by the decay mechanisms. In the ^{8}Be center of mass frame, the two secondary α's only share 91.8 keV. Therefore, when the total energy of the decay increases, the opening angle between α_2 and α_3 becomes smaller, and are emitted more or less as a back-to-back decay with α_1. Since the detectors are placed in pairs directly opposite of eachother, this type of back-to-back emission is more likely to be detected. The uncertainty in foil thickness does have an effect on the simulated efficiency the order of 5% at low energy.

8.4.2 Decays through excited ^{8}Be

Finding the efficiency of detecting a ^{8}Be(ex.) decay is a bit more complicated due to the extra degree of freedom. The efficiency is not only dependent on E_{tot}, but also the Dalitz coordinates x and y. Uniform phase space decays were simulated with a uniform E_{tot} distribution. The events that survive the analysis and cuts described in chapter 7, are plottet into a 3-dimensional histogram. A 2D projection of this histogram is shown in fig. 8.4, where each plot correspond to a range in E_{tot}. The red line in fig. 8.3 shows a projection of fig. 8.4 onto the E_{tot} axis. It is clear to see that the efficiency of detecting uniform phase space decays is quite a bit lower than for ^{8}Be(peak) decays. This is due to the fact that when E_{23} increases, the opening angle of α_2 and α_3 increases, resulting in the opposite effect described previously for ^{8}Be(peak) decays.

Figure 8.4 shows that most of the phase space is relatively well covered, except for the upper and lower right corners where we have a *blind spots* - a region in phase space where we have no sensitivity. The blindness at the lower right corner

is a result of the cut placed on E_{23}. The upper right corner correspond to events with low E_3, and is therefore a direct consequence of the ADC thresholds. These blind spots are more pronounced at low energies. The rest of the phase space is relatively evenly covered by the experimental setup, except for the region at high energies near the circular edge of the Dalitz plot, where the acceptance rises. This region correspond to events where the α particles are emitted back-to-back.

8.5 Background Estimation

From fig. 7.3 it is clear that the momentum cut in eq. (7.5) cuts away most of the background events. However, it is still valuable to investigate the origin of these events as well as estimating how much of the background survives the cuts.

The three most obvious types of background due to wrongly identified coincidences are

1. Two α-particles and a β from the same decay.
2. Two α-particles and a β from an unrelated decay.
3. Two α-particles from one decay, and another α from an unrelated decay.

The first type of events can be estimated by simulations. We start by simulating ^{8}Be(peak) decays using the procedure described in section 8.2. The resulting energy-momentum plot of these events is shown in fig. 8.5a. It is straightforward to tag the β-particles that are treated as an α in the analysis. These events are shown in fig. 8.5b. There are two noticeable features in fig. 8.5b, which is the broad trapezoidal part in the middle of the plot, as well as a thin circular edge at large momenta. Both of these features are also visible in the data in fig. 7.3. The relative background contribution from β mixed events that survive the cuts from chapter 7 can now be easily extracted and is 1.0% for ^{8}Be(peak) decays.

The ^{8}Be(ex.) decays are simulated using a uniform phase space distribution as in the previous section. The resulting momentum-energy plots are shown in fig. 8.6a and fig. 8.6b. Here, the background contribution is broader with no distinct features. The background contribution from this type of decays is 1.3%. So, the background contribution from the first type of background events is on the order of $1\% - 1.5\%$.

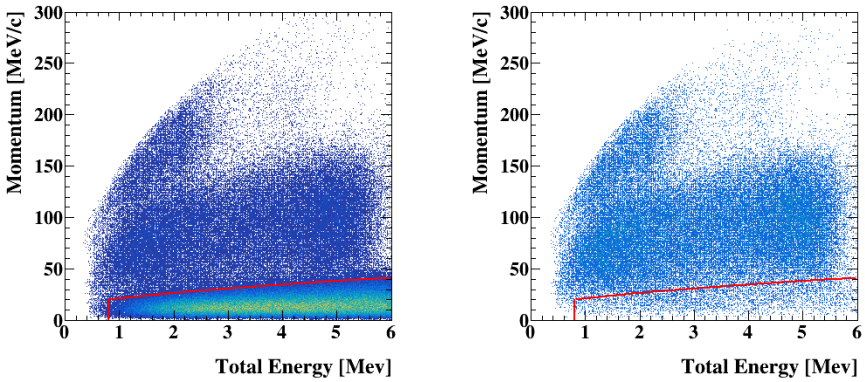

Figure 8.5: *Simulated ^{8}Be(peak) decays. The red line shows the energy momentum cut from eq.* (7.5) *and eq.* (7.6). ***(a)*** *All events.* ***(b)*** *Events with a β misidentified as an α.*

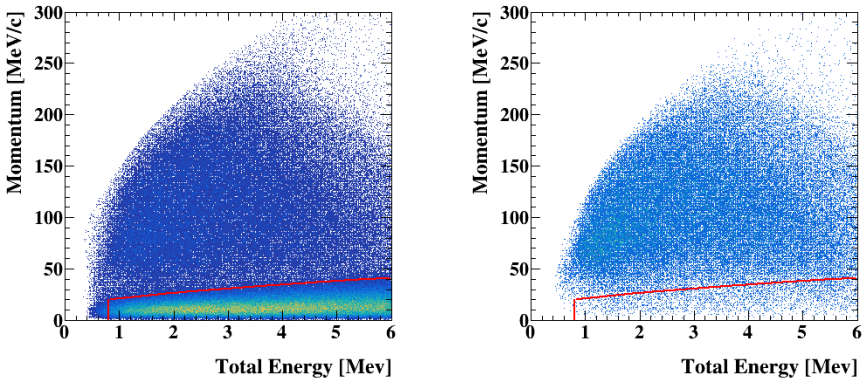

Figure 8.6: *Simulated uniform phase space decays. The red line shows the energy momentum cut from eq.* (7.5) *and eq.* (7.6). ***(a)*** *All events.* ***(b)*** *Events with a β misidentified as an α.*

The rate of β decays inside the chamber is calculated in section 9.1 to be 12.2 kHz on average. The ADC gate being 2.5 µs, the probability of having two β decays within the same ADC window can be calculated using a Poissonian distribution with expectation value $\lambda = 2.5\,\mu s \times 12.2\,kHz$ to be 3%. Assuming the background contribution of these events being similar to the first type of background events, the total background contribution is on the order of $3\% \times 1\% = 0.03\%$, and is clearly negligible.

The last type of background contribution is mixing with α-particles from an unrelated decay. The α decay branching ratio of ^{12}B β decay is 0.69% [Hyl+09], which means that the probability of this type of event happening is on the order of 50 times lower than unrelated β summing and therefore also negligible.

All in all, a conservative estimation of the background contribution after making the cuts presented in chapter 7 is below 1.5%.

CHAPTER 9

Analysis

After a careful calibration in chapter 6, identifying triple-α events in chapter 7, and estimating the detection efficiency in chapter 8, we are now ready to make it all come together to extract physics information from the data.

The main focus here is to resolve the broad continuum region in ^{12}C at 9-12 MeV. The latest evaluation [KPS17] still poses some questions about the recommended 0^+ and 2^+ resonances in this region. With improved statistics compared to previous studies of ^{12}B β decay and full kinematic information, the measurement from this work presents a much-improved way of understanding the resonances involved.

The analysis in this chapter is divided into several parts. First, the absolute yield of the experiment is determined in section 9.1. The spectrum from this study is then compared to previous similar measurements of both ^{12}B and ^{12}N β-decay in section 9.2. Sections 9.3 to 9.5 presents three different ways of analyzing parts of the spectra using R-Matrix theory. Lastly, the $\beta\alpha$ angular correlation is analyzed in section 9.6 in order to cross-check the findings from [Gar17].

9.1 Absolute Yield

The expression in eq. (3.17), includes the total number of β-decays in the experiment and since we have no information about the beam intensity, this number must be extracted through the data. The 1^+ resonance at 12.7 MeV excitation energy in ^{12}C presents one way of determining the yield since it's narrow and relatively easy to subtract from the total spectrum. The total yield in the experiment can be expressed as

$$N_\beta = \frac{n_{1^+}^{obs}}{\epsilon \mathrm{BR}_{1^+}} \frac{\Gamma}{\Gamma_\alpha}, \tag{9.1}$$

where $n_{1^+}^{obs}$ is the number of observed events in the 1^+ peak in the experimental spectrum, BR_{1^+} is the β decay branching ratio to the 1^+ resonance, $\frac{\Gamma_\alpha}{\Gamma} = 0.978(1)$ [KPS17] and ϵ the efficiency of accepting a true event. The efficiency is found by simulating 10^8 events generated with eq. (3.17), and applying the cuts described in chapter 7. BR_{1^+} is found in [Hyl+09] to be $2.8(2) \cdot 10^{-4}\%$ for the 1^+ resonance. The only thing left is to estimate N_{obs} to get the total yield.

The 12.7 MeV seen in fig. 8.2 resonance clearly dominates the spectrum at the peak energy, but there is a small background coming from the high energy tails of lower-lying even-spin resonances. To estimate the background, an exponential function is fitted to the spectrum from 4 MeV to 5 MeV, and integrated from 5 MeV to 6 MeV giving an estimated background contribution of 46 counts in that region. The number of observed counts in the same region is 853, and the resulting total yield is $N_\beta = 6.60 \times 10^9$ decays. By varying both the background fit-region and the peak boundaries by ± 100 keV, the total yield was found to agree within 4%. Combined with the statistical error, the total uncertainty on the yield is 6% which roughly the same as the quoted uncertainty on BR_{1^+}. The data used for this calculation was taken over a period of 150.3 h, which corresponds to an average rate of 12.2 kHz.

9.2 Experimental Results

Sometimes simplicity is bliss. So, before moving on to complicated R-matrix models, let us take a quick break and start by simply taking a careful look at the spectra.

9.2.1 Full spectrum

Experiment I257 is the latest in a campaign of experiments to investigate the continuum in ^{12}C [Fyn+05; Dig+09; Hyl+09; Ref16]. A natural first step is therefore to see how the spectra from this study compare to the previous experiments.

Four other spectra will be included in this section. The first is a measurement of ^{12}N β decay from IGISOL [Ref16] using a setup very similar to the setup in this experiment. The second is also from an experiment done at IGISOL measuring the decay of ^{12}B and ^{12}N in 2009 [Dig+09]. However, only the ^{12}B spectrum will be included here. The other two are both from an experiment performed at KVI [Hyl10; Hyl+09] measuring both ^{12}N and ^{12}B β decay. In the KVI experiment the radioactive isotopes were implanted into a DSSD and the total energy of the decay was then measured. The implantation experiments have the advantage that the detection efficiency is 100% except for at low energies, which means it is possible to get much more statistics and the results are less sensitive to systematic errors in the analysis. However, this simplicity does come with a price, namely that there is no information about the break-up mechanism. Also, the spectrum is shifted somewhat toward higher energy, since the β-particle deposits a small amount of energy in the detector. This shift is on the order of 20 keV to 50 keV. The spectrum from the present experiment is labeled I257. The other spectra are labeled IGI(^{12}N), IGI(^{12}B)[1], KVI(^{12}N) and KVI(^{12}B), respectively.

To compare the full spectrum from I257 to the implantation experiments, both the ^{8}Be(peak) and ^{8}Be(ex.) spectra are corrected individually for efficiency and then added. To allow direct comparison with the ^{12}N measurements, each dataset is also divided by the available phase space to get the ft value. All five spectra are shown in fig. 9.2.

There are a few things to note here. Firstly, looking at the 12.7 MeV peak, we see that both the peak position and width is very similar in the three IGISOL spectra, and the peak appears broader than in the two KVI spectra. The broadening is due to the fact that three individual particles are detected in the full kinematic experiments, so the resolution should be approximately $\sqrt{3}$ times worse just from the electronic noise alone. On top of this, the JYFL experiments

[1] Note that the IGI(^{12}B) spectrum is binned in 100 keV bins, while the other spectra are binned as shown in the figures.

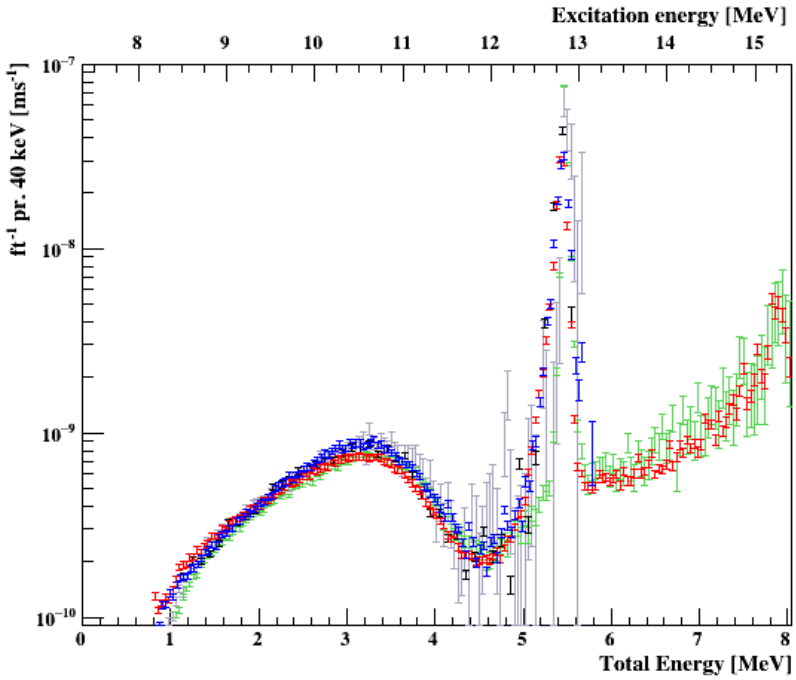

Figure 9.1: *Plot of ft^{-1} corrected for efficiency. Blue points are I257. The black points are IGI(^{12}N), red are IGI(^{12}B), green are KVI(^{12}N) and grey points are KVI(^{12}B).*

have additional broadening due to uncertainty in the energy-loss reconstruction. The peak energy is also located somewhat higher in the KVI data. This shift in peak energy was explained in [Hyl10] to be due to summing of the β energy.

In fig. 9.2 (top), the same spectrum is zoomed in on the continuum below the 12.7 MeV peak. Here, a systematic offset between the ^{12}B and ^{12}N spectra is clearly visible. This effect was shown in [Hyl+09] to be energy independent, which confirms the explanation from [DH 00; WA71] that the asymmetry is mainly due to nuclear structure and not second-class-currents.

Figure 9.2 (bottom) shows the I257 spectrum divided by the other two ^{12}B spectra. Note that the errorbars only indicate the error associated with the I257 spectrum, and it is therefore underestimated. The blue line corresponds to the

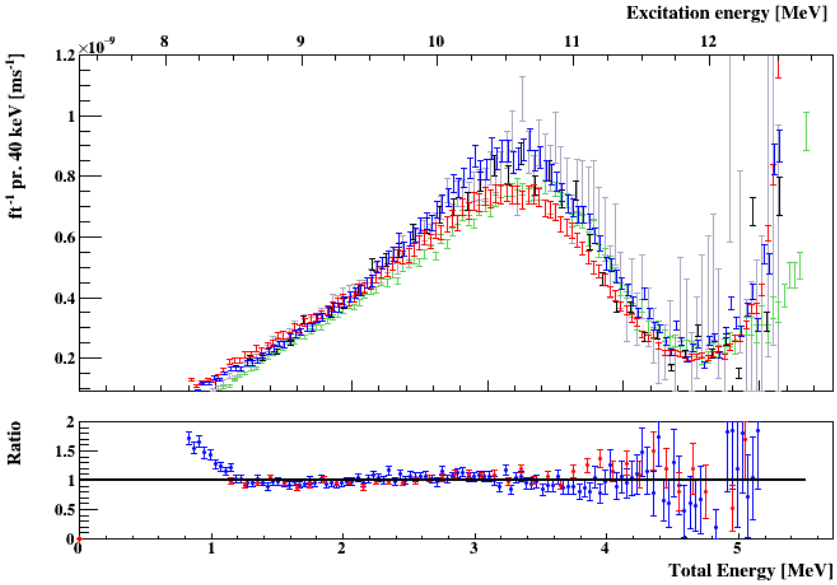

Figure 9.2: ***(Top)*** *Same plot as fig. 9.1 on linear scale and zoomed in on the region below the* 12.7 MeV *resonance.* ***(Bottom)*** *Blue points are I257 spectrum divided by KVI(^{12}B). Red points are I257 divided by IGI(^{12}B).*

I257 spectrum divided by KVI(^{12}B) and shows a clear systematic difference at low energy up to around 1.2 MeV. The efficiency for the I257 spectrum in this region is below 2% and the efficiency corrected spectrum is therefore very sensitive to even small systematic errors in the estimated efficiency. Due to the simple efficiency of the KVI data, I believe that the efficiency in this analysis is most likely underestimated below 1.2 MeV. At higher energies, the difference is within the estimated uncertainty. For the comparison with IGI(^{12}B), there is no significant energy-dependent systematic difference. As a result of fig. 9.2, the region below $E_{\mathrm{tot}} = 1.2$ MeV is excluded in the further analysis.

9.2.2 ^{8}Be(peak) decays

The separation into ^{8}Be(peak) and ^{8}Be(ex.) is not possible in the implantation experiments and, therefore, only the I257 and IGI(^{12}N) spectra are included in this section. The ^{8}Be(peak) spectra corrected for efficiency and β phase space are

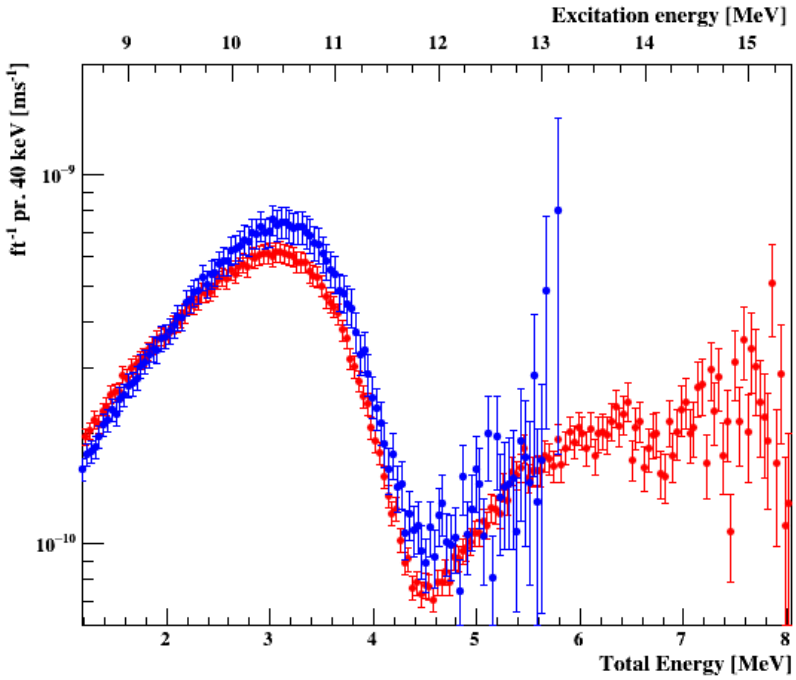

Figure 9.3: *Plot of ft^{-1}-value for ^{8}Be(peak) events corrected for efficiency. Blue circles are I257. The red circles are IGI(^{12}N).*

shown in fig. 9.3. Below 2 MeV total energy, the ft^{-1} value of IGI(^{12}N) is larger than that of I257, which is inconsistent with the asymmetry mentioned in the previous section. However, by comparing the IGI(^{12}N) and KVI(^{12}N) spectra in fig. 9.2, we see that the IGI(^{12}N) efficiency is most likely underestimated in this region. At energies above 4 MeV the β phase space starts to decrease rapidly for ^{12}B, and the statistics in I257 is therefore quite limited. Above 5 MeV, the β phase space varies extremely over a single energy bin, which is the reason for the large errorbars.

By factoring out the β phase space factor, a clearer picture of the nuclear resonances starts to emerge. Figure 9.3 shows a large asymmetric peak structure centered around 10.5 MeV excitation energy in ^{12}C. The low energy edge of the peak is enhanced, while the upper flange is suppressed. The same effect was

observed in [Fyn+05], albeit much less statistics, and it was attributed to interference between the Hoyle state and the 0_3^+ state. Figure 9.3 is a very clear illustration that interference plays a large part in describing the spectral shape in this region. The interference sign shifts at the resonance poles, and here we see that the two 0^+ states interfere constructively in between the poles, and destructively outside, i.e. above the 0_3^+ level.

From 4.5 MeV, the ft^{-1} starts to increase again. This region is usually concealed underneath the 12.7 MeV 1^+ level, but due to full kinematic measurements it is possible to gate on ^{8}Be(peak) decays, and thereby removing that background. The increase in ft^{-1} suggests that some other component starts to dominate at higher energy, however, based on the IGI(^{12}N) spectrum, there is no peak structure like one would expect from a resonance at higher energy. Instead, the value increases and then saturates. I have no clear explanation for this structure, but one could speculate that a different decay mechanism starts to play a role. Direct decays?

9.2.3 ^{8}Be(ex.) decays

A similar exercise as the one in the previous section can be made for the ^{8}Be(ex.) spectrum. Both spectra are corrected for efficiency, assuming uniform phase space distribution. The ft^{-1} value is shown in fig. 9.4, and the spectra are clearly in good agreement. Note that y-range in this plot is very large, and the mirror asymmetry is therefore not visible in this plot.

The most prominent feature is the 1^+ level at 12.7 MeV. Another narrow level is visible in the IGI(^{12}N) spectrum at 15.1 MeV excitation energy. This is the 1^+ isobaric analogue state which has isospin 1 and the α decay of this state is therefore isospin-forbidden. The reason we see it anyway, albeit weakly, is due to isospin mixing with the 12.7 MeV level [BZT74].

A peak at lower energy, similar to the one in fig. 9.3 is also seen, however the maximum is shifted up in energy, now at roughly 11.2 MeV excitation energy. Also, the steep slope on the high energy side due to interference between 0^+ levels is not visible in this spectrum.

Above the 12.7 MeV level, the IGI(^{12}N) spectrum does not saturate as in fig. 9.3. Instead, it increases up to the isobaric analogue state and above it. The upper flange of the 12.7 MeV level does not show signs of significant interference, so it is

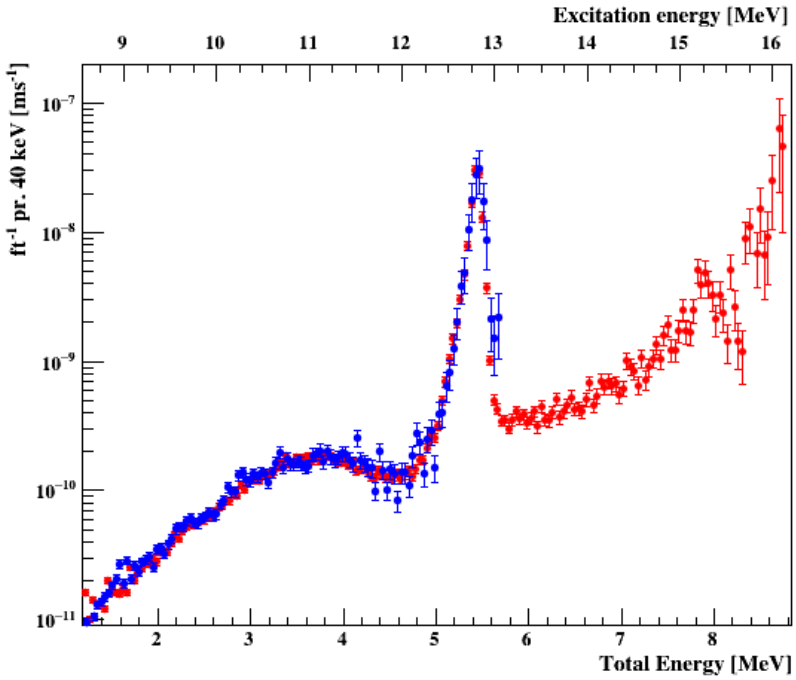

Figure 9.4: *Plot of ft^{-1}-value for ^{8}Be(ex.) events corrected for efficiency. Blue circles are I257. The red circles are IGI(^{12}N).*

likely that the strength in the region between the 1^+ levels and above the isobaric analogue state is due to some other structure. One explanation could be that it is the low-energy tail of a higher lying broad resonance. However, the only postulated broad spin 0^+, 1^+ or 2^+ resonance in this region is the 2^+ level at 15.44 MeV excitation energy with $\Gamma = 1770(200)$ keV [KPS17]. But since no peak is seen at 15.44 MeV, this seems unlikely.

So far, fig. 9.3 and fig. 9.4 have been treated independently. However, as discussed previously, a part of the ^{8}Be(ex.) spectrum belongs to the *ghost* of the ^{8}Be ground state and this part can be estimated based on the ^{8}Be(peak) spectrum. Figure 9.5 shows the fraction of all events going through the ^{8}Be(ex.)

channel as a function of total energy

$$\frac{N_{ex}(E)}{N_{gs}(E) + N_{ex}(E)}. \tag{9.2}$$

The data points are found by correcting both the ^{8}Be(peak), and ^{8}Be(ex.) spectra for acceptance and calculating the ratio going through ^{8}Be(ex.). By plotting the fraction of events going through ^{8}Be(ex.), the ^{12}B and ^{12}N asymmetry mentioned in the previous section is removed.

As in fig. 9.4, the 12.7 MeV level is clearly visible with the ratio going up to 1. At low energy, most events go through ^{8}Be(peak). This is fully in line with the expectation, since only the extreme tail of the ^{8}Be 2^+ level contributes here. At roughly 3.5 MeV something happens which dramatically increases the fraction of events going through ^{8}Be(ex.). This is roughly the region where the ^{8}Be 2^+ level starts to open up, so an increase is not surprising. There are no data above the 1^+ level for I257, but based on the IGI(^{12}N) spectrum it looks like, if the 1^+ level was removed, the plateau at 4.3 MeV continues until 6 MeV from where the ^{8}Be(ex.) fraction starts to increase again. An analysis of the Dalitz plots in [Ref16] showed that the region above the 1^+ level is dominated by decays through the $(j_a, l, j_b) = (0, 2, 2)$ and $(2, 2, 2)$ channels, which is consistent with the increase seen in fig. 9.5.

If we assume either pure 0^+ or 2^+ strength in ^{12}C, and only decays to ^{8}Be ground state through the $(0, 0, 0)$ or $(2, 2, 0)$ channels respectively, the peak-to-ghost ratio can be estimated by numerical integration of the Dalitz plots generated from eq. (3.17). The phase space is divided into two regions, separated at $E_{23} = 120$ keV to get the ^{8}Be(peak) and ^{8}Be(ex.) contributions, respectively, and the ratio can then be expressed as:

$$\text{ratio} = \frac{P^g_{000}}{P_{000}}, \tag{9.3}$$

where $P_{j_a l j_b}$ is the Balamuth weight integrated over all of phase space for channel (j_a, l, j_b). The superscripts g indicates a gate on the ^{8}Be ground state *ghost*. In this ratio, the dependency of the reduced width of the channel, as well as the β feeding is divided out. These ratios are shown as the black and purple solid lines in fig. 9.5 for pure 0^+ and 2^+ strength, respectively.

Below 2 MeV, there is an excess of ^{8}Be(ex.) decays compared to the expectation from the ^{8}Be ground state *ghost*. This excess was seen in similar plots in both

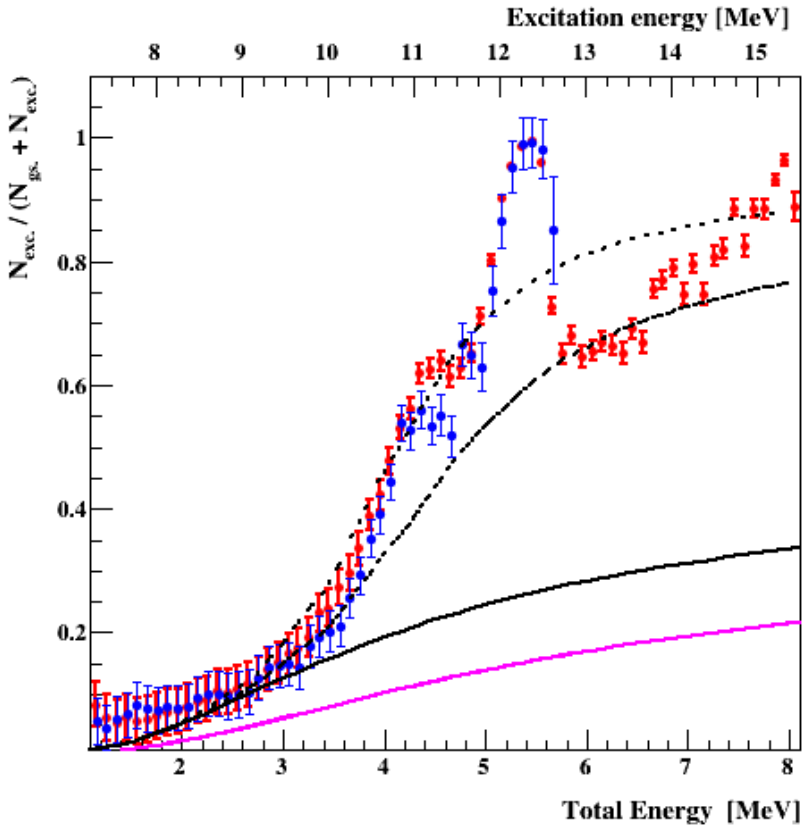

Figure 9.5: *Fraction of events going through ^{8}Be(ex.) as a function of total energy. The blue squares are data from I257, red squares is data from IGI(^{12}N). The black and purple lines are theoretical distributions assuming pure 0^+ and 2^+ strength, respectively. See text for details on the theoretical lines.*

[Dig+09; Ref16]. It would be surprising if decays through ^{8}Be(ex.) would become relatively more prominent at low energies, since the decay is only sensitive to the extreme low energy tail of the 2^+ state. In both [Dig+09; Ref16], the excess was attributed to badly estimated detection efficiencies. We note that the excess is within one σ errorbars of the ^{8}Be(peak) estimate and therefore consistent with this explanation. However, the fact that the data from I257 and IGI(^{12}N) agrees so well, and that the same feature is seen in three independent studies is quite curious.

From 2 MeV to 3 MeV, most of the ^{8}Be(ex.) spectrum can be described with pure 0^+ strength decaying through the ^{8}Be ground state ghost. This is in line with the results from section 9.4, where it is shown that this part of the spectrum is dominated by the Hoyle state ghost and another 0^+ level. At higher energy however, some additional contribution is required to describe the rapid increase in the ratio. As mentioned before, this region is roughly where one could expect the ^{8}Be 2^+ level to start contributing, so we can try to include this channel.

Starting with pure 0^+ strength in ^{12}C, the two allowed decay channels are $(0,0,0)$ and $(0,2,2)$. In the single-level approximation in ^{12}C, the $(0,2,2)$ reduced width can be expressed as the $(0,0,0)$ reduced width times a scalar, α_0. The ratio of ^{8}Be(ex.) and ^{8}Be(peak) decays is then:

$$\text{ratio} = \frac{P^g_{000} + \alpha_0 P_{022}}{P_{000} + \alpha_0 P_{022}}. \tag{9.4}$$

A plot with $\alpha_0 = 2$ and 5 are shown in fig. 9.5 as the dashed and dotted black lines. Increasing α_0 to 2, gives a good description of the data up to approximately 3.6 MeV, but it can not explain the full slope or the plateau at 4.3 MeV. Choosing $\alpha_0 = 5$ does increase the steepness of the slope, but the ratio is then overestimated between between 3 MeV and 4 MeV.

A similar test can be done assuming pure 2^+ strength in ^{12}C, however, this time there are three allowed channels, $(2,2,0)$, $(2,0,2)$ and $(2,2,2)$, which results in two free parameters. Variations of the two paremeters yielded a similar structure as the 0^+ plot, and no combination of parameters were able to reproduce the steep increase or the plateau at 4.3 MeV.

The conclusion from this simple model is that a single level in ^{12}C can not fully describe the β decay spectrum. Also, the ^{8}Be(2^+) level is too broad to give such a sudden and steep increase at 4 MeV, and does not reproduce the plateau at

4.3 MeV. The structure in fig. 9.5 therefore seems more likely to be a result of resonances in ^{12}C. In section 9.4 it is shown that most of the ^{8}Be(peak) spectrum is dominated by the Hoyle state ghost and another 0^+ resonance. If this is also the case for the ^{8}Be(ex.) spectrum, we can conclude that the second 0^+ resonance must have a stronger coupling to the $(0, 2, 2)$ channel than the Hoyle state, and that this 0^+_3 state should be located at roughly 11 MeV excitation energy.

9.3 Dalitz Fit

As shown in chapter 3, each decay channel has a distinct signature distribution in a Dalitz plot. The contributions from different channels can be estimated by fitting a linear combination of these Dalitz components to the experimental spectrum, as has been done previously for ^{12}N β decay in [Dig+09; Ref16]. However, due to the small branching ratio of states above the 3α threshold, previous studies of ^{12}B β decay has not been able to make this kind of analysis.

In this model, we assume that channels add incoherently, and the total Dalitz plot is a linear combination of the single-channel components

$$H_{i,j} = \sum_c x_c y_c(i,j), \tag{9.5}$$

where $y_c(i,j)$ is the weight in bin (i,j) of channel c and x_c is the weight of the channel and will be used as the fitting parameter.

The individual channel Dalitz distributions are found by calculating the decay weight from eq. (3.17) in every point in a Dalitz plot at a given excitation energy in ^{12}C, similar to the plots shown in fig. 3.3. Decays through the ^{8}Be ground state peak, i.e. bins that correspond to $E_{23} \leq 250$ keV, are excluded. The experimental acceptance is included by multiplying by the phase space efficiency found in section 8.4.2 in each bin, and lastly, the histogram is normalized to unit integral.

The experimental spectrum is divided into four ranges in E_{tot}, from 1.5 MeV to 2.5 MeV, 2.5 MeV to 3.5 MeV, 3.5 MeV to 5 MeV and 5.0 MeV to 6 MeV, and the Dalitz plots for each range is shown in fig. 9.7a. Figure 9.6 shows the Dalitz plots for all allowed decay channels in the same energy bins.

The minimization is done using the MIGRAD routine from the MINUIT2 library in ROOT [CER21]. Because some bins have few or no counts, a log-likelihood

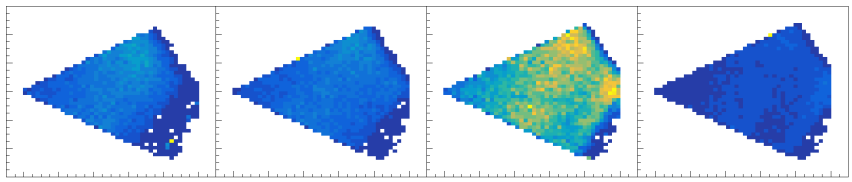

(a) *(0,0,0)*

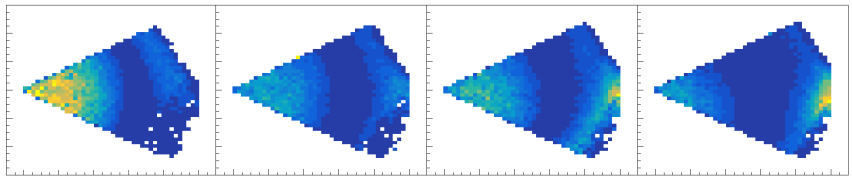

(b) *(0,2,2)*

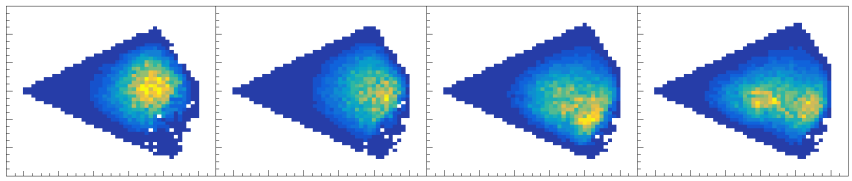

(c) *(1,2,2)*

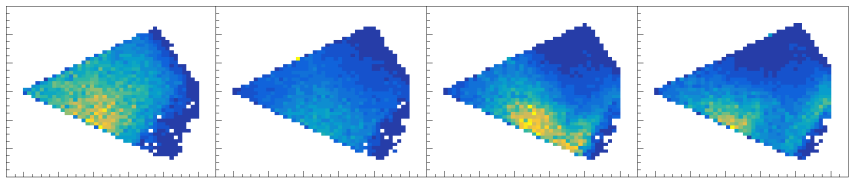

(d) *(2,0,2)*

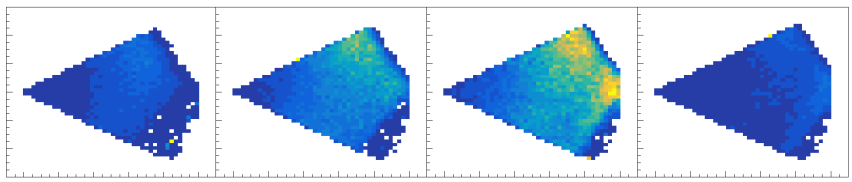

(e) *(2,2,0)*

Figure 9.6

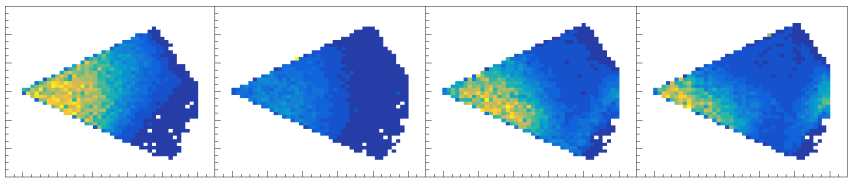

(f) *(2,2,2)*

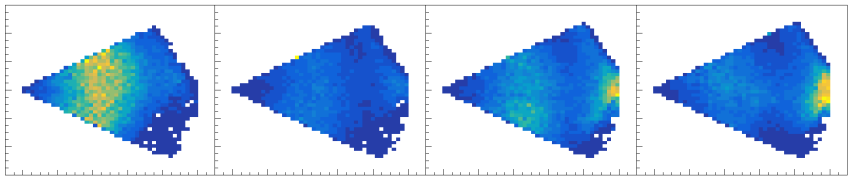

(g) *(2,4,2)*

Figure 9.6: *Dalitz plots for all allowed decay channels, including experimental acceptance. Each figure is labeled by* (j_a, l, j_b)*. For each channel, the figures from left to right correspond to* E_{tot} *=2 MeV, 3 MeV, 4 MeV, and 5 MeV.*

function is used as minimization function

$$\chi^2 = 2\sum_{i,j} n_{i,j} \ln\left(\frac{n_{i,j}}{H_{i,j}}\right) + H_{i,j} - n_{i,j}, \tag{9.6}$$

where $n_{i,j}$ is the observed counts in bin (i, j).

The fitted Dalitz plots are shown in fig. 9.7b and the channel weights are plotted in fig. 9.8a. Some channels converge toward zero in all fits, and were therefore not included in the plot. The included channels are (j_1, l, j_2)= $(0, 0, 0)$, $(1, 2, 2)$, $(2, 2, 0)$ and $(2, 0, 2)$. The way x_c is defined, the parameters can be interpreted as the number of counts going through each channel. These coefficients are shown in fig. 9.8a. However, this distribution is mostly determined by the available phase space. Figure 9.8b shows the same plot, except the fit coefficients has been normalized to 1, such that the coefficients shows the fraction of events in a single fit that goes through each channel.

Starting with the fit at highest energy, the Dalitz plot is described solely by the $(1, 2, 2)$ channel. This is of course expected since this region is completely dominated by the 1^+ state in ^{12}C.

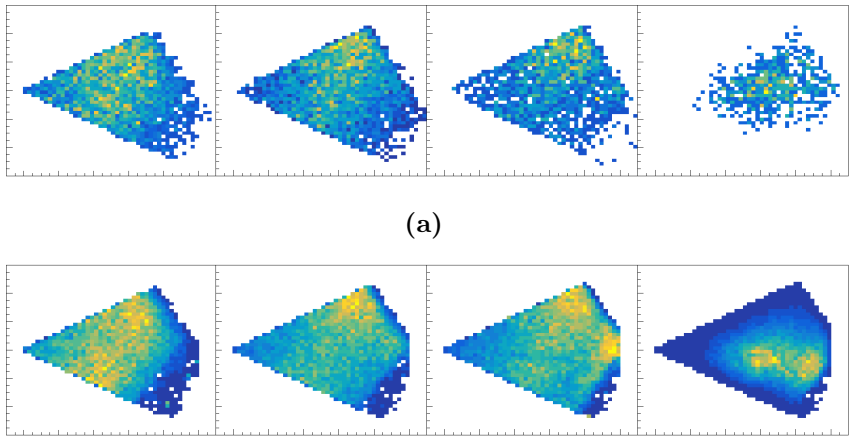

(a)

(b)

Figure 9.7: *(a) Experimental Dalitz plots. (b) Fitted linear combination of allowed decay channels. Fit coefficients are shown in fig. 9.8a.*

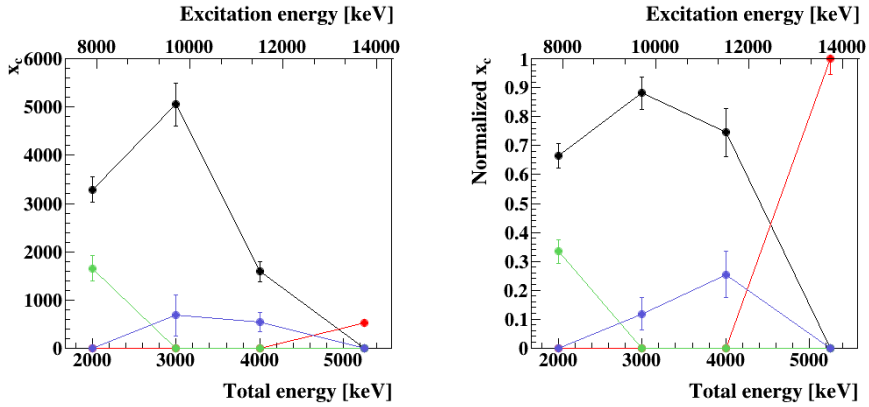

(a) **(b)**

Figure 9.8: *Parameters that converge toward 0 are excluded. Channel* $(0,0,0)$ *is marked by the black line,* $(1,2,2)$ *by the red line,* $(2,2,0)$ *by the purple line and channel* $(2,0,2)$ *is marked by the green line.* ***(a)*** *Fitted* x_c *coefficients as a function of* E_{tot}*.* ***(b)*** *Normalized fit coefficients.*

The fit at 2 MeV is quite surprising, due to the fact that the $(2, 0, 2)$ channel correspond to more than 30% of the events. It would be very surprising if, at low energy, decays through ^{8}Be(2^+) would become relatively more dominant compared to decays through the ^{8}Be ground state. A visual inspection of the measured and fitted Dalitz plots show a likely explanation. The $(2, 0, 2)$ channel is the only channel, where the primary strength lies in the lower left corner / center. In the $(0, 0, 0)$ and $(2, 2, 0)$ channels, the primary strength is located in the upper-most corner of the Dalitz plot, with a tail going down to the lower region. The measured Dalitz spectrum seems to be more or less evenly distributed along the y-axis, and pure ^{8}Be ground state contribution would therefore underestimate the strength in the lower part of the plot. The resulting fitted Dalitz plot show two distinct peaks, one at large y corresponding to the ^{8}Be ground state and one at low y from the $(2, 0, 2)$ channel. It therefore seems likely that the acceptance is badly estimated in this region, and the $(2, 0, 2)$ strength is an artifact of this. The same explanation could also explain the excess of ^{8}Be(ex.) events at low energy in fig. 9.5.

The fits at 3 MeV and 4 MeV indicate that the decays predominantly happen through the ^{8}Be ground state, and no evidence is seen for decays going through ^{8}Be(2^+). In both fits, there is a significant contribution from 2^+ strength in ^{12}C, and the fraction of decays going through ^{12}C 2^+ is larger at 4 MeV compared to 3 MeV. The fact that the ^{12}C(2^+) strength is described mostly by the $(2, 2, 0)$ channel is in agreement with [Zim+13] who observed the 2_2^+ level to decay primarily through ^{8}Be ground state with $L = 2$. This description is supported by a detailed analysis of the Dalitz distributions from ^{12}N β decay in [Ref16], which also showed the region to be dominated by decays through the $(0, 0, 0)$ and $(2, 2, 0)$ channels, with the $(2, 2, 0)$ channel becoming relatively stronger at 4 MeV.

9.4 R-Matrix Fit to ^{8}Be(peak)

In the previous section, the ^{8}Be(ex.) decays were used to estimate the amount of 0^+ and 2^+ strength as a function of excitation energy, based on a Dalitz plot analysis. In this section, the ^{8}Be(peak) decays will be used to test models including specific resonances, determining their energy, width and β strengths. The β delayed triple-α decays going through the ground state of ^{8}Be, can be treated as quasi two-body decay using the expression in eq. (2.27). To compare eq. (2.27) to the experimental spectrum, a few additional steps are needed. First

we need to include the experimental response function when calculating the total energy of a single event. Secondly the R-matrix spectrum must be multiplied by the efficiency from fig. 8.3. In practice, both of these steps are done by combining them into a response matrix and multiplying it onto the R-matrix spectrum. The E_{tot} response function is found by simulating ^{8}Be(peak) decays for each bin in the efficiency plot. The simulation is then run through the same analysis as the experimental data and the resulting E_{tot} histogram is then normalized to the efficiency in that bin.

The minimization is, once again, done using the MIGRAD routine from ROOT. A log-likelihood function is used as minimization function

$$\chi^2 = 2\sum_i n_i \ln\left(\frac{n_i}{y_i}\right) + y_i - n_i, \tag{9.7}$$

where n_i is the observed counts in bin i, and y_i is the R-matrix expression corrected for experimental effects. The fit is restricted to the range from 1.2 MeV to 6 MeV total energy.

The channel radius is calculated as

$$a_c = r_0\left(A_1^{1/3} + A_2^{1/3}\right), \tag{9.8}$$

where A_1 and A_2 are the mass numbers of the two particles in the outgoing channel and r_0 is chosen large enough to exclude any nuclear interaction in the external region. In these fits r_0 was chosen as 2.0 fm in the first breakup, and 1.8 fm in the second. The choice of r_0 might seem large, however, the Hoyle state is known to have a large spatial extension which necessitates a large inner region in the R-matrix model.

The last thing we need before fitting, is to renormalise the spectrum due to excluding the ^{8}Be ground state *ghost* in the ^{8}Be(peak) spectrum. According to [Hyl10], the ratio of events going through the ground state peak is

$$\frac{A_{\mathrm{peak}}}{A_{\mathrm{total}}} = \frac{1}{1 + \sum_c \gamma^2_{\lambda,c}\frac{\delta S}{\delta E}|_{E=E_\lambda}}. \tag{9.9}$$

In an R-matrix fit, everything can be fitted if enough resonances are added to the model. In this analysis, the models start as simple as possible, and more resonances are progressively added. The model configurations are shown in

Model	Configuration	$\frac{\chi^2}{ndf}$ Free Hoyle	$\frac{\chi^2}{ndf}$ Fixed Hoyle
0	0^+_H	$7.7 \cdot 10^4/479$	
1	$0^+_H + 0^+_1$	1070/476	4347/478
2	$0^+_H + 2^+_1$	6017/476	$2.2 \cdot 10^4/478$
3	$0^+_H + 0^+_1 + 2^+_1$	725/473	2142/475
4	$0^+_H + 0^+_1 + 0^+_{bg}$	669/473	1530/475
5	$0^+_H + 0^+_1 + 2^+_1 + 0^+_{bg}$	504/470	566/472
6	$0^+_H + 0^+_1 + 0^+_2 + 0^+_{bg}$	507/470	636/472
7	$0^+_H + 0^+_1 + 2^+_1 + 2^+_{bg}$	502/470	745/472
8	$0^+_H + 0^+_1 + 2^+_1 + 0^+_{bg} + 2^+_{bg}$	499/467	516/469

Table 9.1: *Table of models fitted to the ^{8}Be(peak) spectruma along with the resulting χ^2/ndf.*

table 9.1 along the with χ^2/ndf values. The number of free parameters in the fit, depends on the resonances included in the model. For each resonance there is a resonance energy, E_λ, β strength, g_λ, and the partial widths, $\gamma_{\lambda,c}$. For a 0^+ resonance in ^{12}C only the $(0,0,0)$ channel (Γ_{00}) is allowed by spin and parity conservation and therefore only one partial width. In the case of a 2^+ resonance the only allowed channel is $(2,2,0)$ (Γ_{20}). Unless otherwise noted, the initial parameters for all levels are $E_R = 10.5\,\text{MeV}$, $\Gamma = 1.5\,\text{MeV}$ and $B(GT) = 0.1$. For the ^{8}Be ground state, the resonance energy is 0 keV and the width is chosen as 5.57 eV based on [Til+04].

The following analysis is divided into two parts, one where all parameters are left as free parameters and one where the Hoyle state is fixed to literature values. The $\frac{\chi^2}{ndf}$ for all models in both cases are shown in table 9.1

9.4.1 Free Hoyle state

Although the Hoyle state is quite well known from previous studies, its role in ^{12}B β decay is not as clear. Historically, the accepted B(GT) value to the Hoyle state was measured by [MM62; GP63]. In [Hyl+09] this value was reduced by a factor of two and later validated in [Mun+16] and [Bis+20]. The width of the Hoyle state was updated in the latest evaluation by [KPS17], increasing the width by 10% compared to the previous evaluation from [Ajz90]. Due to these

uncertainties I have chosen to include a series of fits with the Hoyle state width and B(GT) as free parameters. These fits also give us a way to investigate how sensitive the spectrum is to the Hoyle state *ghost*.

Hoyle state only

It is, by now, well known that the Hoyle state can not describe the entire spectrum up to 12 MeV, however, the fit is included for completeness. The resonance energy is fixed to 7654 keV, while γ_{00} and B(GT) is left as fit parameters. The fit is shown as the solid green line in fig. 9.9, while the soli red line show a plot of the Hoyle state using literature parameters from [Til+04] B(GT)= 0.108 and $\Gamma_{00} = 9.3$ eV. Not surprisingly, the fit does not reproduce the spectral shape in any convincing way, which is also reflected in the χ^2 value.

Two levels

Models 1 and 2 include the Hoyle state and an additional 0^+ or 2^+ resonance, respectively. Resonances of identical spin and parity are added coherently in eq. (2.27), which gives rise to interference effects. In this case, the two 0^+ resonances interfere constructively in between the resonances, and destructively on the high energy side of the continuum. Models 1 and 2 show the need for interference between the Hoyle state and a 0^+_3 level to reproduce the steepness on the high energy side of the main peak. Based on this, we can conclude that the 0^+_3 level must be a part of any realistic model.

Three levels

Models 3 and 4 correspond to model 1 with another added 0^+ or 2^+ resonance and are shown in fig. 9.10. The χ^2 value is reduced significantly, and the region above 4 MeV is better described. There seems to be a minor sensitivity toward the spin of the third resonance, with a 0^+ resonance giving the best fit quality, however none of the models give the correct shape of the shoulder at 4.5 MeV.

Four and five levels

In models 5-7, yet another level is added and they each correspond to different combinations of spins. The χ^2 value for all these models are roughly equal, which can also be seen by visual inspection of fig. 9.11. The entire spectrum is well

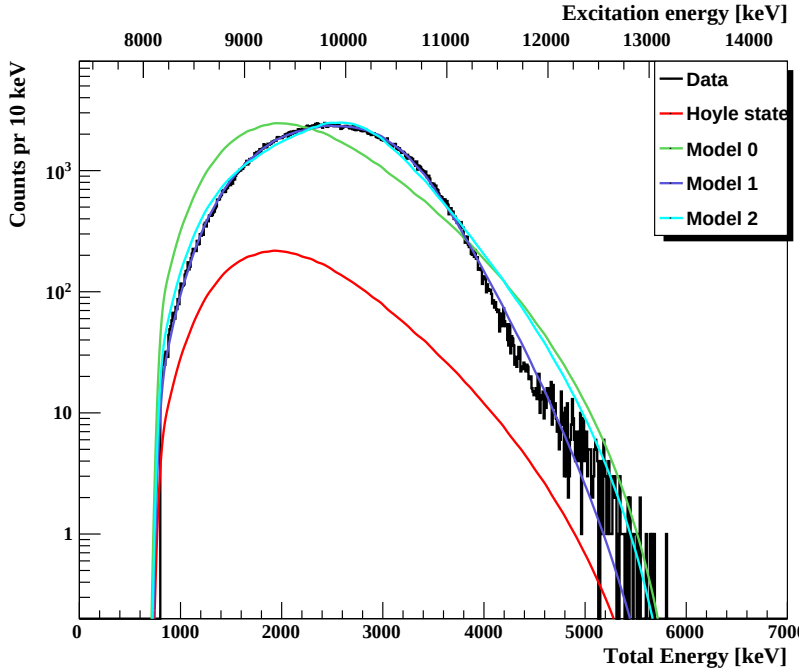

Figure 9.9: *R-matrix fit to ^{8}Be(peak) spectrum - models 0, 1 and 2 with free Hoyle state parameters. The solid red line is the expected contribution from the Hoyle state ghost.*

reproduced in all four-level models as well as model 8 which has five levels. The fitted resonance parameters are shown in table 9.2.

The uncertainties on the fit parameters in table 9.2 are on the order of 1-5%. However, they are not included since the model-dependent uncertainty far outweighs the fit errors and are therefore not very meaningful.

A common theme in all four models is the Hoyle state being much broader than the literature value of 9.3 eV from [KPS17]. Also, the B(GT) value is significantly larger in all models compared to 0.108 from [Hyl+09]. In model 7 the Hoyle state B(GT) is extremely large, which seems to suggest that at least two additional 0^+ resonances are needed. This effect is investigated in the next section.

Another interesting feature of these fits is the 0^+_3 resonance, which seems to be

Model	5	6	7	8
$E_{0_2^+}$ [MeV]	$7.654^\dagger$	$7.654^\dagger$	$7.654^\dagger$	$7.654^\dagger$
Γ_{00} [eV]	13.8	12.2	16.4	15.6
B(GT)	0.159	0.170	1.17	0.154
$E_{0_3^+}$ [MeV]	10.7	10.6	10.9	10.7
Γ_{00} [keV]	1182	1058	1730	1209
B(GT)	0.114	0.121	0.105	0.105
$E_{2_2^+}$ [MeV]	14.1		10.7	10.4
Γ_{20} [keV]	4217		1895	753
B(GT)	0.156		0.057	0.009
$E_{0_4^+}$ [MeV]	22.6	12.0		19.2
Γ_{00} [keV]	$1.8 \cdot 10^5$	1113		$1.2 \cdot 10^5$
B(GT)	0.001	0.019		10^{-9}
$E_{2_3^+}$ [MeV]			34.4	14.9
Γ_{20} [keV]			$3.4 \cdot 10^5$	2430
B(GT)			3.84	0.206
$E_{0_5^+}$ [MeV]		37.3		
Γ_{00} [keV]		$6.2 \cdot 10^5$		
B(GT)		0.030		
χ^2/ndf	504/470	507/470	502/470	499/467

Table 9.2: *Results for fits of models 5, 6, 7 and 8 to ^{8}Be(peak) spectrum using free Hoyle state parameters. Parameters with † were fixed in the fit. The uncertainties of the parameters are on the order of 1-5%, but are not quoted in the table. See the text for a discussion of these.*

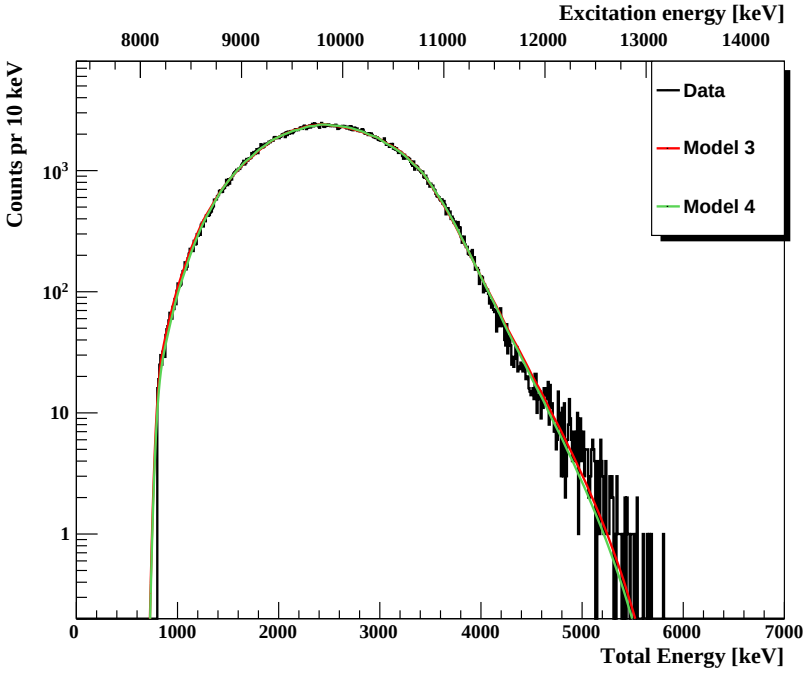

Figure 9.10: *R-matrix fit to ^{8}Be(peak) spectrum - models 3 and 4 with free Hoyle state parameters.*

relatively consistent in models 5, 6 and 8. The exception to this is model 7, but this is likely a result of the 0_3^+ having to add strength at higher energy - something which is achieved by a broad resonance at high energy in the other models. The average 0_3^+ parameters from models 5, 6 and 8 are $E_{0_3^+} = 10.7\,\mathrm{MeV}$, $\Gamma = 1150\,\mathrm{keV}$ and B(GT)$= 0.113$.

The properties of the 2_2^+ resonance seems to strongly depend on the model, and replacing it with another 0^+ resonance creates an equally good fit. It is therefore not possible to conclude even the existence of the 2_2^+ resonance based on these fits.

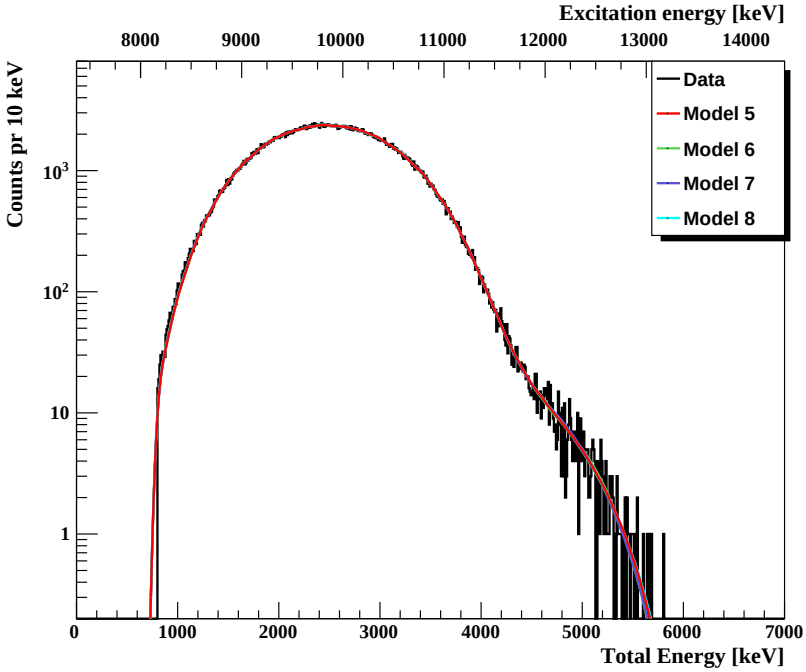

Figure 9.11: *R-matrix fit to ^{8}Be(peak) spectrum - models 5, 6, 7 and 8 with free Hoyle state parameters. Fit parameters are shown in table 9.2.*

9.4.2 Fixed Hoyle state

An obvious issue in all the previous fits is the Hoyle state. Both the fitted width and B(GT) values are too large compared to [KPS17]. In contrast to this experiment, [Hyl+09] measured the Hoyle state peak directly, whereas we are only sensitive to the *ghost* in this experiment. As such, their determination of the Hoyle state B(GT) is more reliable. To investigate the effect of this difference in the fits, the same series of fits were made with a fixed Hoyle state. The Hoyle state parameters were fixed as $E_R = 7.654\,\text{MeV}$, $\Gamma = 9.3\,\text{eV}$ [KPS17] and B(GT)$= 0.108$ [Hyl+09]. The χ^2 from these fits are shown in the last column in table 9.1.

In models 1-4, the same pattern repeats as in the fits with a free Hoyle state, albeit this time it is even more pronounced. It is clear that we need at least four

levels and that interference between the 0^+ resonances are needed to describe the spectrum.

Four and five levels

In the "Free Hoyle" fits, there was little or no sensitivity toward the spin of the resonances other than 0^+_3. However, when the Hoyle state is fixed we suddenly have a significant difference in χ^2 in models 5-7. Of the three, model 7 has the worst χ^2 which indicates that third 0^+ resonance is needed. The meaning of this resonance will be discussed later.

The difference in χ^2 between model 5 and 6 is quite interesting. The fact that model 5 is significantly better seems to indicate that a 2^+ resonance is indeed needed for a good fit and provides some of the first evidence for the 2^+_2 resonance in ^{12}B β decay. The resulting level parameters are shown in table 9.3, and the fit uncertainties are again left out for the same reason as in the previous section.

As was the case in the previous fits with fitted Hoyle state parameters, model 7 stands out from the others. In this fit the 0^+_3 resonance becomes extremely broad and is located at high energy, also, the fit quality is much worse than the other models. This suggests that there is some 0^+ strength that can not be described solely by the 0^+_3 resonance at 10-11 MeV. This could potentially be an indication of the same non-resonant contribution as seen in fig. 9.3.

Looking at models 5, 6 and 8, the 0^+_3 resonance energy is quite consistently determined, with a resonance energy at roughly 11.2 MeV excitation energy. The resonance energy found in these fits are fully compatible with the suggested resonance energy from [Hyl+10] listed in table 9.4. The width of the 0^+_3 resonance is not as model independent and is somewhat broader than what is found in [Hyl+10]. The B(GT) value varies a lot in the different models and it is therefore difficult to determine precisely. A similar model-dependency on the width and B(GT) value was found in [Hyl+10; Hyl10]. It is clear that when adding a 0^+_4 resonance, it tends to be a broad resonance at high energy. These types of R-matrix resonances, often referred to as background-poles, typically corresponds to an effective level that accounts for a continuum-like structure such as direct decays. For a discussion on these see chapter 5 of [Hyl10] and [Rii+15].

On the other hand, the 2^+_2 resonance seems to be much more model-dependent. In model 5 the entire 2^+ strength is modeled only through a single resonance,

Model	5	6	7	8
$E_{0_2^+}$ [MeV]	$7.654^\dagger$	$7.654^\dagger$	$7.654^\dagger$	$7.654^\dagger$
Γ_{00} [eV]	$9.3^\dagger$	$9.3^\dagger$	$9.3^\dagger$	$9.3^\dagger$
B(GT)	$0.108^\dagger$	$0.108^\dagger$	$0.108^\dagger$	$0.108^\dagger$
$E_{0_3^+}$ [MeV]	11.1	11.2	20.0	11.5
Γ_{00} [keV]	1837	2117	$3.2 \cdot 10^5$	2441
B(GT)	0.034	0.105	1.0	0.010
$E_{2_2^+}$ [MeV]	11.0		10.3	9.4
Γ_{20} [keV]	968		1173	687
B(GT)	0.044		0.087	0.001
$E_{0_4^+}$ [MeV]	40	14.0		40.0
Γ_{00} [keV]	1214	237		1180
B(GT)	791	10.8		1118
$E_{2_3^+}$ [MeV]			12.2	21.5
Γ_{20} [keV]			3259	$3.4 \cdot 10^5$
B(GT)			0.009	0.97
$E_{0_5^+}$ [MeV]		37.3		
Γ_{00} [keV]		23		
B(GT)		$6.2 \cdot 10^4$		
χ^2/ndf	566/472	636/472	745/472	516/469

Table 9.3: *Results for fits of models 5, 6, 7 and 8 to ^{8}Be(peak) spectrum. Parameters with † were fixed in the fit. The uncertainties of the parameters are on the order of 1-5%, but are not quoted in the table. See the text for a discussion of these.*

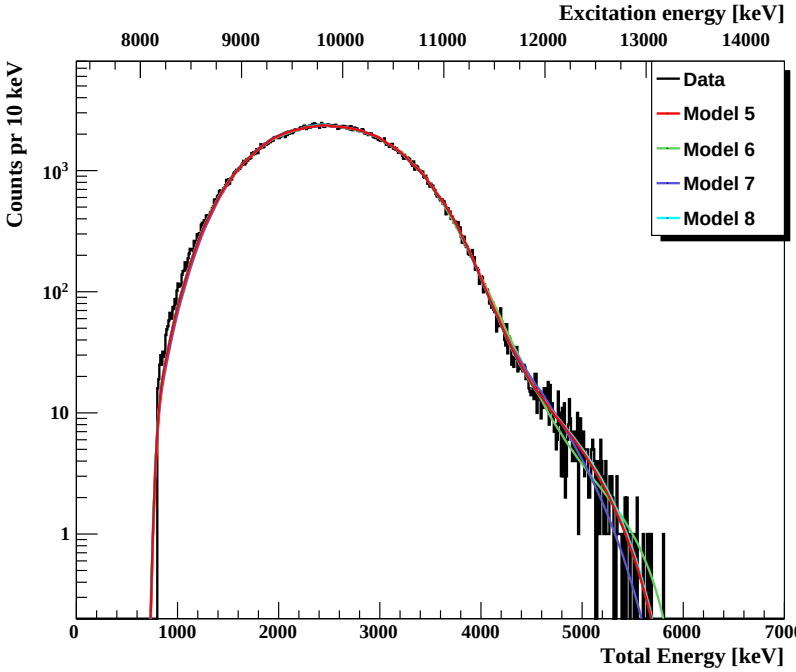

Figure 9.12: *R-matrix fit to ^{8}Be(peak) spectrum - models 5, 6, 7 and 8 with fixed Hoyle state parameters. Fit parameters are shown in table 9.3.*

whereas two 2^+ levels are included in models 7 and 8. The effect of adding two 2^+ levels is that the 2^+_2 level is pushed toward lower energy, while the high energy level becomes broad. The fit in model 8 seems to be consistent with a narrow level at 9.5-10 MeV as suggested by [Zim+13] and other reaction experiments, along with a background-pole at higher energy. Alternatively, if all the 2^+ strength modeled as a single level, as in model 5, the resonance is located at roughly the same energy as suggested by [Hyl+10]. This is quite surprising because the analysis in [Zim+13] includes only a single level, while the analysis in [Hyl+10] is a multi-level R-matrix fit with two 2^+ levels.

9.4.3 Summary

Let us summarize the findings so far in the analysis.

Resonance	E_R	Γ	B(GT)
0^+_H			0.108(3)
0^+_1	11.2(3) MeV	1.5(6) MeV	0.07(3)
2^+_1	11.1(3) MeV	1.4(4) MeV	0.06(4)

Table 9.4: *Table of resonance parameters from [Hyl+10] and [Hyl+09] for the Hoyle state and the recommended* 0^+_3 *and* 2^+_2 *resonances.*

1. Most of the main peak in the ^{8}Be(peak) spectrum can be described well using just two 0^+ resonances. The sensitivity to the spin of the second state comes from the fact that destructive interference is required to reproduce the steepness on the high energy side of the main peak.
2. When adding more than two 0^+ states, the models with fixed Hoyle state show sensitivity toward the spin of the third state with a better fit quality when including a 2^+ resonance.
3. An additional broad 0^+ resonance at high energy is also needed for an acceptable fit.
4. Adding more than three levels to the model significantly improves the fit quality indicating that the known 0^+_2, 0^+_3 and 2^+_2 resonances do not describe the full spectrum.

The recommended 0^+_3 resonance found in these fits is fully compatible with the recommendation from [Hyl+10] shown in table 9.4. Even though evidence is seen for a 2^+_2 resonance, its parameters can not be uniquely determined in this analysis.

9.5 Combined R-Matrix Fit

In the previous sections, the ^{8}Be(peak) and ^{8}Be(ex.) spectra were analyzed individually because there exists no combined R-matrix description. However, recently J. Refsgaard, a former PhD student in our group, K. Riisager and H.O.U. Fynbo have developed exactly such a R-matrix model. This model is not yet published or even fully proven, but it reduces to both partial models in separate limits. A rough overview of the model is given in section 9.5.1.

The limitations of both partial R-matrix models are discussed in section 3.3.3. A collective description of all parts of the β-delayed triple-α breakup presents a major advancement compared to the two separate models. As seen in [Hyl10; Hyl+10; Ref16] and the previous sections, a complicated many-level model is needed to reproduce the spectra, and overfitting quickly becomes an issue. Having a model that combines the different parts of the breakup allows us to put further constraints on a relatively featureless spectrum. Also, in order to understand the prominent structures in fig. 9.5, the ^{8}Be(peak) and ^{8}Be(ex.) channels must be combined.

There are still some parts of this analysis which is not completely understood, and the fit quality is generally very poor. The analysis in this section should therefore not be seen as a final result, but instead as a proof-of-concept of a novel method.

9.5.1 The theory

The reduced width amplitude from the known R-matrix expression in eq. (2.27) is multiplied by a breakup amplitude, which depends on kinematic variables

$$dN_c = f_\beta P_c \left| \sum_{\lambda\mu} B_\lambda \gamma_{\mu c} A^{j_a}_{\lambda\mu} \right|^2 dE \tag{9.10}$$

$$\rightarrow dN_c = f_\beta \left| \sum_{\lambda\mu} B_\lambda \gamma_{\mu c} A^{j_a}_{\lambda\mu} T_c^{J_a m_a}(E_1, E_{23}, \Omega_1, \Omega_{23}) \right|^2 dE, \tag{9.11}$$

where the breakup amplitude is separated by variables

$$T_c^{J_a m_a}(E_1, E_{23}, \Omega_1, \Omega_{23}) = D_l(E_1) \times F_{\lambda_b}(E_{23}) \times G^{J_a m_a}_{l\lambda_b}(\Omega_1, \Omega_{23}). \tag{9.12}$$

The three components are

$$D_l(E_1) = P_l^{1/2} e^{i(\omega_l - \phi_l)}, \tag{9.13}$$

$$F_{\lambda_b}(E_{23}) = \pi^{-1/2} \frac{\gamma_{\lambda_b} P_{l'}^{1/2} e^{i(\omega_{l'} - \phi_{l'})}}{E_{\lambda_b} - E_{23} - \Delta_{\lambda_b} - iP_{l'}\gamma^2_{\lambda_b}}, \tag{9.14}$$

$$\begin{aligned} G^{J_a m_a}_{l\lambda_b}(\Omega_1, \Omega_{23}) = (2J_a + 1)^{-1/2} \sum_{m_b} & \langle j_b l m_b (m_a - m_b) | j_a m_a \rangle \\ & \times \left[i^l Y_l^{m_a - m_b}(\Omega_1) \right] \left[i^{l'} Y_{l'}^{m_b}(\Omega_{23}) \right]. \end{aligned} \tag{9.15}$$

The Bose symmetrization is achieved by changing the variables from $d\theta_{23}dE_{23}$ to $dxdy$, since the x and y coordinates are independent of permutation. The total expression is then:

$$dN_c = 2\pi E^2 f_\beta \sum_{j_a m_a} (2j_a+1)^{-1} \left| \sum_{\lambda\mu} B_\lambda \gamma_{\mu c} A^{j_a}_{\lambda\mu} \frac{T_c^{J_a m_a}(E,x,y)}{(E_1 E_{23})^{\frac{1}{4}}} \right|^2 dE. \quad (9.16)$$

In practice when fitting, the two spectra are still separated. The expression used to fit the ^{8}Be(peak) spectrum is integrated over $dxdy$ such that

$$dN_c = f_\beta \sum_{j_a} \tilde{P}_c^{\,j_a} \left| \sum_{\lambda\mu} B_\lambda \gamma_{\mu c} A^{j_a}_{\lambda\mu} \right|^2 dE, \quad (9.17)$$

with

$$\tilde{P}_c^{\,j_a} = 2\pi E^2 \int (2j_a+1)^{-1} \left| \frac{T_c^{J_a m_a}(E,x,y)}{(E_1 E_{23})^{\frac{1}{4}}} \right|^2 dxdy. \quad (9.18)$$

This expression is then folded with the simulated response function and efficiency just like in section 9.4 to be able to compare to the experimental spectrum.

For the Dalitz distribution, the response is more complicated and should in principle be simulated based on the R-matrix model. However, such a task is computationally very demanding. Instead, we use the simulated uniform phase space distribution from section 8.4.2. The response is mostly flat or slowly varying in the Dalitz coordinates x and y. Early investigations by J. Refsgaard has shown that the change in χ^2 due to this approximation is on the order of 5-10%.

The full normalization of the ^{8}Be(ex.) spectrum is an ongoing issue at the time of writing. I have therefore chosen to let the integral of the ^{8}Be(ex.) spectrum be a free parameter. The same channel radii and ^{8}Be level parameters used in section 9.4 are used in the fits in this section. The Hoyle state parameters are also fixed to the values from section 9.4.2. The parameter Γ_{22} for the Hoyle state is fixed to zero. This assumption is not necessarily true, but it would be surprising if the channel $(0,2,2)$ contributes a lot.

9.5.2 Fits

The minimization is once again done using the MIGRAD routine from ROOT. The minimization function used for the ^{8}Be(peak) spectrum is the same as the

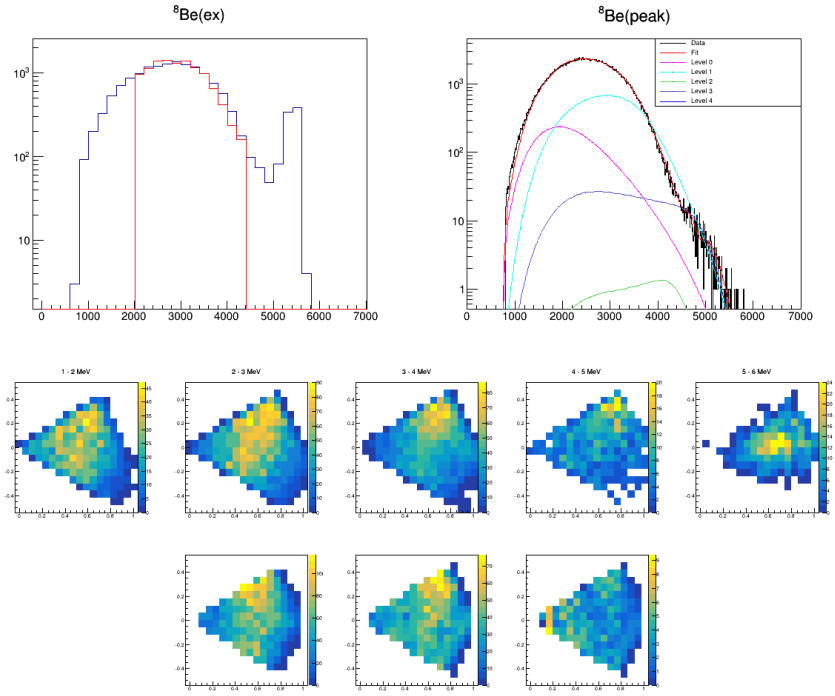

Figure 9.13: *Plot of combined fit to model 8. Upper right plot shows the ^{8}Be(peak) spectrum, upper left is the E_{tot}-projection of ^{8}Be(ex.) spectrum. Middle and bottom rows are measured and fitted Dalitz plots, respectively.*

one used in section 9.4. For the ^{8}Be(ex.) spectrum, the same log-likelihood function is summed for each bin in the (x, y, E_{tot}) spectrum. The ^{8}Be(ex.) spectrum is restricted to the range $2\,\text{MeV} \leq E_{\text{tot}} \leq 4.4\,\text{MeV}$. The low energy cut is to due to the issues discussed in section 9.2 and section 9.3, while the high energy cut is placed such that the 1^+ level is excluded.

The computational cost of evaluating the spectrum is each bin is quite demanding, even when using a uniform phase space distribution to estimate the ^{8}Be(ex.) acceptance. As a result, I have reduced the number of bins in the ^{8}Be(ex.) spectrum such that the x an y coordinates are binned in 0.05 intervals and the energy is binned in intervals of 200 keV. Even still, investigating a large parameter space such as model 8 in section 9.4 is a difficult task. As a

Model	5	6	7	8
$E_{0_2^+}$ [MeV]	$7.654^\dagger$	$7.654^\dagger$	$7.654^\dagger$	$7.654^\dagger$
Γ_{00} [eV]	$9.3^\dagger$	$9.3^\dagger$	$9.3^\dagger$	$9.3^\dagger$
Γ_{22} [eV]	$0^\dagger$	$0^\dagger$	$0^\dagger$	$0^\dagger$
B(GT)	$0.108^\dagger$	$0.108^\dagger$	$0.108^\dagger$	$0.108^\dagger$
$E_{0_3^+}$ [MeV]	11.06	10.95	11.10	11.09
Γ_{00} [keV]	1827	1540	3144	1871
Γ_{22} [keV]	129	109	146	121
B(GT)	0.138	0.138	0.151	0.133
$E_{2_2^+}$ [MeV]	11.57		11.01	11.86
Γ_{20} [keV]	962		171	928
Γ_{02} [keV]	4		1010	391
Γ_{22} [keV]	0		53	274
B(GT)	0.005		0.035	$9.5 \cdot 10^{-5}$
$E_{0_4^+}$ [MeV]	12.81	26.78		12.65
Γ_{00} [keV]	73	5357		205
Γ_{22} [keV]	2570	2500		2240
B(GT)	0.53	139		0.463
$E_{2_3^+}$ [MeV]			29.6	12.11
Γ_{20} [keV]			2390	2306
Γ_{02} [keV]			1726	68.0
Γ_{22} [keV]			$1.52 \cdot 10^3$	11.7
B(GT)			14.7	0.036
$E_{0_5^+}$ [MeV]		30.0		
Γ_{00} [keV]		16		
Γ_{22} [keV]		$2.6 \cdot 10^3$		
B(GT)		359		
χ^2/ndf ^{8}Be(peak)	696/461	775/461	1870/461	676/461
χ^2/ndf ^{8}Be(ex.)	5070/1614	5104/1614	5360/1614	5032/1614

Table 9.5: *Results for combined fit to models 5, 6, 7 and 8. Parameters with* † *are fixed in the fit. The partial widths are labeled for each channel as* Γ_{l,j_b}.

consequence I here present models 5-7 from section 9.4, as well as one example of a fit to model 8. However, time constraints has not allowed a full investigation of the parameter space, so the fit showed here could very well be a local minimum. The fit parameters are shown in table 9.5. The plot from model 8 is shown in fig. 9.13, while models 5-7 are shown in Appendix A. The plot in the upper-right corner is the ^{8}Be(peak) spectrum along with the total fit. The colored lines correspond to the single-level approximations of all levels in the model. The E_{tot}-projection of the ^{8}Be(ex.) spectrum is plotted in the upper-left corner as the blue line, with the R-matrix expression plotted as the red. For each bin in the E_{tot} plot, a Dalitz plot is generated and evaluated. However, the Dalitz plots in the lower two rows are binned in 1 MeV intervals. The middle row is data while the bottom row is the acceptance-corrected R-matrix generated Dalitz plots.

The χ^2 value for all models suggests that the fits are clearly not acceptable. The ^{8}Be(ex.) spectrum is responsible for most of the χ^2 contribution which is also seen when looking at the upper-left plot in fig. 9.13. The E_{tot} projection of the spectrum is quite poorly reproduced with the main peak in the fitted distribution being too narrow. This is the case in all four models. However, the shape of the Dalitz plots reproduces the main features quite well, except for the region above 4 MeV where a large contribution near $x = 0$ is seen in the fitted spectrum. Looking at fig. 9.6, we see that only the channels $(0, 2, 2)$ and $(2, 2, 2)$ has a strong contribution in this region. These channels are not included in the ^{8}Be(peak) spectrum, and any constraint on these parameters are therefore solely from the ^{8}Be(ex.) spectrum. One explanation could be that the ^{8}Be ground state channels are constrained by the ^{8}Be(peak) spectrum, and the ^{8}Be(2^+) channels are then enhanced to mimic the E_{tot}-projection without being very sensitive to the shape of the Dalitz plot in this region.

The level parameters shown in table 9.5 support this explanation quite well. The 0_3^+ level is very consistent in all models and is seen to primarily decay through the ^{8}Be ground state. The width and energy is fully consistent with the fits in section 9.4 as well as the values in table 9.4. The B(GT) value is constant in all models and a factor two larger than the value from table 9.4.

The 2_2^+ level is also almost identical to the resonance found in section 9.4, however it is located at slightly higher energy. In models 5 and 8, which have the best χ^2, the 2_2^+ level primarily decays through the ^{8}Be ground state, which is in line with the expectation from [Zim+13] and [Ref16]. The B(GT), however, is

poorly determined.

What is quite interesting, is that except for model 7, all models place the ^{8}Be(2^+) strength primarily in a 0^+ resonance. In models 5 and 8 this resonance is located just below 13 MeV, while the strength is attributed to a background-pole in model 6. This observation is fully in line width the explanation for the poorly reproduced Dalitz plot before. One could therefore hope that the determination of the 0^+_3 and 2^+_2 resonances are relatively robust despite the seemingly bad fit quality.

In fig. 9.5 a resonant-looking structure is seen at roughly 4.3 MeV total energy. Based on that figure, we should expect to see a resonance at roughly 11-11.5 MeV excitation energy with a significant decay branch through ^{8}Be(2^+). While the 2^+_2 resonance is located at this energy in the fits, it does not have any appreciable coupling to ^{8}Be(2^+) and can, therefore, not explain the structure in fig. 9.5. Note, that this is the same range where the E_{tot} projection of the ^{8}Be(ex.) spectrum is poorly reproduced, and the exact same region resulted in poor fits in [Ref16].

9.5.3 Limitations

As should be evident by now, the fits presented in this section are very ambitious. Even though the fit quality at the moment is not satisfactory, a qualitative analysis of the fits is quite promising. At the moment there are a few limitations and issues with the method, both theoretical as well as practical. On the theoretical side, an issue remains with the absolute normalization of the ^{8}Be(ex.) spectrum. Recent developments might have solved this already, but was not tested fully at the time of writing this thesis.

On the practial side, one issue is the poorly reproduced E_{tot}-projection of the ^{8}Be(ex.) spectrum. At the moment it is unclear whether this is due to an issue with the theoretical model or with the numerical implementation. As mentioned previously, the theoretical spectrum is multiplied by an acceptance matrix based on a uniform phase space distribution. The effect of using this acceptance is estimated but not fully understood at the moment. Also, the ^{8}Be(ex.) plot does not include any experimental response function such as the one used in the ^{8}Be(peak) plot. This response function is quite complex, since it must include the response in all three coordinates, i.e. (x,y,E_{tot}).

Another problem is the computational cost of these fits, especially when fitting a

complex model which seems to be needed to describe the spectra. Usual R-matrix fits are doable on a regular personal pc within a timeframe of an hour or so. However, the added cost of calculating the R-matrix amplitude in a three-dimensional spectrum increases the time needed by at least an order of magnitude, even after applying the simplifications presented in the previous section. With more than 10 free fit parameters, the process of finding the global minimum therefore becomes very time consuming. Other than using physical intuition to help guide the fit, one can also start with a simple ^{8}Be(peak)-fit as presented in section 9.4 to find approximate solutions for a subset of the fit parameters in order to minimize this issue.

9.6 $\beta - \alpha$ Angular Correlation

One of the motivations for doing this experiment was to evaluate the β-α angular correlation in the β decay of ^{12}B. In a previous study of ^{12}N β decay [Gar17], the β-α angular correlation showed strong anisotropy between 10 MeV and 11 MeV excitation energy. In [Gar17] this effect was attributed to the existence of the 2_2^+ resonance. The resonance energy and width found in their study is $E_R = 10.53$ MeV and $\Gamma_R = 1.35$ MeV. In this section the $\beta - \alpha$ angular correlation will be extracted and for both ^{12}B and ^{8}Li β decay, in an attempt to cross-check the results from [Gar17].

9.6.1 ^{8}Li β decay

In experiment I257, we included beamtime for measuring the β decay of ^{8}Li. The β-α angular correlation in the decay of ^{8}Li is known to be very nearly isotropic [TG75], and can be used to check that an isotropic angular distribution can be reconstructed using the simulation tool and analysis presented in this thesis. The β decay of ^{8}Li is simulated in similar fashion to the ^{12}B simulations described in section 8.2, and I will therefore only give a short overview of the process. The simulated events are generated as:

1. Sample ^{8}Be excitation energy, E_{ex}.
2. Generate β momentum from eq. (8.1) and an isotropic angular distribution.
3. Generate $\beta\nu$ recoil from eq. (8.2).

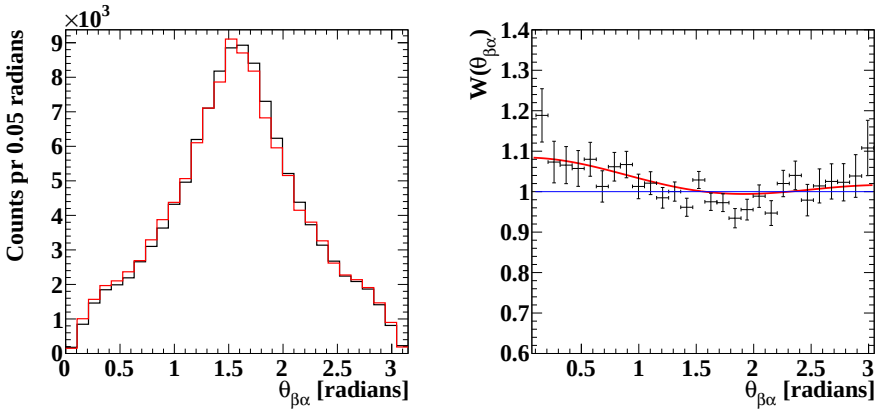

(a) (b)

Figure 9.14: *$\beta - \alpha$ correlations for ^{8}Li decays with 6 MeV $\leq E_{ex} \leq$ 8 MeV* ***(a)*** *Histogram of $\theta_{\beta\alpha}$. Black line is experimental data and red line is simulated.* ***(b)*** *Correlation plot. Red line is best fit to eq.* (2.19).

4. Generate two α-particles back-to-back in center-of-mass frame and apply recoil.

The particle identification and coincidence analysis is the same as described in chapter 7, except the coincidence criteria has been modified to include only two α's and the momentum cut was changed to

$$|\sum_i \vec{p_i}| \leq 40\,\text{MeV/c}. \tag{9.19}$$

If two α-particles and a β are detected, the angle $\theta_{\beta\alpha_i}$ between either α and the β is saved. This spectrum is shown in fig. 9.14a for 6 MeV $\leq E_{ex} \leq$ 8 MeV, where the black line shows the experimental spectrum and the red line shows the simulation. By dividing the two spectra, we get the angular correlation plot which is shown in fig. 9.14b. The red line is a fit to eq. (2.19), with parameters $A_0 = 0.034(11)$ and $B_0 = 0.050(15)$ and $\chi^2/ndf = 34.0/30$. The average kinetic energy of the β-particle in this region is calculated using eq. (8.1), to be $\langle T_\beta \rangle = 5.3$ MeV. Literature values for $A_0/\langle T_\beta \rangle$ and $B_0/\langle T_\beta \rangle$ are found in [Eic+66] and shown in table 9.6.

Parameter	R. E. Tribble *et al.*	This work
$A_0/\langle T_\beta \rangle$	$-7.92(20) \cdot 10^{-3}$	$6.4(20) \cdot 10^{-3}$
$B_0/\langle T_\beta \rangle$	$3.55(87) \cdot 10^{-3}$	$9.4(30) \cdot 10^{-3}$

Table 9.6: *Angular correlation parameters for eq.* (2.19). *Literature values found in [TG75] and shown for* $\langle T_\beta \rangle = 4.9\,\mathrm{MeV}$.

It is evident that the fit parameters found here are not compatible with the literature values. The most prominent difference is the sign of the parameter A_0, which is wrong. This parameter is determined by the recoil of the daughter nucleus in the β-decay and must be negative, which means that the structure in the angular correlation is most likely dominated by systematic uncertainties in the analysis. Due to this, we should not expect the parameter B_0 to solely describe the theoretical $\cos^2$ term. What we instead can do, it to use this analysis as a baseline estimation for the precision at which we can hope to extract angular correlation information in the ^{12}B decay. Both the paramaters A_0 and B_0 are on the order of 10^{-2}, so any anisotropic correlation found in the ^{12}B analysis at or below this level is therefore not significant.

9.6.2 ^{12}B β decay

The $\beta - \alpha$ angular correlation function of the ^{12}B β decay is found in a similar fashion as for ^{8}Li. Due to the difference in acceptance for different decay channels, the data is gated on ^{8}Be(peak) events, such that only the channels $(0, 0, 0)$ and $(2, 2, 0)$ contribute. An isotropic β distribution is estimated by simulating ^{8}Be(peak) events as a function of ^{12}C excitation energy with an isotropic β emission. Both the simulated and experimental data is then run through the analysis from chapter 7, where $\theta_{\beta\alpha}$ is calculated as the angle between the β and the highest energy α-particle.

The data is then divided into six bins based on the excitation energy in ^{12}C. For the lowest energy bins, a difference was seen in the (θ, ϕ) distribution of triple-α events between the experimental and the simulated data. Fewer events where the secondary, low-energy, α-particles had to travel through the catcher foil, was seen in the experimental data. This is most likely a result of a poorly estimated foil thickness or an un-even foil, and is similarly seen in fig. 6.4b. Again, the same

effect could be the reason for the poorly reproduced Dalitz plots at low energy in section 9.3.

We can try to account for the error by correcting the simulated data for each of the seven energy bins. The simulated data, gated on a β-particle, is plotted in a 3-dimensional histogram with coordinates $(\theta, \phi, \theta_{\beta\alpha})$, where θ and ϕ are the polar and azimuthal angles. Each point in this histogram is then corrected by a factor

$$\epsilon(\theta, \phi, \theta_{\beta\alpha}) = \frac{\int n_{3\alpha,obs}(\theta, \phi, \theta_{\beta\alpha}) d\theta d\phi}{\int n_{3\alpha,sim}(\theta, \phi, \theta_{\beta\alpha}) d\theta d\phi}, \tag{9.20}$$

where $n_{3\alpha}(\theta, \phi)$ is the observed number of all triple-α events as a function of θ and ϕ, without gating on a β-particle. This correction does not have any appreciable effect on the fits above 9.5 MeV.

The angular correlation function is then found by dividing the measured and simulated $\theta_{\beta\alpha}$ histograms. An example of this is shown in fig. 9.15b together with a fit to eq. (2.18). The χ^2/ndf values of the fits range from 0.98 to 1.15. The fitted A_2 coefficients are plotted as the black squares in fig. 9.15a. The errorbars reflect the uncertainty of the fit, as well as the estimated uncertainty associated with the correction mentioned above.

The red squares in fig. 9.15a are values fitted from ^{12}N data and presented in [Gar17]. The anisotropy coefficients are not as precisely determined in the present study, in part due to the previously mentioned correction and due to less statistics in the high energy region. However, they are consistent with the results from [Gar17]. The systematic uncertainty estimated from ^{8}Li β decay is on the order of 10^{-2}. Taking this into account, the region between 9.5 MeV and 11 MeV still shows a significant difference from isotropy with the points being 2.5-3 standard deviations from zero. This region is also the most well determined, since it has the most statistics and the correction is negligible. The remaining points are all consistent with both isotropy as well as with the measurement from [Gar17].

The origin of the, now confirmed, anisotropy is still not quite understood. As mentioned previously the explanation presented in [Gar17] is that second-forbidden transitions to the 2_2^+ resonance are enhanced due to nuclear structure differences between the mother and daughter states.

Another possible explanation for this could be a weak population of the 1^- level

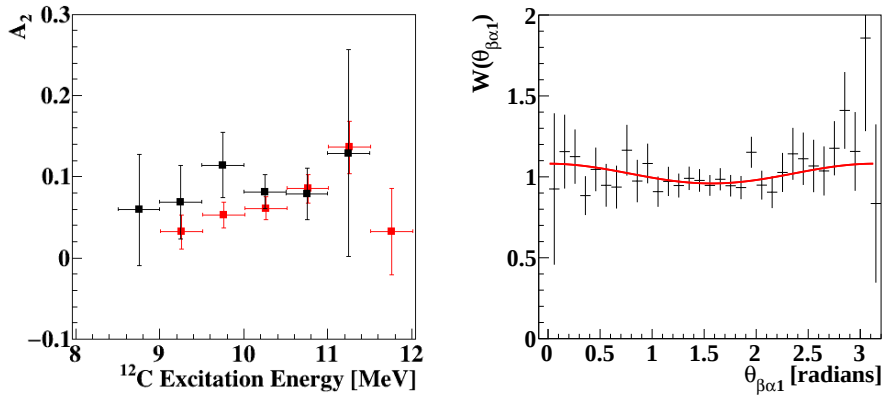

(a) (b)

Figure 9.15: *βα correlations for* ^{12}B *β-decays* ***(a)*** *Fitted values of* A_2 *as a function of* ^{12}C *excitation energy.* ***(b)*** *Correlation plot for* ^{12}C *excitation energy between* 10 MeV *and* 10.5 MeV. *Red line is best fit to eq.* (2.18)*, with* $A_2 = 0.13(12)$.

located at 10.84 MeV through a first-forbidden transition. The $\log ft$ values for first-forbidden transitions can for light nuclei be as low as 6 [Sin+98], and in such a case the 1^- level could potentially contribute significantly to the observed $\beta - \alpha$ angular correlation. If this is the case, then the level should be seen in the energy spectrum, and an R-matrix fit including such a 1^- level to fig. 9.3 could potentially be used to give an upper limit of the anisotropy from the 1^- level. Theoretical calculations of these first-forbidden transitions would be very beneficial in order to resolve the observed anisotropy.

CHAPTER 10

Conclusion and Outlook

The present work aimed to decipher the broad resonant structures around 9-11 MeV in ^{12}C. A major motivation for this is an identification of the 2^+_2 state, first predicted by [Mor56] in 1956 and recently observed by [Zim+13; Hyl+10; Gar17]. Another goal of this work was to provide a cross-check on the unexpected anisotropy seen in a complementary measurement of ^{12}N β-decay and presented in [Gar17].

To achieve these goals, an experiment was planned to populate excited states in ^{12}C through β decay of ^{12}B. The β-decay selection rules provide a unique way of eliminating unwanted background contributions from narrow levels in the region of interest. The β-delayed triple-α decay of ^{12}C was measured in full kinematics, giving information about not only the ^{12}C excitation energy but also the decay mechanism.

A new experimental setup was designed and constructed for this experiment, consisting of six closely packed segmented silicon detectors providing a large solid angle coverage with both energy and position information. Of these six detectors, two were 1 mm variants to allow identification of outgoing β-particles. The experiment was carried out at the IGISOL facility in Jyväskylä, Finland, where a 12.2 kHz radioactive beam of ^{12}B was implanted into a thin foil inside the detector chamber. Of these, approximately 4.2×10^5 triple-α coincidences were

measured in full kinematics, which is orders of magnitude more than the previous similar experiment [Dig+09].

The triple-α breakups were divided into two categories based on the invariant energy of the two lowest energy α-particles and analyzed both separately and in one combined analysis using R-matrix theory. Breakups through the excited state in ^{8}Be were analyzed by comparing the phase space distributions at different energies to theoretical distributions. The theoretical phase space distributions were combined with a custom Monte Carlo simulation tool based on Geant4, to take into account experimental effects, acceptance, and cuts made in the event reconstruction analysis. The primary constituent of the broad peak was found to be best described by 0^+ strength which decays with the emission of a $L = 0$ α-particle to the *ghost* of the ^{8}Be ground state. This observation is consistent with the interpretation that the Hoyle state *ghost* contributes significantly in this region. The remaining strength was found to be best described by 2^+ strength decaying to the ^{8}Be ground state *ghost* through the emission of a $L = 2$ α-particle. This is consistent with the findings from [Zim+13], who observed a 2^+ state at 10 MeV, which decays exclusively through the $(2, 2, 0)$ channel. Additionally, a similar study by [Ref16] found similar evidence but concludes that the phase space distribution of this channel is not easily distinguishable from 0^+ decays with $L = 0$. When gating on the 1^+ level at 12.7 MeV, the phase space distribution was best described purely by decays through the $(1, 2, 2)$ channel.

The excitation spectrum of breakups decaying through the ^{8}Be ground state peak was analyzed using the standard multi-channel multi-level R-matrix description provided in [Bar68; Bar69; Hyl10], and the spectrum was fitted using a range of different models. When fixing the Hoyle state parameters to literature values, the models showed sensitivity toward the spin of the states around 10 MeV. Most of the broad peak was best described by the Hoyle state *ghost* and a 0^+ state at roughly 11 MeV, and interference between the two is needed to reproduce the observed asymmetry in the peak. Another broad 0^+ component located at high energy is also needed to provide an acceptable fit. A similar broad resonance is seen in [Hyl+10] and is attributed to either the low energy tail of a higher-lying resonance or non-resonant direct decays. It was also found that including a 2^+ resonance results in a significant improvement in fit quality compared to yet another 0^+ resonance. The features of this 2^+ resonance was found to be model-dependent. The resonance energy varied from 11-11.5 MeV and the width

was found to be between 1.8-2.4 MeV. In [Hyl+10], a 2^+ resonance was observed at 11.2(3) MeV with $\Gamma = 1.4(4)$ MeV. Note that they observed a model-dependent variation by a factor of two on the resonance width and B(GT) values.

A novel combined analysis of the two abovementioned decay types was presented in section 9.5. This analysis is based on a recently developed, unpublished R-matrix model, which aims to give a full description of the β-delayed triple-α decay of ^{12}B and ^{12}N. This analysis did not result in any good fits based on the χ^2 value, however, it was included as a proof-of-concept. All tested models showed some evidence of a 0^+ resonance located at 11.1 MeV, decaying primarily by the emission of a $L = 0$ α-particle which is consistent with the findings from the phase space distribution analysis. The width of this state was found to be between 1.5-1.8 MeV which is consistent with the findings in section 9.4 and the resonance recommended by [Hyl+10]. The B(GT) value was a factor of two larger than what was found in [Hyl+10]. A significantly better fit was achieved when adding a third 0^+ level. The resonance energy of this level varied but was found in all cases to primarily decay through the $(0, 2, 2)$ channel. The fits also showed some evidence for a 2^+ level at 11.5-11.9 MeV with $\Gamma = 950$ keV and poorly determined B(GT) value. It was found to primarily decay via $L = 0$ α emission, again, consistent with the phase space distribution analysis.

A pattern is starting to emerge around the ^{8}Be(ex.) spectrum at roughly 11.5 MeV excitation energy. A comparison between the ^{8}Be(peak) and ^{8}Be(ex.) spectrum shows some resonance-like structure with a strong coupling to ^{8}Be(2^+) in this region. However, the fits in section 9.5 do not reproduce this, and a systematic error is seen at the same energy range in the E_{tot}-projection of the ^{8}Be(ex.) spectrum. The same region was found problematic in a separate study by [Ref16].

Lastly, the $\beta - \alpha$ angular correlation function was extracted and compared to simulations with an isotropic angular distribution. The correlation amplitude was extracted and the region between 9.5-11 MeV showed evidence for significant anisotropy while the remaining fits were also consistent with isotropy. The amplitude was compared to a similar measurement from [Gar17], and was found to be consistent.

The experiment presented in this work is the first time the region all the way up

to the 12.7 MeV level has been successfully measured through ^{12}B β decay, with full kinematic information. Combined with the ^{12}N measurement presented in [Ref16; Gar17] and the implantation experiments from [Hyl+09; Hyl+10], we have now investigated the entire region of ^{12}C populated by β decay. While one can always wish for more statistics, we are now, with this experiment, reaching a point of diminishing returns in that regard. As such, experiment I257 marks the end of a 20+ year-long experimental effort by our group to understand the ^{12}C continuum through β-delayed triple-α decay.

The results from the combined R-matrix analysis are still very premature. However, if it is even possible to describe the spectrum in terms of R-matrix theory and resonances, the tools needed to understand it should now be in place. An interesting next step could be to combine the present experimental data in a full fit to both the kinematics experiments and the implantation experiments, simultaneously to ^{12}N and ^{12}B data.

Appendix A

Illustrations of models 5, 6 and 7 from section 9.5 are shown in fig. 1, fig. 2 and fig. 3, respectively. The plot in the upper-right corner is the ^{8}Be(peak) spectrum along with the total fit. The colored lines correspond to the single-level approximations of all levels in the model. The E_{tot}-projection of the ^{8}Be(ex.) spectrum is plotted in the upper-left corner as the blue line, with the R-matrix expression plotted in red. For each bin in the E_{tot} plot, a Dalitz plot is generated and evaluated. However, the Dalitz plots in the lower two rows are binned in 1 MeV intervals. The middle row is data while the bottom row is the acceptance-corrected R-matrix generated Dalitz plots. The fit parameters are listed in table 9.5.

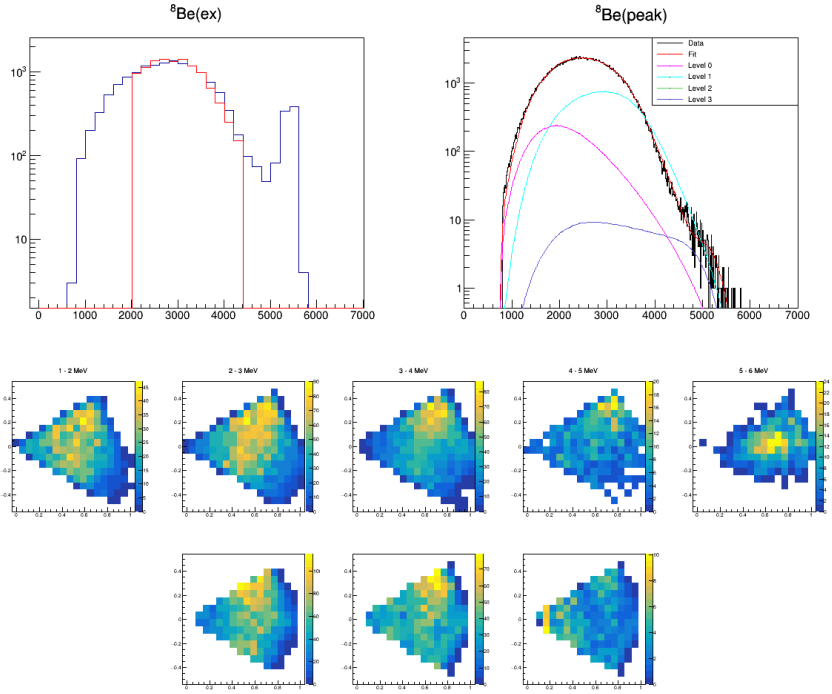

Figure 1: *Plot of combined fit to model 5. Upper right plot shows the ^{8}Be(peak) spectrum, upper left is the E_{tot}-projection of ^{8}Be(ex.) spectrum. Middle and bottom rows are measured and fitted Dalitz plots, respectively.*

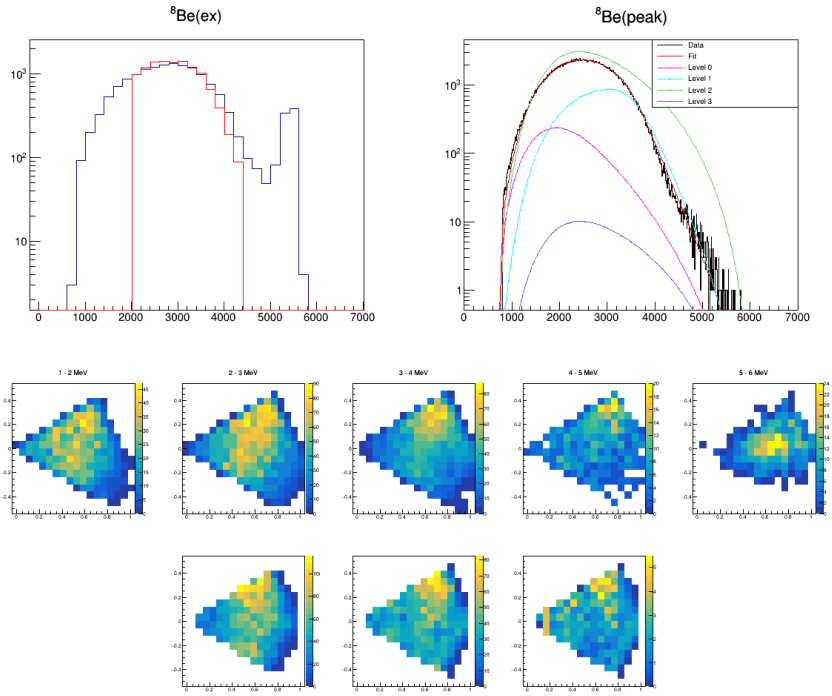

Figure 2: *Plot of combined fit to model 6. Upper right plot shows the ^{8}Be(peak) spectrum, upper left is the E_{tot}-projection of ^{8}Be(ex.) spectrum. Middle and bottom rows are measured and fitted Dalitz plots, respectively.*

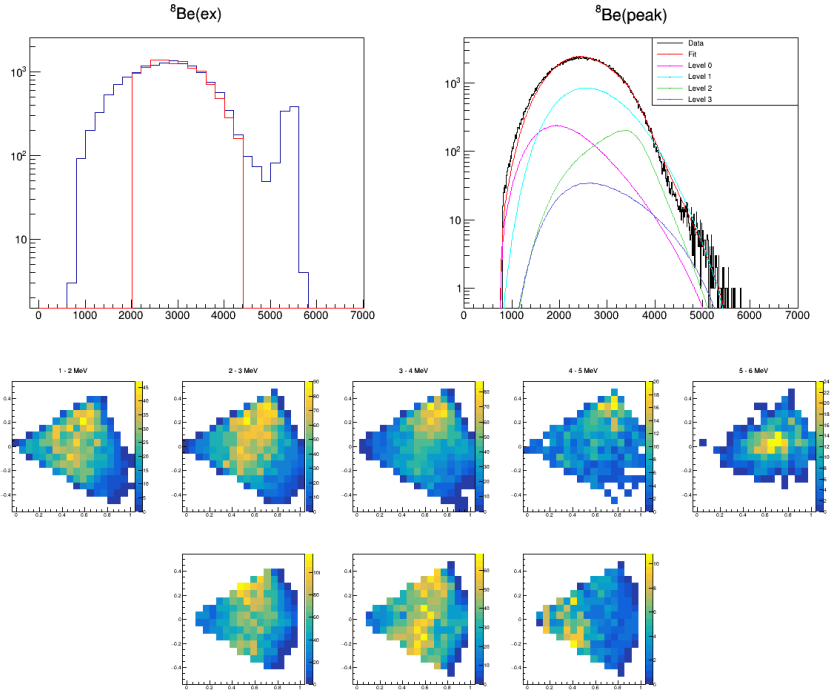

Figure 3: *Plot of combined fit to model 7. Upper right plot shows the ^{8}Be(peak) spectrum, upper left is the E_{tot}-projection of ^{8}Be(ex.) spectrum. Middle and bottom rows are measured and fitted Dalitz plots, respectively.*

Bibliography

[Ago+03] S. Agostinelli et al. "Geant4—a simulation toolkit". In: *Nuclear Instruments and Methods in Physics Research Section A: Accelerators, Spectrometers, Detectors and Associated Equipment* 506.3 (2003), pp. 250–303. ISSN: 0168-9002. DOI: https://doi.org/10.1016/S0168-9002(03)01368-8.

[Ajz90] F. Ajzenberg-Selove. "Energy levels of light nuclei A = 11-12". In: *Nuclear Physics A* 506.1 (1990), pp. 1–158. ISSN: 0375-9474. DOI: https://doi.org/10.1016/0375-9474(90)90271-M. URL: https://www.sciencedirect.com/science/article/pii/037594749090271M.

[ABG48] R. A. Alpher, H. Bethe, and G. Gamow. "The Origin of Chemical Elements". In: *Phys. Rev.* 73 (7 Apr. 1948), pp. 803–804. DOI: 10.1103/PhysRev.73.803. URL: https://link.aps.org/doi/10.1103/PhysRev.73.803.

[Äys+14] J. Äystö et al. *Three decades of research using IGISOL technique at the University of Jyväskylä*. Springer, Dordrecht, 2014. DOI: https://doi.org/10.1007/978-94-007-5555-0.

[BZT74] D. P. Balamuth, R. W. Zurmühle, and S. L. Tabor. "Isospin-forbidden alpha decay of the 15.11-MeV state in ^{12}C". In: *Phys. Rev. C* 10 (3 Sept. 1974), pp. 975–986. DOI: 10.1103/PhysRevC.10.975. URL: https://link.aps.org/doi/10.1103/PhysRevC.10.975.

[Bar68] F.C. Barker. "0^+ states of ^{8}Be". In: *Australian Journal of Physics* 21 (1968), p. 239.

[Bar69] F.C. Barker. "2^+ states of ^{8}Be". In: *Australian Journal of Physics* 22 (1969), pp. 293–316.

[BW88] F.C. Barker and E.K. Warburton. "The beta-decay of 8He". In: *Nuclear Physics A* 487.2 (1988), pp. 269–278. ISSN: 0375-9474. DOI: https://doi.org/10.1016/0375-9474(88)90613-6. URL: https://www.sciencedirect.com/science/article/pii/0375947488906136.

[BT62] F.C Barker and P.B Treacy. "Nuclear levels near thresholds". In: *Nuclear Physics* 38 (1962), pp. 33–49. ISSN: 0029-5582. DOI: https://doi.org/10.1016/0029-5582(62)91014-3. URL: https://www.sciencedirect.com/science/article/pii/0029558262910143.

[Ber+16] M. J. Berger et al. "Report 49". In: *Journal of the International Commission on Radiation Units and Measurements* os25.2 (Apr. 2016), NP–NP. ISSN: 1473-6691. DOI: 10.1093/jicru/os25.2.Report49. eprint: https://academic.oup.com/jicru/article-pdf/os25/2/NP/9587198/jicruos25-NP.pdf. URL: https://doi.org/10.1093/jicru/os25.2.Report49.

[BAS06] M. Bhattacharya, E. G. Adelberger, and H. E. Swanson. "Precise study of the final-state continua in ^{8}Li and ^{8}B decays". In: *Phys. Rev. C* 73 (5 May 2006), p. 055802.

[Bis+20] J. Bishop et al. "Beta-delayed charged-particle spectroscopy using TexAT". In: *Nuclear Instruments and Methods in Physics Research Section A: Accelerators, Spectrometers, Detectors and Associated Equipment* 964 (2020), p. 163773. ISSN: 0168-9002. DOI: https://doi.org/10.1016/j.nima.2020.163773. URL: https://www.sciencedirect.com/science/article/pii/S0168900220303089.

[BC87] G. Bortels and P. Collaers. "Analytical function for fitting peaks in alpha-particle spectra from Si detectors". In: *International Journal of Radiation Applications and Instrumentation. Part A. Applied Radiation and Isotopes* 38.10 (1987), pp. 831–837. ISSN: 0883-2889. DOI:

https://doi.org/10.1016/0883-2889(87)90180-8. URL: https://www.sciencedirect.com/science/article/pii/0883288987901808.

[Bur+57] E. Margaret Burbidge et al. "Synthesis of the Elements in Stars". In: *Rev. Mod. Phys.* 29 (4 Oct. 1957), pp. 547–650. DOI: 10.1103/RevModPhys.29.547. URL: https://link.aps.org/doi/10.1103/RevModPhys.29.547.

[CER21] CERN. *ROOT*. 2021. URL: https://root.cern.ch/.

[Che+07] M. Chernykh et al. "Structure of the Hoyle State in ^{12}C". In: *Phys. Rev. Lett.* 98 (3 Jan. 2007), p. 032501. DOI: 10.1103/PhysRevLett.98.032501. URL: https://link.aps.org/doi/10.1103/PhysRevLett.98.032501.

[CK65] S. Cohen and D. Kurath. "Effective interactions for the 1p shell". In: *Nuclear Physics* 73.1 (1965), pp. 1–24. ISSN: 0029-5582. DOI: https://doi.org/10.1016/0029-5582(65)90148-3. URL: https://www.sciencedirect.com/science/article/pii/0029558265901483.

[Coo+57] C. W. Cook et al. "B^{12}, C^{12}, and the Red Giants". In: *Phys. Rev.* 107 (2 July 1957), pp. 508–515. DOI: 10.1103/PhysRev.107.508. URL: https://link.aps.org/doi/10.1103/PhysRev.107.508.

[Coo+58] C. W. Cook et al. "High-Energy Alpha Particles from B^{12}". In: *Phys. Rev.* 111 (2 July 1958), pp. 567–571. DOI: 10.1103/PhysRev.111.567. URL: https://link.aps.org/doi/10.1103/PhysRev.111.567.

[DJ50] Goward F. D. and Wilkins J.J. In: *Proc. Phys. Soc. (London)* A(63) (1950), p. 1171.

[DI53] Jackson J. D. and Wanklyn D. I. In: *Phys. Rev.* 86 (1953), 381(A).

[DH 00] D.H. Wilkinson. "Limits to second-class nucleonic and mesonic currents". In: *Eur. Phys. J. A* 7.3 (2000), pp. 307–315. DOI: 10.1007/s100500050397. URL: https://doi.org/10.1007/s100500050397.

[Dal53] R.H. Dalitz. "CXII. On the analysis of τ-meson data and the nature of the τ-meson". In: *The London, Edinburgh, and Dublin Philosophical Magazine and Journal of Science* 44.357 (1953), pp. 1068–1080. DOI: 10.1080/14786441008520365. URL: https://doi.org/10.1080/14786441008520365.

[Den97] Peter Dendooven. "The development and status of the IGISOL technique". In: *Nuclear Instruments and Methods in Physics Research Section B: Beam Interactions with Materials and Atoms* 126.1 (1997). International Conference on Electromagnetic Isotope Separators and Techniques Related to Their Applications, pp. 182–189. ISSN: 0168-583X. DOI: https://doi.org/10.1016/S0168-583X(96)01010-5. URL: https://www.sciencedirect.com/science/article/pii/S0168583X96010105.

[Dig06] C. Aa. Diget. "Beta delayed particle emission". PhD thesis. Aarhus University, Department of Physics and Astronomy, Sept. 2006.

[Dig+09] C. Aa. Diget et al. "Breakup channels for ^{12}C triple-α continuum states". In: *Phys. Rev. C* 80 (3 Sept. 2009), p. 034316. DOI: 10.1103/PhysRevC.80.034316. URL: https://link.aps.org/doi/10.1103/PhysRevC.80.034316.

[Dun+53] D. N. F. Dunbar et al. "The 7.68-Mev State in C^{12}". In: *Phys. Rev.* 92 (3 Nov. 1953), pp. 649–650. DOI: 10.1103/PhysRev.92.649. URL: https://link.aps.org/doi/10.1103/PhysRev.92.649.

[Eic+66] H. Eichner et al. "$\beta\gamma$- und $\beta\alpha$-Winkelkorrelationen beim Zerfall von ^{8}Li und ^{8}B". In: *Z.Naturforsch.* 21a (1966), p. 908.

[ENS] ENSDF. *From ENSDF database as of August 9th, 2021. Version available at http://www.nndc.bnl.gov/ensarchivals/.*

[Epe+12] Evgeny Epelbaum et al. "Structure and Rotations of the Hoyle State". In: *Phys. Rev. Lett.* 109 (25 Dec. 2012), p. 252501. DOI: 10.1103/PhysRevLett.109.252501. URL: https://link.aps.org/doi/10.1103/PhysRevLett.109.252501.

[Fre+09] M. Freer et al. "2^+ excitation of the ^{12}C Hoyle state". In: *Phys. Rev. C* 80 (4 Oct. 2009), p. 041303. DOI: 10.1103/PhysRevC.80.041303. URL: https://link.aps.org/doi/10.1103/PhysRevC.80.041303.

[Fre+12] M. Freer et al. "Consistent analysis of the 2^+ excitation of the ^{12}C Hoyle state populated in proton and α-particle inelastic scattering". In: *Phys. Rev. C* 86 (3 Sept. 2012), p. 034320. DOI: 10.1103/PhysRevC.86.034320. URL: https://link.aps.org/doi/10.1103/PhysRevC.86.034320.

[Fre+18] Martin Freer et al. "Microscopic clustering in light nuclei". In: *Rev. Mod. Phys.* 90 (3 Aug. 2018), p. 035004. DOI: 10.1103/RevModPhys.90.035004. URL: https://link.aps.org/doi/10.1103/RevModPhys.90.035004.

[Fun+05] Funaki, Y. et al. "Resonance states in 12C and ticle condensation". In: *Eur. Phys. J. A* 24.3 (2005), pp. 321–342. DOI: 10.1140/epja/i2004-10238-x. URL: https://doi.org/10.1140/epja/i2004-10238-x.

[Fyn+03] H. O. U. Fynbo et al. "Clarification of the Three-Body Decay of ^{12}C (12.71 MeV)". In: *Phys. Rev. Lett.* 91 (8 Aug. 2003), p. 082502. DOI: 10.1103/PhysRevLett.91.082502. URL: https://link.aps.org/doi/10.1103/PhysRevLett.91.082502.

[Fyn+05] H. O. U. Fynbo et al. "Revised rates for the stellar triple-α process from measurement of ^{12}C nuclear resonances". In: *Nature* 433.7022 (Jan. 2005), pp. 136–139. URL: http://dx.doi.org/10.1038/nature03219.

[Gad21] A Gad. *G4Sim*. 2021. URL: https://gitlab.au.dk/au479664/G4Sim.

[Gar17] R. Garg. "Hoyle state rotational excitation studied via β-triple-α angular correlations". PhD thesis. University of York, Oct. 2017.

[21a] *Geant4 GPS*. 2021. URL: https://geant4-userdoc.web.cern.ch/UsersGuides/ForApplicationDeveloper/html/GettingStarted/generalParticleSource.html.

[GP63] Neel W. Glass and Robert W. Peterson. "Direct Comparison of the B^{12} and N^{12} Beta Spectra". In: *Phys. Rev.* 130 (1 Apr. 1963), pp. 299–305. DOI: 10.1103/PhysRev.130.299. URL: https://link.aps.org/doi/10.1103/PhysRev.130.299.

[Ham47] Donald R. Hamilton. "Electron-Neutrino Angular Correlation in Beta-Decay". In: *Phys. Rev.* 71 (7 Apr. 1947), pp. 456–457. DOI: 10.1103/PhysRev.71.456. URL: https://link.aps.org/doi/10.1103/PhysRev.71.456.

[Hol74] Barry R. Holstein. "Recoil effects in allowed beta decay: The elementary particle approach". In: *Rev. Mod. Phys.* 46 (4 Oct. 1974), pp. 789–814. DOI: 10.1103/RevModPhys.46.789. URL: https://link.aps.org/doi/10.1103/RevModPhys.46.789.

[HDa53] F. Hoyle, D. Dunbar, and et al. "A State in C^{12} Predicted from Astrophysical Evidence." In: *Physical Review* (1953).

[Hyl10] S. Hyldegaard. "Beta-decay studies of ^{8}B and ^{12}C". PhD thesis. Aarhus University, Department of Physics and Astronomy, Aug. 2010.

[Hyl+09] S. Hyldegaard et al. "Precise branching ratios to unbound ^{12}C states from ^{12}N and 12B β-decays". In: *Physics Letters B* 678.5 (2009), pp. 459–464. ISSN: 0370-2693. DOI: https://doi.org/10.1016/j.physletb.2009.06.064. URL: https://www.sciencedirect.com/science/article/pii/S0370269309007771.

[Hyl+10] S. Hyldegaard et al. "R-matrix analysis of the β decays of ^{12}N and ^{12}B". In: *Phys. Rev. C* 81 (2 Feb. 2010), p. 024303. DOI: 10.1103/PhysRevC.81.024303. URL: https://link.aps.org/doi/10.1103/PhysRevC.81.024303.

[IGI] IGISOL. *Ion Guide Isotope Separator On-Line (IGISOL)*. URL: https://www.jyu.fi/science/en/physics/research/infrastructures/accelerator-laboratory/nuclear-physics-facilities/the-exotic-nuclei-and-beams/ion-guide-isotope-separator-on-line-igisol. (accessed: 26.07.2021).

[ITH68] Kiyomi Ikeda, Noboru Takigawa, and Hisashi Horiuchi. "The Systematic Structure-Change into the Molecule-like Structures in the Self-Conjugate 4n Nuclei". In: *Progress of Theoretical Physics Supplement* E68 (July 1968), pp. 464–475. ISSN: 0375-9687. DOI: 10.1143/PTPS.E68.464. URL: https://doi.org/10.1143/PTPS.E68.464.

[ITK19] R. Imai, T. Tada, and M. Kimura. "Real-time evolution method and its application to the 3α cluster system". In: *Phys. Rev. C* 99 (6 June 2019), p. 064327. DOI: 10.1103/PhysRevC.99.064327. URL: https://link.aps.org/doi/10.1103/PhysRevC.99.064327.

[Ito+11] M. Itoh et al. "Candidate for the 2^+ excited Hoyle state at $E_x \sim 10$ MeV in ^{12}C". In: *Phys. Rev. C* 84 (5 Nov. 2011), p. 054308. DOI: 10.1103/PhysRevC.84.054308. URL: https://link.aps.org/doi/10.1103/PhysRevC.84.054308.

[Jen21] E.A.M. Jensen. *DecSD*. 2021. URL: https://gitlab.au.dk/ausa/erik/decsd.

[Kan07] Yoshiko Kanada-En'yo. "The Structure of Ground and Excited States of 12C". In: *Progress of Theoretical Physics* 117.4 (Apr. 2007), pp. 655–680. ISSN: 0033-068X. DOI: 10.1143/PTP.117.655. URL: https://doi.org/10.1143/PTP.117.655.

[Kar+95] S. Karataglidis et al. "Fully microscopic model of 200 MeV proton−^{12}C elastic and inelastic scattering". In: *Phys. Rev. C* 52 (2 Aug. 1995), pp. 861–877. DOI: 10.1103/PhysRevC.52.861. URL: https://link.aps.org/doi/10.1103/PhysRevC.52.861.

[KPS17] J.H. Kelley, J.E. Purcell, and C.G. Sheu. "Energy levels of light nuclei A=12". In: *Nuclear Physics A* 968 (2017), pp. 71–253. ISSN: 0375-9474. DOI: https://doi.org/10.1016/j.nuclphysa.2017.07.015. URL: https://www.sciencedirect.com/science/article/pii/S0375947417303330.

[Kir+11] O. S. Kirsebom et al. "Precise and accurate determination of the ^{8}B decay spectrum". In: *Phys. Rev. C* 83 (6 June 2011), p. 065802.

[Kir+19] O. S. Kirsebom et al. "Discovery of an Exceptionally Strong β-Decay Transition of ^{20}F and Implications for the Fate of Intermediate-Mass Stars". In: *Phys. Rev. Lett.* 123 (26 Dec. 2019), p. 262701. DOI: 10.1103/PhysRevLett.123.262701. URL: https://link.aps.org/doi/10.1103/PhysRevLett.123.262701.

[Kir10] O.S. Kirsebom. "^{8}B Neutrinos and ^{12}C Resonances". PhD thesis. Aarhus University, Department of Physics and Astronomy, Aug. 2010.

[LT58] A. M. Lane and R. G. Thomas. "R-Matrix Theory of Nuclear Reactions". In: *Rev. Mod. Phys.* 30 (2 Apr. 1958), pp. 257–353.

[Lau+13] Laursen, K. L. et al. "High-statistics measurement of the β-delayed α spectrum of 20Na". In: *Eur. Phys. J. A* 49.6 (2013), p. 79. DOI: 10.1140/epja/i2013-13079-6. URL: https://doi.org/10.1140/epja/i2013-13079-6.

[Lau14] K. L. Laursen. "Broad resonances in ^{12}C and ^{20}Ne". PhD thesis. Aarhus University, Department of Physics and Astronomy, Dec. 2014.

[Li+20] K. C. W. Li et al. *Multi-probe study of excited states in ^{12}C: disentangling the sources of monopole strength between the Hoyle state and $E_x = 13$ MeV*. 2020. arXiv: 2011.10112 [nucl-ex].

[MM62] T. Mayer-Kuckuk and F. C. Michel. "Comparison of the Beta Spectra of B^{12} and N^{12}". In: *Phys. Rev.* 127 (2 July 1962), pp. 545–554. DOI: 10.1103/PhysRev.127.545. URL: https://link.aps.org/doi/10.1103/PhysRev.127.545.

[MGG80] R. D. McKeown, G. T. Garvey, and C. A. Gagliardi. "Beta-alpha angular correlations in mass 8". In: *Phys. Rev. C* 22 (2 Aug. 1980), pp. 738–749. DOI: 10.1103/PhysRevC.22.738. URL: https://link.aps.org/doi/10.1103/PhysRevC.22.738.

[Mic07] N. Michel. "Precise Coulomb wave functions for a wide range of complex ℓ, η and z". In: *Computer Physics Communications* 176.3 (Feb. 2007), pp. 232–249. DOI: 10.1016/j.cpc.2006.10.004. arXiv: physics/0702051 [physics.comp-ph].

[Moo+13] I.D. Moore et al. "Towards commissioning the new IGISOL-4 facility". In: *Nuclear Instruments and Methods in Physics Research Section B: Beam Interactions with Materials and Atoms* 317 (2013). XVIth International Conference on ElectroMagnetic Isotope Separators and Techniques Related to their Applications, December 2–7, 2012 at Matsue, Japan, pp. 208–213. ISSN: 0168-583X. DOI: https://doi.org/10.1016/j.nimb.2013.06.036. URL: https://www.sciencedirect.com/science/article/pii/S0168583X13007143.

[Mor56] H. Morinaga. "Interpretation of Some of the Excited States of $4n$ Self-Conjugate Nuclei". In: *Phys. Rev.* 101 (1 Jan. 1956), pp. 254–258. DOI: 10.1103/PhysRev.101.254. URL: https://link.aps.org/doi/10.1103/PhysRev.101.254.

[Mor66] H. Morinaga. "On the spin of a broad state around 10 MeV in 12C". In: *Physics Letters* 21.1 (1966), pp. 78–79. ISSN: 0031-9163. DOI: https://doi.org/10.1016/0031-9163(66)91349-7. URL: https://www.sciencedirect.com/science/article/pii/0031916366913497.

[Mor59] Masato Morita. "Higher Order Corrections to the Allowed Beta Decay". In: *Phys. Rev.* 113 (6 Mar. 1959), pp. 1584–1589. DOI: 10.1103/PhysRev.113.1584. URL: https://link.aps.org/doi/10.1103/PhysRev.113.1584.

[MM66] Masato Morita and Reiko Morita. "Beta-Gamma Angular Correlations and Beta-Ray Angular Distributions". In: *Progress of Theoretical Physics Supplement* 37-38 (Mar. 1966), pp. 458–472. ISSN: 0375-9687. DOI: 10.1143/PTPS.37.458. URL: https://doi.org/10.1143/PTPS.37.458.

[MHK17] M. Munch, J. Halkjær, and O.S. Kirsebom. *AUSALIB - Aarhus Subatomic Library*. 2017. URL: https://gitlab.au.dk/ausa/ausalib/wikis/home.

[Mun+16] M. Munch et al. "Independent measurement of the Hoyle state β feeding from ^{12}B using Gammasphere". In: *Phys. Rev. C* 93 (6 June 2016), p. 065803. DOI: 10.1103/PhysRevC.93.065803. URL: https://link.aps.org/doi/10.1103/PhysRevC.93.065803.

[Mun+19] M. Munch et al. "VME Readout at and Below the Conversion Time Limit". In: *IEEE Transactions on Nuclear Science* 66.2 (Feb. 2019), pp. 575–584. ISSN: 1558-1578. DOI: 10.1109/tns.2018.2884979. URL: http://dx.doi.org/10.1109/TNS.2018.2884979.

[NVB00a] P. Navrátil, J. P. Vary, and B. R. Barrett. "Large-basis ab initio no-core shell model and its application to ^{12}**C**". In: *Phys. Rev. C* 62 (5 Oct. 2000), p. 054311. DOI: 10.1103/PhysRevC.62.054311. URL: https://link.aps.org/doi/10.1103/PhysRevC.62.054311.

[NVB00b] P. Navrátil, J. P. Vary, and B. R. Barrett. "Properties of ^{12}C in the Ab Initio Nuclear Shell Model". In: *Phys. Rev. Lett.* 84 (25 June 2000), pp. 5728–5731. DOI: 10.1103/PhysRevLett.84.5728. URL: https://link.aps.org/doi/10.1103/PhysRevLett.84.5728.

[Neu51] John von Neumann. "Various Techniques Used in Connection with Random Digits". In: *Monte Carlo Method*. Ed. by A. S. Householder, G. E. Forsythe, and H. H. Germond. Vol. 12. National Bureau of Standards Applied Mathematics Series. Washington, DC: US Government Printing Office, 1951. Chap. 13, pp. 36–38.

[NND] NNDC. *From NNDC database as of October 7th, 2021. Version available at https://www.nndc.bnl.gov/nudat2/.*

[Öpi51] E. J. Öpik. "Stellar Models with Variable Composition. II. Sequences of Models with Energy Generation Proportional to the Fifteenth Power of Temperature". In: *Proceedings of the*

Royal Irish Academy. Section A: Mathematical and Physical Sciences 54 (1951), pp. 49–77. ISSN: 00358975. URL: http://www.jstor.org/stable/20488524.

[RGS65] R. S. Raghavan, Z. W. Grabowski, and R. M. Steffen. "Study of Second Excited 2^+ States of Some Even-Even Nuclei by Beta-Gamma Angular Correlations". In: *Phys. Rev.* 139 (1B July 1965), B1–B8. DOI: 10.1103/PhysRev.139.B1. URL: https://link.aps.org/doi/10.1103/PhysRev.139.B1.

[Ref16] J. Refsgaard. "Resonances, R-Matrix - Rotations in ^{12}C". PhD thesis. Aarhus University, Department of Physics and Astronomy, Sept. 2016.

[Rii+15] K. Riisager et al. "Broad resonances and beta-decay". In: *Nuclear Physics A* 940 (Apr. 2015).

[RR88] C. E. Rolfs and W. S. Rodney. *Cauldrons in the cosmos: Nuclear astrophysics.* Chicago: University of Chicago Press., 1988.

[Rot+04] R. Roth et al. "Nuclear structure based on correlated realistic nucleon–nucleon potentials". In: *Nuclear Physics A* 745.1 (2004), pp. 3–33. ISSN: 0375-9474. DOI: https://doi.org/10.1016/j.nuclphysa.2004.08.024. URL: https://www.sciencedirect.com/science/article/pii/S0375947404008917.

[Rot+11] Robert Roth et al. "Similarity-Transformed Chiral $NN + 3N$ Interactions for the Ab Initio Description of ^{12}**C** and ^{16}**O**". In: *Phys. Rev. Lett.* 107 (7 Aug. 2011), p. 072501. DOI: 10.1103/PhysRevLett.107.072501. URL: https://link.aps.org/doi/10.1103/PhysRevLett.107.072501.

[Sal52] E.E. Salpeter. "Nuclear Reactions in Stars Without Hydrogen." In: *apj* 115 (Mar. 1952), pp. 326–328. DOI: 10.1086/145546.

[21b] *Sim3a*. 2021. URL: https://gitlab.au.dk/ausa/sim3a.

[Sin+98] B. Singh et al. "Review Of LogftValues In β Decay". In: *Nuclear Data Sheets* 84.3 (1998), pp. 487–563. ISSN: 0090-3752. DOI: https://doi.org/10.1006/ndsh.1998.0015. URL: https://www.sciencedirect.com/science/article/pii/S0090375298900151.

[05] "Stopping of Ions Heavier than Helium". In: *Journal of the ICRU* 5.1 (2005), pp. 1–1. DOI: 10.1093/jicru_ndi001. eprint: https://doi.org/10.1093/jicru_ndi001. URL: https://doi.org/10.1093/jicru_ndi001.

[Ten+04] O. Tengblad et al. "Novel thin window design for a large-area silicon strip detector". In: *Nuclear Instruments and Methods in Physics Research Section A: Accelerators, Spectrometers, Detectors and Associated Equipment* 525.3 (2004), pp. 458–464. ISSN: 0168-9002. DOI: https://doi.org/10.1016/j.nima.2004.01.082. URL: https://www.sciencedirect.com/science/article/pii/S0168900204002414.

[Til+04] D.R. Tilley et al. "Energy levels of light nuclei A=8,9,10". In: *Nuclear Physics A* 745.3 (2004), pp. 155–362. ISSN: 0375-9474.

[Toh+01] A. Tohsaki et al. "Alpha Cluster Condensation in ^{12}C and ^{16}O". In: *Phys. Rev. Lett.* 87 (19 Oct. 2001), p. 192501. DOI: 10.1103/PhysRevLett.87.192501. URL: https://link.aps.org/doi/10.1103/PhysRevLett.87.192501.

[TG75] R. E. Tribble and G. T. Garvey. "Induced weak currents and $\beta^{\pm} - \alpha$ angular correlations in $A = 8$". In: *Phys. Rev. C* 12 (3 Sept. 1975), pp. 967–983. DOI: 10.1103/PhysRevC.12.967. URL: https://link.aps.org/doi/10.1103/PhysRevC.12.967.

[Viñ+21] S. Viñals et al. "Calibration and response function of a compact silicon-detector set-up for charged-particle spectroscopy using GEANT4". In: *The European Physical Journal A* 57.2 (Feb. 2021), p. 49. ISSN: 1434-601X. DOI: 10.1140/epja/s10050-021-00371-5. URL: https://doi.org/10.1140/epja/s10050-021-00371-5.

[Vog62] Erich Vogt. "Theory of Low Energy Nuclear Reactions". In: *Rev. Mod. Phys.* 34 (4 Oct. 1962), pp. 723–747.

[Vog04] Erich Vogt. "R-Matrix Theory". In: *Lecture notes for the R-Matrix School of the Joint Institute for Nuclear Astrophysics at Notre Dame University.* South Bend Indiana, Oct. 2004.

[WA71] D. H. Wilkinson and D. E. Alburger. "β Decay of ^{8}Li and ^{8}B: The Second-Class Current Problem". In: *Phys. Rev. Lett.* 26 (18 May 1971), pp. 1127–1130. DOI: 10.1103/PhysRevLett.26.1127. URL: https://link.aps.org/doi/10.1103/PhysRevLett.26.1127.

[Wil+63] D. H. Wilkinson et al. "Alpha-Particle Emission in the Decays of B^{12} and N^{12}". In: *Phys. Rev.* 130 (5 June 1963), pp. 1953–1960. DOI: 10.1103/PhysRev.130.1953. URL: https://link.aps.org/doi/10.1103/PhysRev.130.1953.

[YS05] Yamada, T. and Schuck, P. "Single ticle orbits and Bose-Einstein condensation in 12C". In: *Eur. Phys. J. A* 26.2 (2005), pp. 185–199. DOI: 10.1140/epja/i2005-10168-1. URL: https://doi.org/10.1140/epja/i2005-10168-1.

[YS04] Taiichi Yamada and Peter Schuck. "Dilute multi-α cluster states in nuclei". In: *Phys. Rev. C* 69 (2 Feb. 2004), p. 024309. DOI: 10.1103/PhysRevC.69.024309. URL: https://link.aps.org/doi/10.1103/PhysRevC.69.024309.

[ZZB10] J.F. Ziegler, M.D. Ziegler, and J.P. Biersack. "SRIM – The stopping and range of ions in matter (2010)". In: *Nuclear Instruments and Methods in Physics Research Section B: Beam Interactions with Materials and Atoms* 268.11 (2010). 19th International Conference on Ion Beam Analysis, pp. 1818–1823. ISSN: 0168-583X.

[Zim+13] W. R. Zimmerman et al. "Unambiguous Identification of the Second 2^{+} State in $^{12}\mathbf{C}$ and the Structure of the Hoyle State". In: *Phys. Rev. Lett.* 110 (15 Apr. 2013), p. 152502. DOI: 10.1103/PhysRevLett.110.152502. URL: https://link.aps.org/doi/10.1103/PhysRevLett.110.152502.